Thin-Film Microelectrode Arrays: Materials & Designs

A dissertation
submitted to the Faculty of Sciences of the University of Neuchâtel,
in fulfilment of the requirements for the degree of "Docteur ès Sciences"

by

Fiaccabrino Giovanni Carlo
Dipl. Microtech. Ing. EPFL

Institute of Microtechnology
University of Neuchâtel
Rue Jaquet-Droz 1, CH-2000 Neuchâtel
Switzerland

1996

IMPRIMATUR POUR LA THÈSE

Thin-Film Microelectrode Arrays : Materials and Designs

de M. Giovanni Carlo Fiaccabrino

UNIVERSITÉ DE NEUCHÂTEL

FACULTÉ DES SCIENCES

La Faculté des sciences de l'Université de Neuchâtel sur le rapport des membres du jury,

Madame M. Koudelka-Hep, Messieurs N. F. de Rooij, H. Girault (EPFL) et H. Schäfer (Herisau)

autorise l'impression de la présente thèse.

Neuchâtel, le 9 octobre 1996

Le doyen:

R. Dändliker

R. Dändliker

Abstract

The recourse to the thin-film technology is an attractive alternative for the fabrication of regular microelectrode arrays as it likely offers i) a control of the geometric parameters of the array (microelectrode dimensions and interelectrode spacing), ii) a simple and reliable fabrication procedure, and iii) a large throughput of devices showing reproducible electrochemical characteristics. This technological choice is embodied in the present work by three original thin-film microelectrode arrays, that is, ensembles of iridium microdisks, interdigitated arrays of carbon microbands and arrays of individually addressable platinum microelectrodes.

The first research subject has been initiated by the group of Prof. J. Buffle, "Departement de Chimie Minérale, Analytique et Appliquée" of the University of Geneva, as a logical extension of their work carried out on iridium microwires sealed in glass capillaries. The advantage resulting of the assembly of microdisks in arrays, as compared to a single microdisk, is a corresponding increase of the signal intensity and signal to noise ratio. Ensembles of 100 iridium microdisks featuring 2.5 μm radius and 150 μm interelectrode spacing are realized. The reliability of the fabrication process and the reproducibility of the devices electrochemical characteristics are assessed by running systematic voltammetric experiments. For the analysis of trace metals, mercury films are formed by electrodeposition on top of the microdisks surface. Successive depositions and dissolutions of the mercury films are performed on a panel of arrays to evaluate their life time. The reliability of the mercury-plated arrays is investigated through replicate measurements of lead and cadmium ions in the nanomolar concentration range. A detection limit of 50 pM for these metals is determined. Repeated measurements over a period of 5 hours are performed to determine the stability of the devices. The interest in mercury-plated microelectrode arrays for environmental applications is demonstrated by the direct measure of trace amounts of lead and cadmium in river water.

In collaboration with the "Centre Suisse d'Electronique et de Microtechnique" (CSEM), the development and optimization of a low temperature sputter deposition process (<120 °C) for the fabrication of carbon electrodes has been pursued. Through a systematic approach, the deposition parameters have been adjusted to yield conductive glassy carbon thin-films, firmly adhering to passivated silicon substrates and showing valuable electrochemical properties. The result of this investigation effort can be exploited to produce microelectrodes either on substrates including integrated electronics or on selected plastics. In the present work, the sequence of the technological steps is established to realize electrodes of various sizes and geometries on silicon wafer. The electrochemical properties are assessed with and without activating the electrode surface, and compared to commercially available glassy carbon electrodes. Stability of the activated electrodes is evaluated over a period of 6 months. Patterning of the sputtered carbon layers is illustrated by the fabrication of interdigitated microelectrode arrays featuring 2 μm resolution. The application of these devices in analytical measurements is emphasized by two sets of experiments involving dopamine as biologically important molecule, and acetaminophen as major pharmaceutical compound. Enhancement of the detection limit is achieved for both compounds by the redox cycling effect observed in generation-collection experiments.

In the last research subject, the electronic properties of silicon are exploited to integrate an "on chip" multiplexing unit, allowing the individual addressing of a large number of microelectrodes dedicated to electrochemical mapping purposes. An original and simple addressing principle based on nMOS analog switches is proposed. The device consists of an array of 100 platinum microsquares (25 μm side), arranged in a matrix of size 10 x 10. Each element of the array can thus be indexed by the row and column corresponding to its position in the matrix. The multiplexing function is realized by assigning two nMOS switches connected in series per electrode, and by operating them with the row and the column line corresponding to the address of the electrode. The electrical characteristics of the nMOS switches are assessed. Preliminary electrochemical images illustrate the mapping properties of the device.

Table of Contents

Introduction 

The most attractive aspect of miniaturization stems from the fact that minute size objects may exhibit unusual properties. This statement is embodied by various examples for which miniaturization has improved the characteristics of an object, increased the performances of a system or widened the extent of an application. In particular, significant advances have been accomplished in the field of electroanalytical chemistry by reducing the size of electrodes to and below the micrometer scale. The unique properties of microelectrodes, e.g. enhanced mass transport per unit area, increased temporal and spatial resolution, and large immunity to ohmic distortions have been adequately covered by the relevant research literature [1-10]. A qualitative overview of these properties is summarized hereafter, as they largely determine the characteristic behavior of microelectrode arrays. Aspects more specific to regular arrays are discussed. The objectives and the structure of this work are finally outlined.

1.1 Microelectrodes Properties

The unique properties of microelectrodes, such as the increase of the Faraday current density or the onset of steady or quasi steady-state diffusion regime, result from an enhanced mass transport process. Based on this particular feature rather then on geometric aspects, the following definition of a microelectrode is proposed [11]:

an electrode with at least one dimension small enough that its properties, e.g. mass transport regimes, are a function of size.

1.1.1 Enhanced mass transport

The situation of a molecule diffusing towards a normal-sized electrode (macroelectrode) is depicted in figure 1.1a. The electrode dimensions appear sufficiently large, when compared to the molecule average diffusion length, to consider the diffusion path as perpendicular to the electrode surface. The diffusion is known as planar. The discontinuity at the edges of the electrode only brings a small contribution to the total number of incident molecules. Reducing the dimensions of the same electrode significantly increases the relative ratio of molecules coming from the edges (fig. 1.1b). As a consequence, more electroactive species per unit time and area can now reach the electrode surface. A convergent flux governed by the geometry of the microelectrode surface gives rise to a non-planar diffusion. Frequently-used microelectrode geometries and associated diffusion layers are reported in table 1.1.

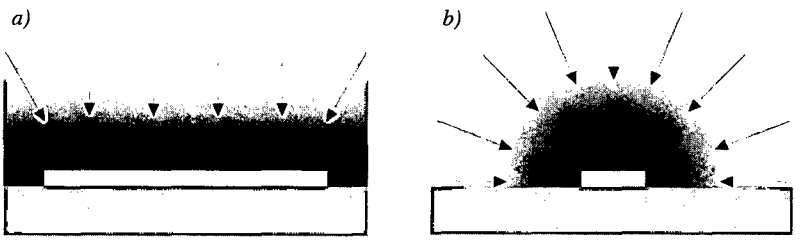

Figure 1.1: a) Planar diffusion, flux lines are mostly perpendicular to the electrode surface. b) Non-planar diffusion, edge effect modifies the geometry of the diffusion layer.

Since diffusion is a time-dependent process, different mass transport regimes are to be expected in the interval of the experiment. Upon initiating the charge transfer reaction, the thickness of the diffusion layer is smaller than the electrode dimensions. The species in the close vicinity of the electrode reach the electrode surface under planar diffusion. The microelectrode behavior first resembles to that of a macroelectrode. As the reaction proceeds, the species are transported across a time-growing diffusion layer. Transition to non-planar diffusion takes place as soon as the thickness of the diffusion layer is larger than at least one of the microelectrode dimensions.

By extension, it could be envisaged that the diffusion layer evolving at a macroelectrode in a quiescent solution would finally extend past the electrode dimensions, so that edge effect would also become noticeable. Yet, the extension of the diffusion layer over such distance does not occur due to natural convection effects. This situation sets an upper limit for the critical dimension of a microelectrode, beyond which the electrode behaves as a macroelectrode. On the other hand, the lower limit is not strictly determined by the limitations of the fabrication technique, but is theoretically given by the double layer thickness and/or the molecular dimension of the redox species. Below this limit, classical electrochemical expressions must be modified [12,13]. Depending on the experimental conditions, the critical dimension of a microelectrode for classic electrochemistry spans over a range of a few tens down to a fraction of a micrometer.

It is worth noting that closely spaced microelectrodes working in parallel, such as arrays of microdisks, will eventually undergo an additional transition to planar diffusion if the individual non-planar diffusion layers developing at each microelectrodes merge together. The overlap of the diffusion layers results in the creation of an apparent planar diffusion layer (fig.1.2a). This effect, known as shielding [14], is discussed in more details in section 1.2.1 and in chapter 3. The time scale of the experiment is usually chosen in order to avoid intermediate situations, where a mixed diffusion regime (planar and non-planar) complicates the analysis of the experimental results.

1.1.2 Steady-state response and high current density

The Faraday current density arising from a diffusion-controlled reaction is proportional to the mass transport rate, i.e. the concentration gradient of the electroactive species at the electrode surface. A close look at table 1.1 reveals that the current density for a plane and a line electrode geometry, respectively, shows a square root and a logarithmic dependence, whereas a time-independent expression is seen for a point geometry. In the absence of forced or natural convection, planar diffusion does not yield a steady-state response. As the reaction proceeds, species diffuse from further and further

portions of the bulk solution to bring new material to the electrode surface. The concentration gradient at the electrode surface relaxes and the diffusion rate decays. The Faraday current shows a time-dependence and is governed by the Cottrell equation [15]. Yet, the existence of natural convection prevents the indefinite growth of the diffusion layer. A steady-state concentration varying linearly is established across the Nernstian diffusion layer, that is, between the bulk of solution and the electrode surface. A limiting amperometric response, most likely suffering from interferences caused by convection effects, is generally observed at long experimental times.

In contrast, for a point electrode, the main concentration drop arises at the close vicinity of the electrode surface, within a distance comparable to the electrode radius. The resulting steep concentration gradient at the electrode surface leads to a high current density remaining virtually constant. The Faraday current tends asymptotically to a limiting value, that is independent of the diffusion layer and relatively insensitive to convection interferences. When the radius of the microelectrode is made sufficiently small, extremely high values of current density are achieved. These values correspond to those obtained at very short time scale experiments with conventionally-sized electrodes.

Hemicylindrical diffusion presents an intermediate situation for which a quasi steady-state diffusion regime is observed. The amperometric response

electrode	*diffusion*	*example*	*current density*	*ohmic drop*
plane	*planar*	*macroelectrode*	$\propto \frac{1}{\sqrt{Dt}}$	$\propto \frac{l}{\kappa\sqrt{Dt}}$
line	*cylindrical, hemicylindrical*	*microwire, microband*	$\propto \frac{1}{W\,ln\left(\sqrt{Dt}/W\right)}$	$\propto \frac{ln(d/W)}{\kappa\,ln\left(\sqrt{Dt}/W\right)}$
point	*spherical, hemispherical*	*microsphere, microdisk*	$\propto \frac{1}{r}$	$\propto \frac{1}{\kappa}$

Table 1.1: Microelectrode geometry and associated diffusion layer; approximations of the diffusion limited-current density following a potential step and of the ohmic drop [16]; D: diffusion coefficient, t: duration of the potential step, W: characteristic dimension of the line geometry (radius or width), r: characteristic dimension of the point geometry (radius), κ: conductivity of the solution, l: distance separating the reference from the working electrode.

exhibits a reduced time dependence. The current density remains higher than that of a planar electrode.
A quasi steady-state situation can also be reached when closely-spaced anode and cathode are within a common diffusion layer. For a reversible or a quasi-reversible reaction, the proximity of the electrodes causes reactants to be generated primarily at the electrodes rather than being transported from the bulk. This effect, known as feedback [14], is further discussed in section 1.2.1 and in chapter 4. High current densities are also achieved under this circumstance.

It is worth noting that a steady-state response can be obtained at any potential, regardless to i) whether the electrochemical reaction is under kinetic or diffusion control, and ii) whether the potential is stepped or slowly scanned to the value. Moreover, a unique relationship between current and potential leads to an identical steady-state value either by galvanostatic or potentiostatic means [17].
For a reaction that is under diffusion control, the diffusion layer generated by a microdisk is akin to that of a minute hemisphere. The steady-state current of a microdisk can thus be approximated by that of a micro hemisphere if the microdisk is given a corresponding surface diameter. The same argument applies to the quasi steady-state response of microbands and micro hemicylinders [18-21].
When heterogeneous and homogeneous kinetic effects are involved, new relationships of equivalence involving rate constants must be devised [9]. This is caused by the fact that cylindrical and spherical electrodes display a uniform current density owing to diffusion flux lines perpendicular to the whole surface, whereas sharp bending of flux lines at the edges of a planar (flat) microelectrode leads to a non uniform distribution of current density. Corresponding infinite values of current density at the edges and non uniform concentration distribution at the electrode surface can significantly affect both homogeneous and heterogeneous processes.

1.1.3 Reduced ohmic drop

The ohmic drop, defined as the product of the current and the resistance in solution, represents a fraction of the applied potential that has no incidence on the charge transfer process and that possibly distorts the analytical data. Marked effects are observed in low conductivity electrolytes and/or when large currents are generated, e.g. at short experimental time scales. Owing to the fact that the electrical field lines converge towards the electrode surface in the case of a microelectrode, the resistance in solution induced by a microelectrode is several orders of magnitudes larger than that at a conventional electrode. Yet, the small current intensity generated at the minute surface area tends to balance such large resistance, leading to good immunity to ohmic distortions. The ratio of the current density over the ohmic drop demonstrates the ohmic superiority of the point and line geometry over the plane electrode.

When a converging diffusion rules the mass transport, the highest current density in solution is found in close vicinity of the electrode surface and the major part of the ohmic drop takes place across that region. The effective solution resistance at a point electrode is inversely proportional to the microelectrode radius (table 1.1). At long experimental time scales, i.e. under a steady-state diffusion regime, the Faraday current magnitude varies linearly with the electrode radius. The product of both the resistance and the steady-state current is therefore independent of the electrode size [22,23].
At short time scales, during which planar diffusion conditions are applicable, the Faraday current and the eventual charging current are proportional to the electrode area. The ohmic drop shows a linear relationship with the electrode radius. The same applies to kinetically controlled reactions, for which the Faraday current is again proportional to the electrode area. Ohmic distortions can thus be greatly minimized in both situations by reducing the dimensions of the electrode, bearing in mind that for a given experiment duration, the mass transport must stay under planar diffusion regime [24]. Hence, ohmic drop is either beneficially affected by miniaturization or independent of it.

1.1.4 Improved time constant and signal to noise ratio

Provided that the characteristic dimension of the microelectrode is larger than the double layer thickness, or assuming that the specific double layer capacitance is not affected by the size reduction, the capacitance is only affected by the surface area of the interface. A reduction of the electrode dimensions proportionally decreases the capacitance and lowers the time constant of the system.
The ratio of the Faraday to charging current will depend on the diffusion regime. At time scales for which a microelectrode is under planar diffusion, both the Faraday and the charging current are proportional to the electrode area. The signal to noise ratio is in this case similar to that obtained at a macroelectrode. Under a steady or a quasi steady-state diffusion regime, the Faraday current shows a linear relationship with the smallest geometric dimension of the microelectrode. Since the charging current remains proportional to the electrode area, a much more favorable signal to noise ratio is achieved and can be further improved by reducing the microelectrode characteristic dimension.

1.1.5 Small current intensity

In spite of the fact that a reduced amperometric response is considered as a beneficial aspect in specific applications, i.e. small consumption of reactants causing minimal interferences with the medium, the small current intensity generated by microelectrodes is generally regarded as a major drawback. The measurement of such low currents most frequently requires the use of a Faraday cage to minimize external noise pick-up and a high gain current-to-voltage converter. A method for increasing the current to be measured is to use an array of widely separated and non interacting microelectrodes. Under these conditions, a current response scaled up by the number of elements forming the array can be obtained. Most of the microelectrodes properties will qualitatively remain comparable [9,24-29]. An alternative approach consists in exploiting the electrochemical amplification described in section 1.2.1, and which arises from a feedback effect between closely-placed anodes and cathodes. This approach is exclusively restricted to reversible or quasi-reversible electrochemical processes.

1.2 Microelectrode Arrays

Different geometries have been considered for the construction of ensembles of microelectrodes. These include i) regular arrays presenting a periodical arrangement of identical electrodes with the same dimensions, and ii) arrays of disordered microelectrodes, featuring a random pattern of either identical or dissimilar microelectrodes. Most of the classical fabrication procedures that have been successfully applied to the manufacture of individual microelectrodes are generally not suitable for the fabrication of regular arrays. This is mostly due to the technological difficulty in controlling the interelectrode spacing when dealing with a large number of electrodes. Yet, arrays of microbands and microdisks, respectively, have been fabricated by polishing cross sections of stacked metallized laminates [30,31] and gold minigrids sealed in an epoxy matrix [32]. A large variety of randomly ordered arrays exhibiting interesting analytical properties have also been constructed by embedding carbon fiber bundles or ensemble of metallic microwires in an insulating matrix [25,33-35], or by filling reticulated vitreous carbon with epoxy [36]. Microporous alumina membranes have also been advantageously used as template for the fabrication of random arrays, by either electrodepositing different conducting materials through the pores of the host membrane or by filling the pores with conductive pastes [28,37,38].

Regular arrays with well defined electrode dimensions and interelectrode spacing have been generally constructed by photolithographic means. One of the earliest report was made by Gueshi et al. [39,40]. The authors used photolithography to produce hexagonal arrays of gold microelectrodes. Using the same technology, Aoki and Osteryoung have proposed regular microdisk arrays of various geometry on glassy carbon substrates [41]. A large number of contributions have been published ever since by other groups. As two interesting alternatives to the photolithographic approach, Seddon et al. [42,43] have demonstrated the convenience of U.V. excimer laser photoablation of polymeric dielectric films for the fabrication of microdisk arrays and Magee et al. [44] have described the construction of microband arrays by filling with epoxy grooves cut in a glassy carbon surface.

1.2.1 Properties of regular arrays

The most frequently-adopted periodic arrangements are the quadratic or hexagonal assembly of microdisks, and the parallel arrangement of microbands. These geometries are usually preferred as the modeling of their electrochemical behavior is more convenient because of the symmetrical aspect of the arrangement. There are two distinct effects arising from the close proximity of microelectrodes assembled in arrays, namely shielding and feedback [14]. These particular electrochemical features occur when the diffusion layers developing at each element interact one with another.

shielding

Shielding is specific to ensembles of densely-packed microelectrodes that are all operated simultaneously at the same potential. Under certain experimental conditions, the interelectrode spacing may not be sufficient to prevent the coalescence of each individual diffusion layer (fig. 1.2a). This overlap results in the creation of an apparent planar diffusion layer extending all over the array. In the case of a diffusion-limited reaction, the array behaves as a large electrode whose surface corresponds to the total surface area, i.e. the sum of the active A_{el} and non active parts A_{ins} of the array. Since the electrochemical response is in this case proportional to the total surface area, and both the capacitive and the electrochemical noise pickup are only proportional to the active area, the signal to noise ratio is theoretically improved by a factor close to $(1+A_{el}/A_{ins})$ [9,24,37]. The issue has been thoroughly addressed by Weber using noise models from different sources [27].

On the other hand, shielding can be avoided with arrays of loosely-packed microelectrodes, i.e. if the interelectrode spacing is sufficiently large to

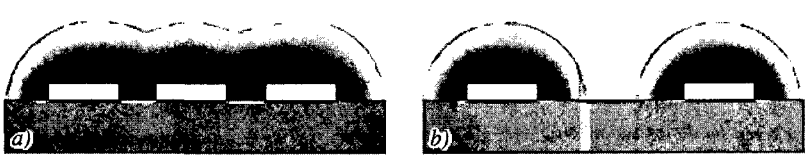

Figure 1.2: Schematic drawing of the diffusion layers at microelectrodes operated at the same potential. a) Densely-packed microelectrode array (occurrence of shielding). b) Loosely-packed array (overlap of the diffusion layers is avoided).

prevent the coalescence of the individual diffusion layers (fig. 1.2b). The amperometric response is in this case exactly equal to that given by the sum of each individual responses [45]. Therefore, the array plays the role of a current amplifier, with a gain factor corresponding to the number of elements forming the array. It has been suggested in the case of hexagonal microdisk arrays, that the minimal interelectrode spacing corresponds to 5-10 times the microdisk radius [46].

feedback

Feedback effect is observed when a number of conditions are met, i) the diffusion layers of closely spaced anode and cathode overlap, ii) the charge transfer process is reversible or quasi reversible, iii) and the electrodes are respectively biased at the adequate oxidation and reduction potentials.

When a reversible or quasi reversible redox couple is present in solution, one of the redox forms of the species can be generated at one electrode (generator) and collected at the adjacent electrode (collector). It is converted there to its initial state by the reverse reaction (fig. 1.3). Some parallels with the electrochemical generation-collection experiments of the type carried out at rotating ring-disk electrodes can be drawn, however with the exception that the generated species detected at the collector electrode can in the present case diffuse back to the generator electrode as regenerated species. An additional amount of reactant is thus provided to the generator electrode. The multiple oxidation and reduction processes

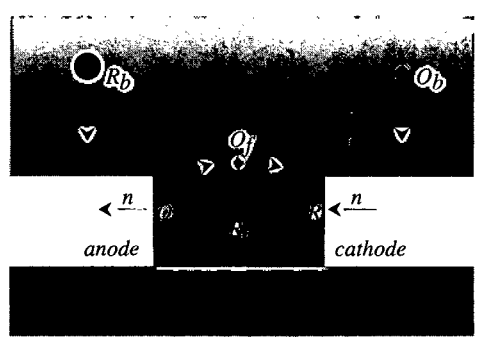

O: oxidation
R: reduction
R_b, O_b: reactants from the bulk
R_f, O_f: feedback reactants
n: exchanged electrons

Figure 1.3: Redox cycling of a reversible species at closely spaced anode and cathode

(redox cycling) significantly increases the amperometric response of both the generator and the collector electrodes. In addition to this electrochemical amplification, redox cycling prevents the depletion of electroactive species at the vicinity of the electrode surface. The electroactive species participating in the reaction are primarily generated at the closely-spaced electrodes rather than being transported from the bulk. Therefore, the evolution of the diffusion layer towards the bulk solution is limited, and steady-state concentration profiles of oxidized and reduced species are established within the interelectrode spacing.
The most popular electrode geometry used for feedback experiments is that of planar interdigitated arrays of microbands, consisting in two separate sets of microbands that can be individually biased. Yet, alternate approach based on vertically separated microelectrodes arrays has been reported [47-49]. These are generally built by the successive deposition and patterning of two dielectric and metal layers, on top of a large planar electrode. In this case, the interelectrode spacing is determined by the thickness of the insulating material that separates the upper from the lower electrode.

1.2.2 The thin-film technology

Thin-film microelectrodes are formed on a substrate by the successive deposition and patterning of different material layers with thicknesses of usually less than a micron. Most of the technological processes involved in the fabrication of such devices have been developed for the integrated circuits industry.
The deposition of the thin metallic films is generally carried out by the evaporation or the sputtering of a solid metal source. Thin dielectric coatings are obtained by various forms of chemical vapor deposition or by the use of spin-on materials. The patterning of these materials is performed by selectively protecting the thin-film to be patterned, so that unprotected parts can be etched in solution or plasma. Photolithography has been developed to this end and provides means for transferring the image of a pattern onto the substrate. A thin layer of light sensitive material (photoresist) is applied to the substrate. The photoresist is exposed to U.V. radiation through a quartz mask onto which the desired pattern has been made in chromium. Exposed areas of the photoresist are either made

soluble (positive photoresist) or insoluble (negative photoresist) in a developing solution. The patterned photoresist acts as a mask, protecting the underlying film during the subsequent etch. Once the etching of the thin-film has been completed, the photoresist mask is stripped from the surface in the appropriate solvent or in oxygen plasma.

The most attractive aspect of the thin-film technology stems from the facility to generate a complex geometry in thin-film materials, at a dimension scale defying the use of conventional machining techniques. For this reason it has been recognized as a suitable mean for the fabrication of planar and regular microelectrode arrays. To the best of the author's knowledge, the earliest work on microdisk arrays fabricated by photolithography has been reported by Gueshi et al. in 1978 [39]. The growing interest among the electrochemical community has been embodied by a number of communications published ever since. The minimal feature size for these thin-film microelectrode arrays has been continuously challenged and to the present date, ensembles of microdisks with a radius as small as 0.375 μm [41] and arrays of microbands with a gap of 0.3 μm have been fabricated [50].
The tight control of the fabrication steps insures a good reproducibility of the microelectrode characteristics. It should be pointed out that polishing of the electrode surface is not possible due to the limited thickness of the electrode material. Yet, this procedure does not prove to be necessary since the electrochemical properties of the "as produced" microelectrodes are generally satisfactory and remain acceptable for a short term and a disposable use.

1.3 Objectives and Outline of the Work

The first objective of this work consists in the development and the optimization of the thin-film technology to produce carbon and iridium microelectrode arrays. These two electrochemically interesting and important materials have either proven to be difficult to adapt to the thin-film technology, or not been utilized until recently. The second objective deals with the conception and the fabrication of a prototype for the purpose of electrochemical imaging, by choosing the approach of "on chip" integrated electronic addressing unit.

Chapter 2 presents the sequence of the technological steps that have been used to fabricate the different arrays, and gives a general overview of the thin-film technology. Some aspects of photolithography, material deposition and patterning are discussed. Reference to the pertinent literature is made.

Chapter 3 deals with ensembles of iridium microdisks, simultaneously operated at the same potential, as substrates for the formation of mercury thin-film microelectrode arrays. These device have been developed for the detection of trace metals in environmental and medical applications. The electrochemical behavior of the fabricated iridium microdisk arrays with or without the deposition of the mercury, and the analytical performances of the device are presented.

Chapter 4 presents the development of a low temperature process for the deposition of thin-film carbon layers showing good electrocatalytic properties. The morphology and the electrochemical behavior of the carbon layer are thoroughly investigated. The electroanalytical potentialities of these carbon thin-films are demonstrated by the fabrication of interdigitated microelectrode arrays for the detection of a biologically important molecule and a pharmaceutical compound.

Chapter 5 demonstrates the concept of electrochemical mapping performed with individually addressable microelectrodes, and uses an original architecture for on "on-chip" multiplexing. Preliminary electrochemical images are shown. The results of this feasibility study will be exploited for the determination of the trace metal concentration gradients at interfaces, i.e. water/sediment and water/air, with the devices described in chapter 3.

References

[1] Wightman R.M., Anal. Chem., 53 (1982), 1125A-1134A

[2] Pons S., Fleishmann M., Anal. Chem., 59 (1987), 1391A-1399A

[3] Wightman R.M., Science, 240 (1988), 415-420

[4] Aoki K., Electroanalysis, 5 (1993) 627-639

[5] Heinze J., Angew. Chem. Int. Ed. Engl., 32 (1993) 1268-1288

[6] Bond A.L., Analyst, 119 (1994) R1-R21

[7] "Ultramicroelectrodes", Fleishmann M., Pons S., Rolison D.R., Schmidt P.P., Datatech, Moraganton, NC, 1987

[8] "Microelectrodes: Theory and Applications", M.I. Montenegro, A.A. Queiros, J.D. Daschbach, Kluwer Academic Publishers, Dordrecht, The Netherlands, 1990

[9] Amatore C. in "Physical Electrochemistry: principles, methods and applications, Rubinstein I., Marcel Dekker, New-York, 1995, 131-208

[10] Morf W., de Rooij N.F., Sensors and Actuator A, 51 (1995) 89-95

[11] Pletcher D. in ref. [7], 3-16

[12] Norton J.D., White H.S., Feldberg S.W., J. Phys. Chem., 94 (1990) 6772-6780

[13] Morris R.B., Franta D.J., White H.S., J. Phys. Chem., 91 (1987) 3559-3564

[14] Bard A.J., Crayston J.A., Kittlesen G.P., Varco Shea T., Wrighton M.S., Anal. Chem., 58 (1986) 2321-2331

[15] Bard A.J., Faulkner L.R., "Electrochemical Methods: fundamentals and applications", John Wiley and Sons, New York, 1980

[16] Oldham K.B., in ref. [7], 276-287

[17] Zoski C.G, Bond A.M., Allinson E.T., Oldham K.B., Anal. Chem. 62 (1990) 37-45

[18] Oldahm K.B., Zoski C.G., J. Electroanal. Chem., 256 (1988) 11-19

[19] Oldham K.B., J. Electroanal. Chem., 122 (1981) 1-17

[20] Coen S., Cope D.K., Tallman D.E., J. Electroanal. Chem., 215 (1986) 29-48

[21] Deakin M.K., Wightman R.M., Amatore C.A., J. Electroanal. Chem., 215 (1986) 49-61

[22] Bruckenstein S., Anal. Chem., 59 (1987), 2098-2101

[23] Oldham K.B., J. Electroanal. Chem, 237 (1987), 303-307

[24] Reller H., Kirowa-Eisner E., Gileadi E., J. Electroanal. Chem., 161 (1984) 247-268

[25] Strohben W.E., Smith D.K., Evans D.H., Anal. Chem., 62 (1990) 1709-1712

[26] Cassidy J., Ghoroghchian J., Sarfarazi F., Smith J.J., Pons S., Electrochim. Acta, 31 (1986) 629-636

[27] Weber S.G., Anal. Chem., 61 (1989) 295-302

[28] Cheng F.I., Whiteley L.D., Martin C.R., Anal. Chem., 61 (1989) 762-766

[29] Ahmad K., Brajter-Toth A., Anal. Chim. Acta, 259 (1992) 139-144

[30] Varco Shea T., Bard A.J., Anal. Chem., 59 (1987) 2101-2111

[31] Bartlet J.E., Deakin M.R., Amatore C., Wightman R.M., Anal. Chem., 69 (1988) 2167-2169

[32] Wu H.P., Anal. Chem., 65 (1993) 1643-1646

[33] Caudill W.L., Howell J.O., Wightman R.M., Anal. Chem., 54 (1982) 2532-2553

[34] Ciszowska M., Stojek Z., J. Electroanal. Chem., 191 (1985) 101-110

[35] Morita K., Shimizu Y., Anal. Chem., 61 (1989) 159-162

[36] Sleszinski N., Osteryoung J., Carter M., Anal. Chem., 56 (1984) 130-135

[37] Penner R.M., Martin C.R., Anal. Chem., 59 (1987) 2625-2630

[38] Cheng I.F., Martin C.R., Anal. Chem., 60 (1988) 2163-2165

[39] Gueshi T., Tokuda K., Matsuda H., J. Electroanal. Chem., 89 (1978) 247-260

[40] Gueshi T., Tokuda K., Matsuda H., J. Electroanal. Chem., 101 (1979) 29-38

[41] Hepel T., Osteryoung J., J. Electrochem. Soc., 133 (1986) 752-757

[42] Seddon B.J., Shao Y., Fost J., Girault H.H., Electrochim. Acta, 39 (1994) 783-791

[43] Seddon B.J., Shao Y., Girault H.H., Electrochim. Acta, 2377-2386

[44] Magee L.R., Osteryoung J., Anal. Chem., 61 (1989) 2124-2126

[45] Morf E.W., "Theoretical Treatment of the Amperometric Current Response of Multiple Microelectrode Arrays", *in press*

[46] West A.C., J. Electrochem. Soc., 140 (1993) 134-139

[47] Niwa O., Morita M., Tabei H., J. Electroanal. Chem., 267 (1989) 291-297

[48] Niwa O., Morita M., Tabei H., Electroanalysis, 3 (1991) 163-168

[49] Horiuchi T., Niwa O., Morita M., Tabei H., J. Electrochem. Soc., 138 (1991) 3549-3553

[50] Paeschke M., Wollenberger U., Köhler C., Lisec T., Schnakenberg U., Hintsche R., Anal. Chim. Acta, 305 (1995) 126-136

Fabrication Process

The widest and most demanding application of thin-film technology is undoubtedly found in microelectronics. Most of the processes and equipment developed for the integrated circuits industry can be conveniently adapted to the fabrication of microelectrodes. This approach enables a large variety of planar designs such as regular arrays, difficult to obtain in a reproducible manner by other conventional means. This section illustrates some aspects of the thin-film technology by introducing the fabrication steps that are used to realize the microelectrode arrays of chapter 3, 4 and 5. A brief account of the relevant deposition, photolithography, patterning processes is given. More details are found in the suggested literature [1-7].

2.1 Introduction

Thin-film microelectrode arrays are built by the successive deposition and patterning of dielectric and conductive materials, on top of an optically flat and polished substrate. Due to the background of most technological steps, the choice of a silicon wafer as starting substrate is probably the most suitable. Silicon additionally offers the opportunity to conceive complex systems such as those including integrated signal processing units and/or bulk micromachining [8-10], temperature diodes and pH sensitive field effect transistors [11]. Chapter 5 will present the case where a multiplexing function has been integrated "on-chip" to individually address thin-film microelectrodes. If the electronic or crystallographic properties of silicon are not required, any material withstanding the different fabrication processes could alternatively be used [12].

The silicon wafer is first insulated by the deposition of a thin dielectric film. This layer is referred to as the bottom passivation (fig. 2.1a). Its prime function is to prevent any chemical reaction of the substrate with the species present in the electrolyte solution, and to electrically disconnect the electrodes from the conductive silicon and from each other. Therefore, the passivation should have good dielectric properties and be chemically inert.

As depicted in figure 2.1 and 2.2a, two strategies can be envisaged to fabricate interdigitated arrays (IDA). In the first approach, the electrode material is deposited on top of the passivated substrate and then covered by a photosensitive resin. The image of the microelectrodes is transferred to the wafer level by photolithography. The patterned resin defines and protects the electrode geometry (fig. 2.1b). The exposed parts of the electrode material are removed by a wet or dry etch process. The resin is then stripped, leaving a patterned electrode material on the substrate. This procedure suits the fabrication of Au or C electrodes. In the second approach, the photosensitive resin is first deposited on the passivated substrate. The reversal image of the electrodes is transferred to the wafer level by photolithography (fig. 2.1c). The patterned resin is then covered by the deposition of the electrode material. The electrode geometry is revealed by dissolving the underlying resin, thus removing from the substrate unwanted parts of the electrode material. This so-called "lift-off" technique is particularly interesting for the fabrication of Pt or Ir electrodes, or any other material for which etch processes are not compatible with photoresist masking.

In most cases, a passivation layer is finally deposited on top of the substrate and etched to only expose the active surface of the electrodes and bonding pads (fig. 2.1d). This top layer offers the same properties as the bottom passivation, and additionally provides a good protection against mechanical damages (scratches). Ensembles of microelectrodes, such as microdisk arrays, can simply be produced by etching multiple openings in the top passivation (fig. 2.2b). As this alternative does not require the patterning of the electrode material, each element of the array is part of the underlying electrode thin-film and all microdisks inevitably operate in parallel.

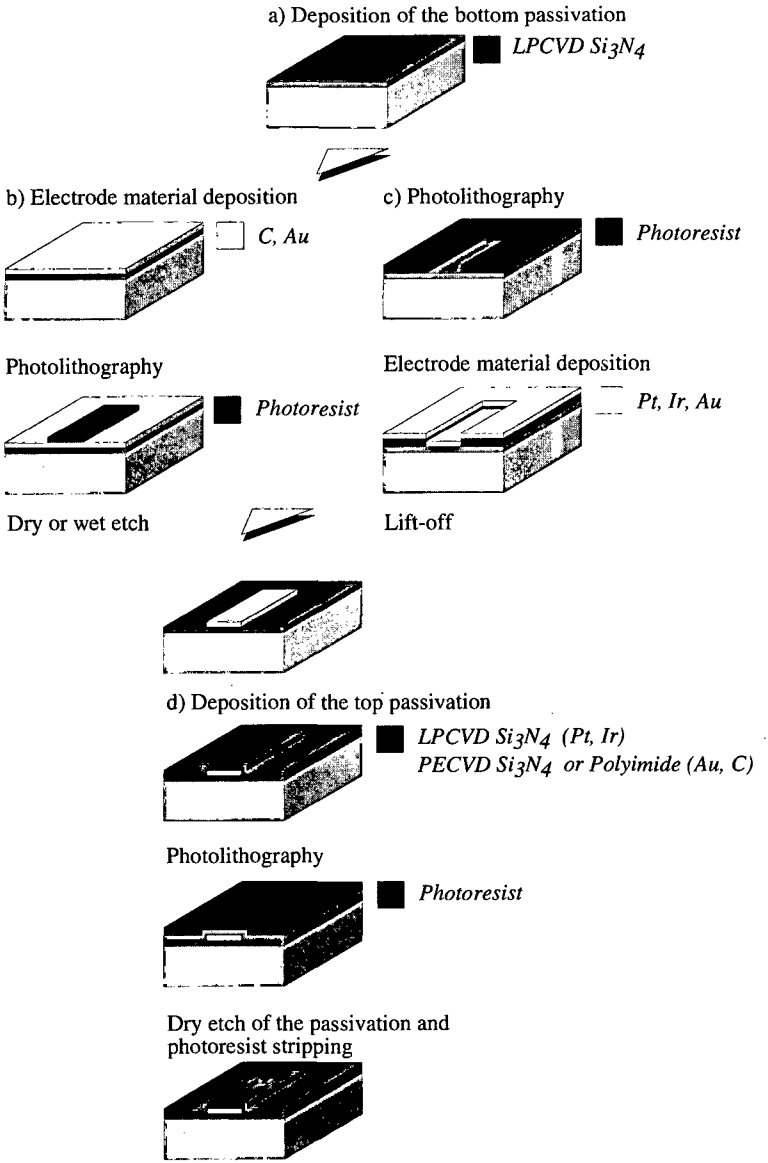

Figure 2.1: Sequence of the technological steps.

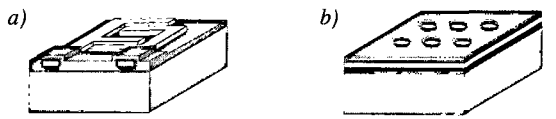

Figure 2.2: a) Interdigitated structure obtained by patterning the electrode material. b) Array of microelectrodes generated by etching multiple openings in the top passivation layer.

The wafer is saw-diced or cleaved into individual devices. Each chip is mounted on a printed circuit board (PCB) and is electrically connected either by wire bonding or via a conductive silver epoxy resin (epo-tek® H20E, Polyscience) to the PCB copper lines. These interconnections and the PCB are carefully encapsulated with an epoxy resin (Araldite® AY105/HY991, Ciba) to prevent interfering chemical and electrochemical reactions when the mounted device is exposed to the measurement media (fig. 2.3). The encapsulation procedure has been described in details by Gernet et al. [13].

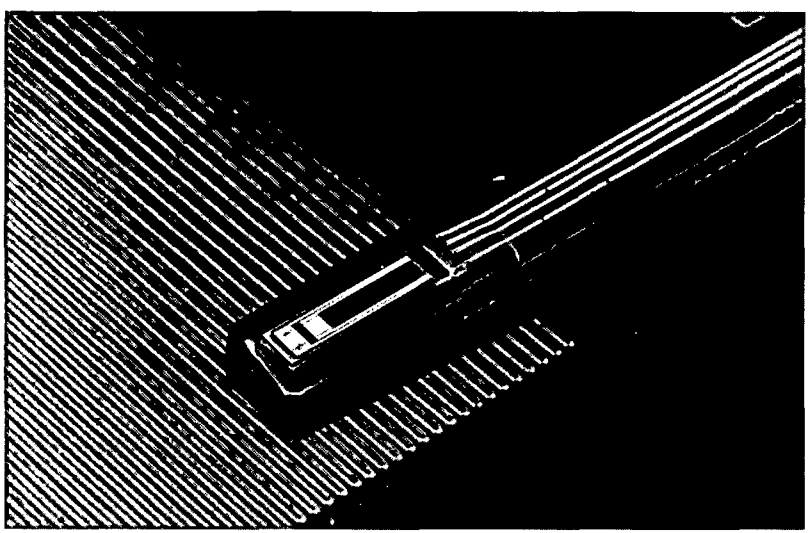

Figure 2.3: Photograph of a mounted and encapsulated interdigitated microelectrode array; width of the PCB: 6 mm.

2.2 Photolithography

Photolithography is the process by which geometric patterns are transferred from a mask to a photosensitive material (photoresist) covering the substrate surface. The mask is a transparent quartz frame, that contains opaque chromium features representing the geometry of the microelectrode array at one particular step of the fabrication. The pattern transfer is performed by shinning an ultraviolet light onto the photoresist through the mask. Exposed regions are either made soluble (positive photoresist) or insoluble (negative photoresist). The photoresist patterns are revealed in the appropriate etching solution (developer).

Positive photoresists are composed of a photo active compound (PAC), a base resin, a casting solvent and other additives. Upon exposure to the proper light source, the PAC undergoes a photochemical reaction that changes its molecular structure and converts it into a soluble acid species. This compound is later on dissolved in an alkaline developer. The patterns of the remaining resist are the same as those of the mask. Negative photoresist contains a polymer combined with a PAC, that initiates a crosslinking reaction upon light exposure. As the crosslinked polymer becomes insoluble, patterns formed in negative photoresist are the reverse image of those of the mask. Until recently, negative photoresists were known to offer a limited resolution (3-5 μm) when compared to that of positive photoresists (0.5-3 μm). This limitation was caused by the swelling of photoresist in the organic solvents used in the development step. More recent negative photoresists offer an improved resolution (0.8-3 μm) and a development without swelling in a simple alkaline solution (table 2.1).

name	*manufacturer*	*type*	*application*	*resolution*
AZ 1518	*Hoechst*	*positive*	*multipurpose*	*≈ 1 μm*
AZ 4562	*Hoechst*	*positive*	*plasma etch*	*≈ 3 μm*
OMR 83 60cp	*Microposit*	*negative*	*wet etch*	*≈ 3 μm*
ma-N 420	*Micro allresist*	*negative*	*multipurpose*	*≈ 1 μm*

Table 2.1: List of the employed photoresists and achieved resolution

(AL6 Electronic Visions, Austria). Alignment marks are usually added on the mask to simplify the alignment of the subsequent photolithographic steps. The wafer and mask are then either brought in direct contact with one another or in close proximity (2-10 μm). The intimate contact between the wafer and the mask is attractive, as it minimizes the diffraction effects on the edges of the mask patterns and provides the highest resolution. Contact printing however is penalized by two major drawbacks, i) special care must be taken to prevent dust particles to fall on the wafer surface and physically damage the mask during contact printing, and ii) sticking of photoresist to the mask can be observed with poorly cleaned mask or incomplete prebake. The light source is a high pressure mercury lamp, whose spectral lines of interest are 365 nm (i-line), 405 nm (h-line) and 436 nm (g-line). For a given lamp intensity, the exposure time is set in order to provide the required amount of energy necessary for a successful pattern transfer. Energy requirements are specific for each photoresist and are generally in the range of 10-100 mJ/cm^2 (table 2.2)

development

Unwanted part of photoresist are dissolved in the appropriate developer (table 2.2). Developed wafers are thoroughly rinsed in DI water and blown dry with nitrogen.

photoresist	*exposure energy*	*developer*	*developing time [s]*
AZ 1518	*55 mJ/cm^2*	*AZ351/DI H_20 1:4*	*60*
AZ 4562	*240 mJ/cm^2*	*AZ351/DI H_20 1:3*	*90*
OMR 83 60 cp	*25 mJ/cm^2*	*varsol*	*70*
		heptane	*30*
		n-butyl acetate	*30*
ma-N 410	*300 mJ/cm^2*	*ma-D 532*	*60*

Table 2.2: Exposure energy and development parameters according to the proprietary recipes. The development of unexposed OMR negative photoresist requires the succession of varsol, heptane, and n-butyl acetate steps.

postbake

A postbake of 30 minutes at 120 °C in a convection oven is carried out as a curing step to further stabilize the photoresist. Since it generally improves the photoresist adhesion, postbake should be carried right before wet etch processes.

2.2.2 Stripping procedures

Positive photoresist and recent negative photoresist counterparts are readily stripped in acetone. When more drastic stripping procedures are required, i.e. after a dry etch process, stripping can be carried out in oxygen plasma or in a H_2SO_4/H_2O_2 mixture. In the latter approach, care has to be taken when Pt and to lesser extent Ir are present on the wafer, as the catalytic properties of both noble metals will promote the chemical reaction. Significant formation of H_2 and increase of the solution temperature may lead to hazardous process conditions. The wafer is then immersed for 10 minutes in 64% H_2SO_4. Several milliliters of 30 % H_2O_2 are gradually and slowly poured for the reaction to proceed right above the wafer surface. The wafer is withdrawn from the solution after 10 minutes, thoroughly rinsed in DI water and blown dry with N_2.

2.3 Thin-Film Deposition

2.3.1 Electrode materials

platinum, iridium and gold

Noble metals, such as Pt, Ir and Au are deposited as thin-films by electron gun evaporation (e-gun). The source material is placed in a crucible and heated by a focused e-beam under high vacuum conditions. The vapor pressure of the metal exceeds that of its environment and a vapor phase is generated. Upon contacting the cooler surface of the substrate, the vapor condenses by a mechanism of nucleation and growth of the film. Sequential depositions of different metallic films are possible without breaking the vacuum when multiple material sources are available in the deposition chamber.

To be of any practical use, the thin-film must adhere firmly to the insulated substrate. The adhesion of noble metals on passivated substrates is usually enhanced by the use of intermediate layers evaporated prior the noble metal deposition. Ti and Ta are the most frequently used adhesion promoters for Pt, Ir, and Au. These transition metals chemically bind to the silicon oxide and nitride by oxide formation [4]. An eventual intermetallic compound is formed between the adhesion promoter and the noble metal, thus creating a strong binding. The use of Cr as adhesion promoter is avoided in our case, as large interdiffusion of Cr in the noble metal has a detrimental effect on the electrochemical response of the electrode [13].

The equipment and operating conditions used for our depositions are reported in the following table.

substrate temperature	*< 100 °C*
pressure	*10^{-6} mTorr*
deposition rate	*5-10 Å/s*
film thickness	*100-2000 Å*

Table 2.3: Typical operating conditions for e-gun evaporation with a Temescal reactor (USA).

carbon

In collaboration with the "Centre Suisse d'Electronique et de Microelectronique" (CSEM, CH), a deposition process of carbon thin-films for electrochemical applications has been developed. The deposition is performed by radio frequency (RF) magnetron sputtering technique. In sputter depositions, a target made of the material to be deposited is bombarded with highly energetic particles. Through momentum transfer, surface atoms of the target are ejected and eventually condense as a film onto the substrate. Inert gases (Ar, Ne) in their ionized form are commonly used as incident particles, ensuring that no chemical activity between the bombarding particles and the target material takes place.

The sputtering system is composed of a vacuum chamber in which two parallel plates serve to generate a glow discharge, and create a potential difference that accelerates the ionized particles towards the target. In our case, a hot pressed C target forms the cathode and the substrate to be coated is placed on a substrate holder acting as the anode (fig. 2.5). The latter electrode can be electrically bias, grounded or floating. The inert gas is then introduced into the system, and a glow discharge (plasma) is created by applying a large potential difference between both electrodes. Ionized positive particles are accelerated towards the cathode. Upon striking the target, neutral C atoms are ejected from the surface and additional electrons are emitted. These are attracted by the anode and eventually interact again

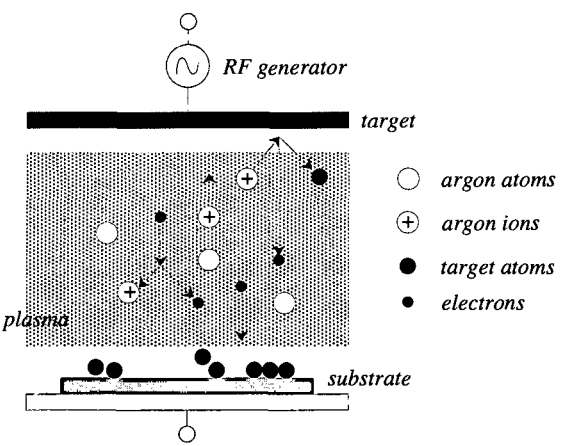

Figure 2.5: Schematic of the glow discharge sputtering process.

with the neutral gas particles. More ionized species and electrons are generated, and a self sustaining glow discharge is formed. The plasma is generated on a RF mode at one of the standard industrial wavelength (13.56 MHz).

As the deposition occurs through momentum transfer, the kinetic energy and the respective masses of the bombarding particles and the target atoms are fundamental aspects of the sputtering process. By controlling the energy and the nature of the incident particles, the crystallographic arrangements of the thin-film can be conveniently modified to obtain specific physical properties [14]. To achieve a low bulk resistivity ($\approx 10^{-3}$ Ωcm) and a good film adhesion, several deposition parameters have been adjusted. These include the choice of the sputtering gas, the pressure of the gas, the distance between the target and the substrate, the substrate bias and the deposition temperature. The energy of the bombarding particles is controlled by the pressure of the gas, the distance separating the target from the substrate and the substrate bias. The values of pressure and electrode distance can only be varied within the limits of the operation window allowing a glow discharge process to occur. By negatively biasing the substrate, the amount of positively charged ions is increased up to a point where the deposition process enters in competition with the sputtering of the thin-film itself. The substrate bias is tuned to allow a net deposition at a convenient rate.

The temperature of the substrate and the target, the structure of the target material itself and the flux of the inert gas have non negligible effects on the film characteristics. Mainly intended as a low temperature deposition process, effort is put on maintaining the substrate temperature below 120°C by using a water-cooled substrate holder. The values of the resistivity are obtained with deposition temperatures not exceeding this values.

Good adhesion of sputtered C films onto the passivated substrate is achieved without using adhesion promoters. For the optimized operating conditions, the energetic bombardment of the film during growth shows a beneficial effect on the adhesion performances. This improvement is probably induced by the constant "cleaning" action of the incident particles during the early stage of nucleation, and other phenomena altering the interface formation [2].

The deposition parameters are propriety of the CSEM and cannot be disclosed.

2.3.2 Passivation materials

Silicon nitride (Si_3N_4) offers attractive characteristics such as a high dielectric strength, a high specific resistivity, and a near imperviousness to water and to the diffusion of alkali ions. For these reasons, it is extensively used as passivation material. Despite the fact that silicon oxide (SiO_2) is an excellent dielectric, it is less used as it shows poorer passivating characteristics in aqueous media than Si_3N_4. The deficiencies compromising its protective performances are a relative permeability to alkali ions, that may possibly cause the shortening of electrodes, and its susceptibility to hydrate. In that respect, SiO_2 is rarely utilized by itself, but is combined with an additional stable and inert ion barrier on top of it, such as aluminum oxide (Al_2O_3) or Si_3N_4 [13]. Whereas low pressure chemical vapor deposition (LPCVD) has proven to be a safe deposition method to form a Si_3N_4 passivation on top of Ir or Pt thin-films, the relatively high process temperature and the HCl formation preclude its use when C, Au or Al are present on the substrate. Lower temperature deposition techniques, such as plasma enhanced chemical vapor deposition (PECVD) or spin-on materials must be used in these particular cases.

LPCVD silicon nitride

The deposition of Si_3N_4 thin-films is obtained by the chemical reaction in vapor phase of selected gases. Optimal protective characteristics are generally achieved using a LPCVD process. The reduced pressure increases the mass transport of the gas molecules, and consequently facilitates the achievement of a good step coverage and an improved conformality. Silicon nitride, having a composition very close to the stochiometric Si_3N_4, is formed by the chemical reaction of dichlorosilane ($SiCl_2H_2$) and ammonia (NH_3):

$$3SiCl_2H_2 + 4NH_3 \rightarrow Si_3N_4 + 6HCl + 6H_2 \quad (2.1)$$

The deposition is carried out in hot-wall reactor (Tempress Systems, NL) at a temperature of 800 °C and a pressure of 200 mTorr. Temperature, pressure and the flow of the gas mixture are set in order to achieve homogeneous depositions at a rate of 40 Å/min. The resulting films are dense and practically free of pinholes. Their thickness is usually kept below 2500 Å,

due to a built-in tensile stress. Thickness and refractive index are measured by ellipsometry (Gaertner, USA). As the value of the refractive index is strongly related to the film composition, its measure provides a convenient test to assess the reproducibility of the deposition process. High refractive indexes are relevant of silicon-rich films, whereas low indexes are indicative of oxygen contamination. The characteristics of LPCVD Si_3N_4 are summarized in table 2.4.

PECVD silicon nitride

PECVD is an interesting alternative to access deposition of Si_3N_4 thin-films at the reduced temperature of 400 °C. The chemical reaction is promoted by the generation of reactive species in a glow discharge environment. A plasma of silane (SiH_4) and NH_3 is used to produce a hydrogenated form of silicon nitride:

$$SiH_4 + NH_3 \rightarrow SiNH + 3H_2 \quad (2.2)$$

The plasma is generated in a cold wall reactor (STS, GB), at a pressure of 800 mTorr and in a 13.56 MHz RF discharge of 25 W. The deposition rate is about 130 Å/min. The film composition significantly departs from the stochiometric Si_3N_4, as hydrogen is usually incorporated in the film structure during growth. Despite the fact that both LPCVD and PECVD silicon nitrides have comparable dielectric properties in dry conditions (table 2.4), PECVD thin films are generally known to offer poorer passivation performances in liquids than LPCVD thin-films.

spin-on polyimide

Polyimides have found a wide acceptance in microelectronics applications as

	LPCVD Si_3N_4	*PECVD Si_3N_4*	*PI 9103-25[a)]*
process temperature	*800 °C*	*400 °C*	*400 °C*
film thickness	*2000 Å*	*2000 Å*	*5 µm*
refractive index	*2.0*	*2.0*	*NA[b)]*
dielectric constant	*6*	*5.6*	*3.1*

Table 2.4: Typical characteristics of LPCVD and PECVD Si_3N_4, and Bectron PI 9103-25. [a)] extracted from the proprietary data sheet; [b)] not available.

dielectric interlayer and passivation for integrated circuits. Preliminary tests on commercially available polyimide Bectron® PI 9103-25 have shown promising results. Samples were kindly provided by Beck Elektroisolier-Syteme, Division of BASF, Germany. Similarly to photoresist, the deposition of the polymeric material is performed by spin coating. Film thicknesses in the order of 5 μm are achieved with the sequence of 3 seconds at 1000 rpm and 40 seconds at 4000 rpm. The film is first dried in ambient air on a hot plate. The starting temperature is set at 90 °C, raised up to 200 °C, and held at that temperature for 15 minutes. The curing step is performed under nitrogen to prevent oxidation or carbonization of the polymer. The hot plate temperature is raised to 400 °C at a rate of 100°C/hr. The substrate is kept at the maximum temperature for 15 minutes and allow to slowly cool down to room temperature. The dielectric characteristics of the polyimide are reported in table 2.4. The PI 9103-25 can be advantageously exploited as top passivation layer for Au-IDAs. Its use with C thin-films is however not recommended as both materials are patterned similarly in O_2 plasma (§ 2.4.2).

CVD and thermal silicon oxide

Silicon oxide is obtained by a chemical vapor deposition technique. The deposition results from the chemical reaction of SiH_4 and oxygen at low temperature (350-450°C):

$$SiH_4 + O_2 \rightarrow SiO_2 + 2H_2 \quad (2.3)$$

The process is carried out at atmospheric pressure in a in-house built cold wall reactor. Argon is used as neutral gas carrier. CVD SiO_2 film is mostly used as solid doping source, by either adding phosphine (n-type) or diborane (p-type) to the gas mixture. The deposition rate is in the range of 10-20 Å/s and strongly depends on the substrate temperature, the presence and the type of impurities. CVD SiO_2 is densified in nitrogen at 615 °C for 15 minutes. The doping of silicon is performed by driving the impurities in a subsequent high temperature step (1100°C) in nitrogen for 50 minutes.

The high quality SiO_2 used as gate oxide in the field effect transistors of chapter 5 is grown by thermal oxidation of the silicon substrate at 1100 °C under a dry oxygen environment.

2.4 Patterning

As described earlier, two options can be envisaged to generate patterned thin-films. In subtractive processing, selected parts of the substrate film, e.g. electrode material or passivation, are etched away to produce the desired pattern. Photoresist is used as an etch mask that delineates the pattern geometry and protects the underlying film. Etching processes are subdivided in wet and dry etch techniques. Whereas the former is obviously performed in liquids, the latter is mostly generic of plasma processes. Different etching possibilities may come in competition for the patterning of a given material. The preference is usually given to that preserving the photoresist integrity.
In additive processing, e.g. lift-off, the patterned photoresist is used to locally protect the areas where no deposition should occur. The patterned photoresist acts as a vertical standoff evaporation mask. This technique offers an important alternative for the patterning of thin-films, for which no etch process is compatible with photoresist masking. It is frequently applied for the patterning of noble metals.

2.4.1 Wet etch

Wet etch is most simply described by the dissolution of the material in the appropriate chemicals. The etching process primarily involves a redox reaction for metals, and a displacement reaction for inorganic oxides. The reaction product is a soluble salt or complex. The photoresist mask should be resistant to the selected chemicals in order to provide a good protection throughout the patterning process. If this condition cannot be fulfilled, other masking materials have to be considered and consequently etched. Metal or dielectric masks can withstand in some cases more rigorous etching processes, such as in elevated temperature or in strong acids or bases. A list of the etching solutions that are compatible with photoresist masking is summarized in table 2.5. Only approximate values of etch rate are given, as they are largely dependent on the film composition (exact stochiometry, purity) and structure (porosity, density). These must be established experimentally in each case.

aluminum

Metal etching is carried in solution containing strong oxidizing agents. When Al interconnection lines are used, these are etched at 42°C in a solution (Alu-etch) containing 4 parts of H_3PO_4, 4 part of CH_3COOH, 1 part of fuming HNO_3, and 1 part of H_2O. The gas evolution during the etching reaction consists in H_2, NO and NO_2. Eventual formation of gas bubbles as reaction product may inhibit further etch by blocking the reaction sites and lead to unsuccessful pattern transfer. Solution stirring alleviates this problem, and additionally improves the etch uniformity by removing product and bringing fresh reactants to the interface.

gold and platinum

Gold and platinum electrodes can be etched in aqua regia (3 parts of fuming HNO_3, 1 part of HCl). This procedure is however avoided as it destroys the photoresist mask. In that respect, a solution of iodine 1:1 (Au-etch), made of 4 g KI and 1 g I_2 in 40 ml H_2O, is preferred for Au patterning. To the author's knowledge, no simple chemical etch process compatible with photoresist masking has been reported in the literature for Pt.

silicon oxides

Insulating and dielectric materials are in general relatively inert chemically, and hence require highly reactive media. SiO_2 is most exclusively etched in a buffered hydrofluoric acid (BHF). The etch process is carried at room temperature, in a solution containing 7 parts of 40% NH_4F to 1 part of concentrated HF. The etch rate is affected by the density of the material and its impurity content. Undensified CVD films tends to etch about three times more rapidly than densified or thermally grown SiO_2. Moreover, the etch rate increases with the amount of impurities incorporated in the CVD film during deposition. Typical values for a dense and undoped CVD SiO_2 film are in the order of 1000 Å/min.

silicon nitrides

The etch rate of Si_3N_4 in BHF is determined by the presence of oxygen linkage in the film composition. Silicon nitride films very close to the stochiometric composition are generally insignificantly etched in a fluoride solution (5-10 Å/min.). The etching process is carried out in this case at

160 °C in boiling 85% H_3PO_4. Under such harsh environment, photoresist masking is inappropriate and is replaced by a CVD SiO_2 mask. Si_3N_4 etch rate is in the order of 100 Å/min.

material	*chemicals*	*etch rate [Å/min.]*
Al	*Alu-etch*	*3000*
Au	*Au-etch*	*4000*
SiO_2	*BHF 7:1*	*1000 a)*

Table 2.5: List of chemicals and orders of magnitude of the corresponding etch rates; a)densified or thermally grown SiO_2.

The materials listed in the preceding table are etched isotropically, i.e. at an equal rate in all directions. As a consequence, the resulting etch profile extends under the mask by an amount roughly equal to the etched thickness, giving rise to a characteristic undercut (fig. 2.6). This effect irremediably reduces the resolution performances of such wet etching processes. Since the width of the desired feature can be widened by as much as twice the thickness of the etched film, a good rule of thumb is to keep the thickness of the layer to be pattern below one-third of the resolution to be achieved.
Etch time should be kept at the minimum insuring a complete pattern transfer, since extended etching increases the undercut. This effect is accentuated by the eventual delamination of the photoresist mask. Loss of adhesion produces severe undercuts that are aggravated by capillarity effects. Priming substrate surfaces before photoresist spinning significantly reduces the risks of adhesion failure.

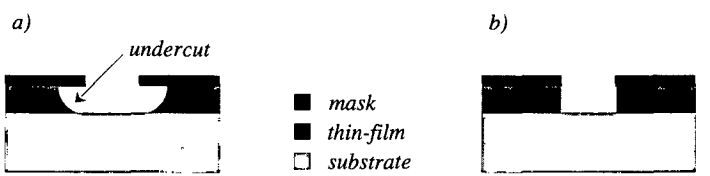

Figure 2.6: Characteristic etch profiles resulting from a) isotropic etch, b) anisotropic etch.

2.4.2 Dry etch

Dry etch includes various techniques such as sputter etching, ion milling, plasma etching (PE) and reactive ions etching (RIE), all of these making use of a glow discharge. The mechanism involved in the etching process can be simplified as either purely physical (sputter etching), chemical (PE), or a combination of the both (RIE). The different etch parameters for C, polyimide and Si_3N_4 are summarized in table 2.6.

Ar sputter etching and cleaning

Sputter etching is carried in a reactor configuration similar to that for sputter deposition, and is used as a preconditioning step for cleaning substrates prior to the C thin-film deposition. Parallels can be drawn from the earlier description of sputtering when considering the etch process as the reverse mode operation of deposition. Knowing that the target becomes eroded when submitted to bombarding particles, exchanging positions between the substrate and the target ideally results in the removal of the thin-film material through the same momentum transfer effect. The glow discharge of an inert gas is again used to impart sufficient energy to the incident particles, so that upon impinging on the substrate surface, atoms of the thin-film are dislodged. Sputter etching is often depicted as the atomic scale version of sandblasting, with the virtues of removing any material. Despite the fact that it can be applied for the removal of noble metals, patterning is however complicated due to the lack of an adequate etch mask, since the erosion rate does not differ markedly from one material to another. Thick photoresist masks, lasting long enough, can be used. However, since sputtering etching is dependent on the incidence of the bombarding particle, top edges of photoresist erode first and consequently lead to the shrinkage of the pattern.

O_2 plasma etch for C and polyimide

In a PE process, the glow discharge generates active species such as atoms or free radicals, that diffuse and chemically react with the surface to produce volatile compounds. Under high pressure conditions, the chemical etching process is controlled by the diffusion of the reactive species, and undercuts similar to those obtained in wet etch may also affect the resolution of the transferred pattern.

PE is a selective technique that only allows the etching of materials for which an adequate reactive gas compound exists. Organic materials are efficiently etched in O_2 plasma. The reaction product is generally composed of CO and CO_2 gases. O_2 plasma is extensively used for removing organic contamination from the substrate, as well as for the stripping of photoresist. Since the process is also adequate for patterning C and polyimide films, the thickness of the photoresist mask must be substantially increased to withstand the etching process. When photoresist masking is inappropriate, Al or Ti masks can alternatively be used. The formation of an inert metallic oxide layer in a strong oxidizing environment will preserve the mask integrity during long etch times. These metallic masks are generated at the expenses of additional process steps, e.g. metallization, lithography and etch.

SF_6 / O_2 reactive ion etching of Si_3N_4

The anisotropy of PE is enhanced by introducing a physical contribution to the etching process. The pressure is usually lowered and the substrate holder is biased to increase ion bombardment. By placing the substrate normal to both the gas flow and the RF field, a highly anisotropic etching can be achieved due to the directional movement of the incident particles. This combined effect of physical and chemical etch is found in RIE. The etch of silicon nitride is carried in a glow discharge containing fluorine. The preference is given here to SF_6, but a number of other fluorinated compounds can also be used [4]. Oxygen is usually added to the gas mixture to promote the formation of elemental fluorine, i.e. increase the etch rate, and prevent the redeposition of organic material.

material	*gas*	*flow rate [sccm]*	*pressure [mbar]*	*power [W]*	*etch rate [Å/min]*
C	*O_2*	*17*	*0.1*	*100*	*≈400*
PI 9103 -25	*O_2*	*17*	*0.1*	*100*	*≈2000*
LPCVDSi_3N_4	*SF_6 / O_2*	*10 / 2*	*0.02*	*90*	*≈550*
PECVDSi_3N_4	*SF_6 / O_2*	*10 / 2*	*0.02*	*90*	*≈650*

Table 2.6: Operating parameters of RF plasma etch processes, for the patterning of C, polyimide (Bectron® PI 9103 -25) and Si_3N_4.

2.4.3 Lift-off

Additive processing encompasses all techniques through which a selective deposition is accomplished. In the case of lift-off, the inverse pattern of the microelectrodes geometry is formed on the wafer level by photolithography, followed by the evaporation of the metal. By dissolving the underlying photoresist mask in acetone, unwanted metallic parts are lifted off, thus leaving on the surface the desired pattern (fig. 2.7). Positive photoresists have been frequently used for lift-off purposes as they were readily soluble in acetone, while the use of traditional negative photoresists was avoided since their removal was difficult even in the adequate stripper solution. Of the recent negative photoresists, some are now soluble in acetone and hence provide a suitable alternative to the positive photoresists.

A high aspect ratio of the photoresist to metal thicknesses is one of the prerequisite conditions for a successful pattern transfer. Vertical separation must be sufficient to prevent the metal deposit to become a continuous film. This condition allows a rapid dissolution of the photoresist mask and prevents the tearing or breaking of the film. In addition to that, photoresist profile is of critical importance (fig. 2.8). Tapered walls, as obtained in undercut photoresist, give rise to the formation of metal wing tips features, that are difficult to entirely cover by the passivation layer. Vertical and

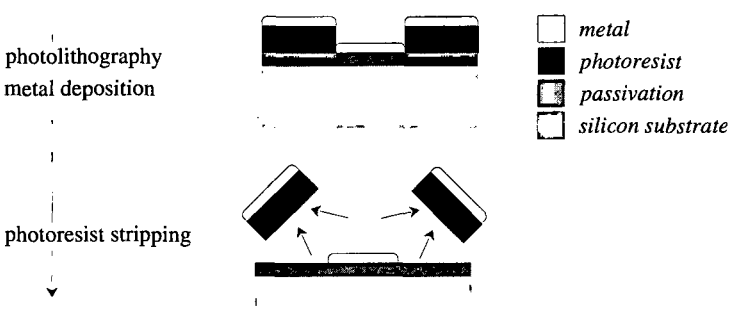

Figure 2.7: Schematic of the lift-off technique.

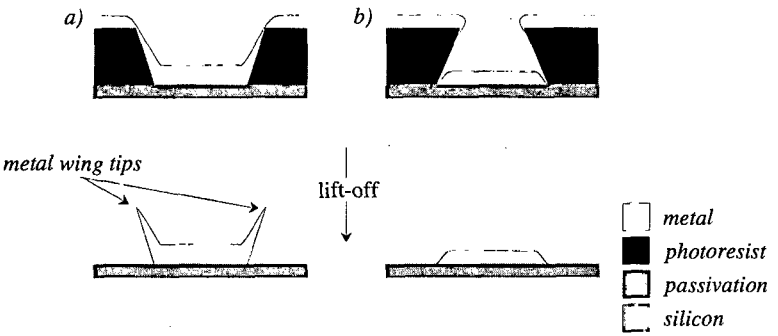

Figure 2.8: a) Formation of metal wing tips at undercut photoresist profile. b) Overcut photoresist profile suitable for the lift-off process.

overcut profiles are more efficient in that respect. Finally, metal evaporation should be done at an angle as perpendicular as possible to the wafer surface, in order to prevent step coverage of the photoresist patterns. Tray rotation, used to improve the homogeneity of the deposit, should be avoided.

Adequate profiles for lift-off purposes can be generated in positive photoresist by treating the surface of the resist. The procedure is performed on exposed photoresist prior development. It consists in removing low molecular weight and photo active compounds in chlorobenzene, in order to form a hardened photoresist surface [15]. Upon development, a pronounced overhang profile results from the chemical modification of the surface. This chlorobenzene treatment is only efficient on overcut or vertical photoresist profiles, the latter being achieved by a contact printing exposure. Tapered walls, as those generated in close proximity photolithography or low exposure energy, cancel the benefits of the overhang and does not prevent the formation of metal wing tips. In principle, the chlorobenzene treatment applies to any novolak-based photoresists, such as the AZ-series (fig. 2.9). However, the results obtained with the AZ 1518 are not as spectacular when compared to those shown in the original literature.
Preliminary tests have been carried with the recent negative photoresist ma-N410. Overcut profiles are obtained by extending the development time by one third. This approach is quite attractive as negative photoresist seems

to easily form an adequate profile for lift-off, without the recourse of surface treatments (fig. 2.10).

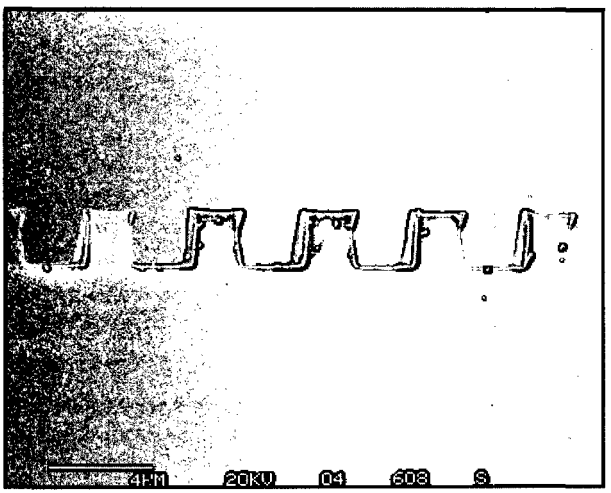

Figure 2.9: SEM picture of the AZ 1518 positive photoresist profile; vacuum contact printing, exposure energy: 55 mJ/cm^2, chlorobenzene soak: 5 minutes, development time: 60 seconds.

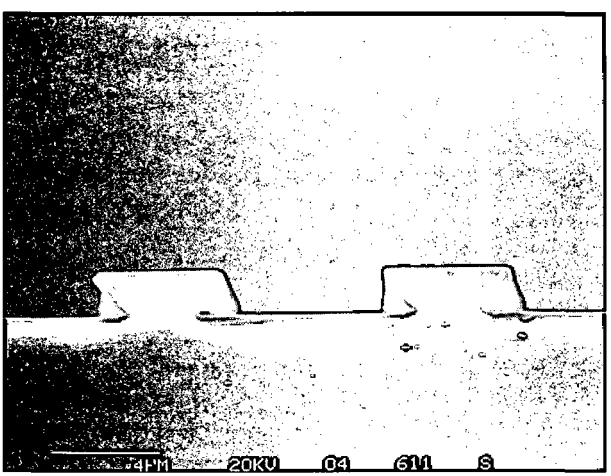

Figure 2.10: SEM picture of the ma-N 410 negative photoresist undercut; vacuum contact printing, exposure energy: 300 mJ/cm^2, development time: 120 seconds.

2.5 Functional Tests

2.5.1 Electrode materials

resistivity

The quality of the electrode material is first assessed in terms of electrical resistivity. Although the proper use would be to express the electrical performances of a conductor by the conductivity, the conductive film is here characterized by its resistivity. Both things being equal, this approach however provides a better insight on the electrode resistance that possibly contributes to the ohmic drop.

Thin-film resistivities up to 10 Ωcm are evaluated by the 4-points probe technique. The experimental set-up consists in four aligned and equally-spaced probes. A constant current I is applied between the two outer probes and the corresponding potential difference V is measured at the two inner ones [4-6]. The potential to current ratio, scaled by the geometric coefficient C_g gives the value of the resistance per square known as the sheet resistivity R_s *[Ω/□]*:

$$R_s = C_g \frac{V}{I} \quad (2.4)$$

C_g takes into account the distribution of the current flux lines within the deposited film. When the substrate diameter is about 20 times larger than the probe spacing (0.635 mm), its limiting value, i.e. $\pi/ln(2)$, is used.

The resistivity ρ *[Ωcm]*, also given the name of bulk resistivity or specific resistance, is found by multiplying the sheet resistivity by the thickness d *[cm]* of the deposited film:

$$\rho = F R_s d \quad (2.5)$$

where F is a correction factor depending on the film thickness to probe spacing ratio. For the thicknesses of interest (< 1 μm), F is very close to unity (0.999) and is omitted. It can be concluded from the values listed in table 2.7, that the measured resistivities for Pt, Ir, Au and C thin-films does not differ markedly from the values reported in the literature for bulk materials. The

material	*thin-film[a] [μΩcm]*	*bulk[b] [μΩcm]*
Pt	*15*	*10.6*
Ir	*7*	*5.3*
Au	*2.9*	*2.3*
C (glassy carbon)	*3200*	*3700-4500*

Table 2.7: Electrical resistivity of metal conductors; a) typical values measured by the 4-points probe technique, film thickness 2000 Å; b) values obtained from [16,17].

resistance generated by the geometry of the electrode is calculated using the sheet resistivity and the electrode surface dimension *L, W [cm]*:

$$R = R_s \frac{L}{W} \quad (2.6)$$

where *L/W* ratio corresponds to the number of squares of width *W* included in a conductive strip of length *L*. By introducing eq. 2.4 into 2.5, the usual formula for a conductor is found. Therefore, *L* corresponds to the length of the conductive path, while *W* and *d* describe the cross section of the conductor.

electrochemical behavior

The electrochemical response of the electrode material is the ultimate criterion to evaluate the quality of the fabrication process, i.e. to determine whether any of the technological steps following the thin-film deposition possibly deteriorate the electrode material. To trace down a faulty step, simple electrochemical tests can be systematically performed on cleaved sections of metallized substrate after each fabrication step.

As the voltammograms of bulk electrode material are well-known, the quality of the thin-films are characterized by cyclic voltammetry. The aspect of the background voltammogram provides information on eventual contamination resulting from the deposition itself or deterioration from the subsequent process steps. Under the appropriate working conditions, the voltammogram allows to visualize, for instance, organic residues adsorbed on the electrode surface or the aforementioned Cr interdiffusion. Pt and Ir are readily evaluated as their voltammograms in H_2SO_4 show characteristic fingerprints. The shape of the voltammogram for Pt, i.e. the position, the

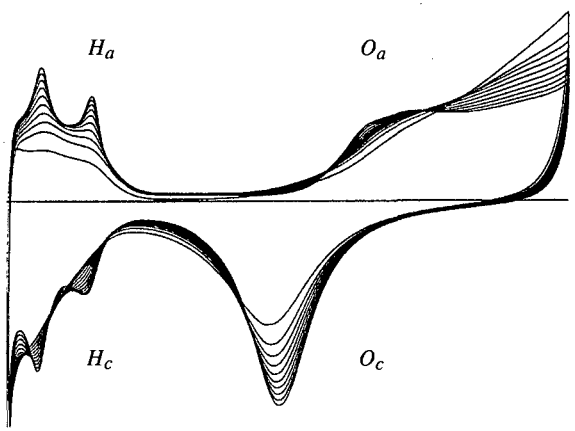

Figure 2.11: Successive voltammograms of Pt thin-film in 1 M H_2SO_4/N_2, 100 mV/s, potentials vs. saturated sulfate reference electrode; H_a, H_C: adsorption and desorption of hydrogen; O_a, O_C: Pt oxide formation and reduction.

presence or the absence of specific peaks, is indicative of the quality of the electrode surface. The number of adsorption/desorption peaks revealed by the measurement is related to the different crystal faces of Pt forming the film [18,19]. Figure 2.11 shows the successive sweeps of a thin-film Pt macroelectrode ($\approx$ 0.3 cm^2) onto which the deposition of a LPCVD Si_3N_4 and its removal in SF_6 plasma etch have been carried out. After less than 10 sweeps, the characteristic features are clearly displayed. However, excellent charge transfer properties are achieved without cycling the electrode potential in H_2SO_4.

Among the different charge transfer reactions that have been intensively and thoroughly investigated, the position of the oxidation and reduction peaks of the ferri/ferro system provides an adequate model system to evaluate the reversibility of the charge transfer reaction, and is considered as relevant diagnostic criterion to evaluate the electrochemical response of various electrode material [17,20]. Dopamine is additionally used as benchmark and is more specific of the assessment of carbon electrochemical activity [17].

2.5.2 Passivation layers

physical integrity

The two following tests are used to provide a gross estimation of the physical integrity of the different dielectric layers, in order to rule out rather poor quality passivation, i.e. when large defects or pinholes are present. The first experimental procedure is based on selective chemical etch and applies to the bottom passivation layers, i.e. LPCVD and PECVD Si_3N_4. The passivation material is deposited on top of a <100> silicon wafer. The thickness of the deposit corresponds to that used later on in the fabrication process (2000 Å). The passivated wafer is immersed in a solution of 19% wt. of KOH in DI water, at 60°C for 12 hours. Unlike silicon, Si_3N_4 should ideally be insignificantly etched in KOH (1-10 Å/hr) and act as a protective etch mask. The presence of pinholes is emphasized by eventual anisotropic etch patterns on the silicon surface. Characteristic and highly contrasted V-grooves can thus be readily observed under optical microscope (fig. 2.12a). The pinhole density of the LPCVD Si_3N_4 is estimated at less than 0.2 pinholes/cm^2. That of PECVD Si_3N_4 is substantially higher and is about 10 pinholes/cm^2. These estimations are made on 3 inch wafer surface, excluding about 0.5 cm from the wafer border where the quality of the deposit is not relevant and the film is possibly damaged by handling.

The second approach is based on the electrolytic decoration principle [21] and is intended for evaluating the top passivation layer integrity, when

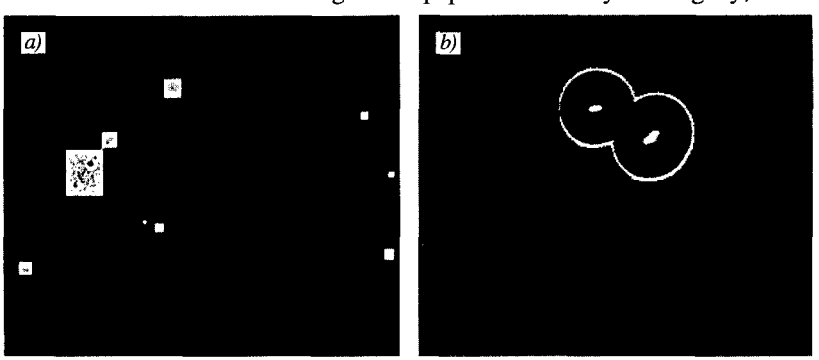

Figure 2.12: Photomicrographs of: a) anisotropic etch of Si wafer through multiple pinholes of a PECVD Si_3N_4 bottom passivation layer; b) Ni electrodeposition through two pinholes of a PECVD Si_3N_4 top passivation layer.

submitted to a potential stress. A multilayer test structure is fabricated on a LPCVD Si_3N_4 passivated Si substrate, by the successive deposition of a Pt layer and the top passivation material under test (LPCVD or PECVD Si_3N_4, Bectron® PI 9103-25). The underlying metallic layer is electrically connected and the wafer is immersed in a commercial Ni electroplating solution. The electrodeposition procedure is followed according to the proprietary recipe. The presence of pinholes is visualized by the growth of Ni hillocks on top of the layer (fig. 2.12b). The values of pinhole density observed for the two distinct nitride layers do not depart significantly from those obtained after the test in KOH. The polyimide layer appears to be practically pinhole-free.
Similar electrodecoration test can be performed after dicing and encapsulation to assess the robustness of the layer. A section of defined area (1 cm^2) is diced and mounted on a PCB. The underlying metallic thin-film is electrically connected by wire bonding and the mounted device is encapsulated. It is then connected to a potentiostat and immersed in the plating solution. It appears that polyimide layer is less brittle then LPCVD or PECVD, and is therefore less sensitive to mechanically induced damages (scratches).

adhesion

Good sealing properties are achieved as long as the passivation material adheres well to the substrate. Apart from the usual tape test, the adhesion of passivation layer is investigated in two accelerated aging tests under humid conditions. The first experimental procedure consists in immersing an unmounted section of the multilayer structure, such as those described earlier for the electrodecoration test, in a boiling solution of 0.9% NaCl at atmospheric pressure for 15 minutes. It has been reported that under such harsh conditions, poorly adhesive polymeric materials peel off within a matter of minutes [22]. The second test is carried out with similar structures in an autoclave, at 1 bar pressure and 120 °C for 5 minutes. All the test structures, passivated with LPCVD, PECVD Si_3N_4 and Bectron® PI 9103-25, have shown no signs of adhesion failure when submitted to both tests. The adhesion performance of these passivation materials is thus considered as excellent.

References

[1] Bunshah R.F., "Handbook of Deposition Technologies for Films and Coatings: science, technology and applications", 2nd ed., Noyes Publications, 1994, USA

[2] Schuegraf K.K., "Handbook of Thin-Film Deposition Processes and Techniques: principles, methods, equipement and applications", Noyes Publications, 1988, USA

[3] Vossen J.L., Kern W., "Thin Film Processes", Academic Press, 1978, New-York

[4] Ghandhi S.K., "VLSI Fabrication Principles: silicon and gallium arsenide", John Wiley & Sons, New-York, 1983

[5] Sze S.M., "VLSI Technology", McGraw-Hill series in electrical engineering, 1983, New-York

[6] Sze S.M., "Semiconductor Devices: Physics and Technology", John Wiley & Sons, 1985, New-York

[7] Moreau W.M., "Semiconductor Lithography: principles, practices and materials", Plenum Press, 1988, New-York

[8] Najafi K., IEEE Engin. in Med. and Biol., June/July 1994 375-387

[9] Kovacs G.T.A., Storment C.W., Halks-Miller M., Belczynski C.R., Della Santina C.C., Lewis E.R., Maluf N.I., IEEE Trans. on Biomed Engin., 41 (1994) 567-577

[10] Edell D.J., Toi V.V:, McNeil V.M., Clark L.D., IEEE Trans. on Biomed Engin., 30 (1992) 633-643

[11] Arquint P.,"Integrated Blood Gas Sensor for pO_2, pCO_2 and pH based on Silicon Technology", PhD dissertation, IMT, University of Neuchâtel, Switzerland, 1994

[12] Cosofret V.V., Erdösy M., Johnson T.A., Buck R.P., Ash R.B., Neuman M.R., Anal. Chem., 67 (1995) 1647-1653

[13] Gernet S.A., "Realization of a Miniaturized Planar Amperometric Glucose Sensor for Biomedical Applications", PhD dissertation, IMT, University of Neuchâtel, Switzerland, 1990

[14] Petrov I., Orlinov V., Ivanov I., Kourtev J., Jelev J., Thin Solid Films, 168 (1989) 239-248

[15] Hatzakis M., Canavello B.J., Shaw J.M., IBM J. Res. Develop., 24 (1989) 452

[16] West R.C., "Handbook of Chemistry and Physics", CRC Press, 68th ed., 1988, Florida, F-122

[17] McCreery L.M., "Carbon Electrodes: structural effects on electron tranfer kinetics" in Electroanalytical Chemistry, a Series of Adances,vol 17, Ed. Bard A.J., Mercel Dekker, 1991, New-York

[18] Bard A.J., Faulkner L.R., "Electrochemical Methods: fundamentals and applications", John Wiley and Sons, New York, 1980

[19] Aschauer E., Fashing R., Urban G., Nicolussi G., Husinsky W., J. Electroanal. Chem., 381 (1995) 143-150

[20] Winkler K., J. Electroanal. Chem., 388 (1995) 151-159

[21] Kern W., RCA review, 24 (1973) 655-690

[22] Yasuda H.K., Sharma A.K., Hale E.B., James W.J., J. Adehsion, 13 (1982) 269-283

Mercury-plated Iridium Microdisk Arrays

As an alternative to iridium wires sealed in glass capillaries, the objective of the present work is to recourse to the thin-film technology to produce ensembles of mercury film microelectrodes, to simplify the manufacture and reduce the preparation time of the microelectrodes.
A short presentation on the characteristic electrochemical behavior of the ensembles of microdisks and the pertinent analytical expressions is first addressed. The fabrication of process of iridium microdisk arrays is then detailed. The electrochemical behavior of the fabricated device and an example of environmental application is presented. Parts of this chapter are taken from a recent publication [1].

3.1 Introduction

Due to the increasingly stringent water quality criteria, the development of sensors for the monitoring of trace metals in natural water, industrial effluents or biological matrices is of major importance [1-7]. To the present date, one of the most sensitive technique for measuring low concentration levels (ppm or sub-ppm) of various trace metals in water is the anodic stripping voltammetry (ASV) [8]. Among the various forms and sizes of mercury electrodes needed for ASV, the thin-film mercury electrodes (MFE) present several attractive advantages over conventional hanging mercury drop electrodes (HMDE). First, limited diffusion within the mercury layer for the adsorbed species results in an enhanced resolution at MFE. Second, thin-film electrodes are easier and safer to use in the field than the large quantity of bulk mercury involved in HMDE. Finally, the electronic instrumentation and the mechanical set-up needed to operate the MFEs is

simpler and can easily be integrated in small portable systems to perform *in-situ* measurements.

The use of iridium as substrate material for the deposition of mercury film has been reported in 1986 by Kounaves et al. [9]. It has been shown that, owing to its low solubility in mercury (< 10^6 wt.%) and good wettability, iridium is a suitable substrate for forming renewable and reproducible mercury films. Aside from the attractive properties of microelectrodes, the rationale motivating the miniaturization of Ir-based MFEs originates from the ability of creating a continuous and durable mercury film on the electrode surface. While a macroelectrode surface is difficult to cover uniformly, a small disk shaped electrode in the micrometer range enables the formation of a mechanically stable and homogenous hemisphere cap of defined radius. Moreover, unlike their macroelectrode counterparts, Hg-plated iridium microelectrodes can be left at open circuit without compromising the uniformity of the film. Using commercially available small diameter iridium wires, the first miniaturization attempt showing good electroanalytical properties has been demonstrated [10,11]. Refining the wire technology by using different electroetching processes, iridium microelectrodes with tip diameters in the range of 1 to 10 μm have been proposed [12-14]. The use of such minute size MFEs is however penalized by a corresponding reduced current intensity. To circumvent this and yet benefit from the properties of these devices, the fabrication of regular arrays of MFEs is proposed. The amperometric response should be multiplied by the number elements, provided that the distance between each element is sufficiently large to avoid shielding effects.

The present research effort is directed towards exploiting the thin-film and photolithographic technology to produce regular array geometries of Ir microelectrodes, with well controlled and defined characteristics. Kounaves et al. [15-17] have recently reported similar investigation efforts. It is anticipated that this approach greatly simplifies the preparation of the microelectrode substrates, increases the reproducibility of the fabrication process and the throughput of single MFEs, and MFEs arrays in particular.

3.2 Theoretical Aspects

In the case of regular arrays, m microelectrodes of identical dimensions are arranged in an orderly fashion (fig. 3.1). If all electrodes are operated simultaneously at a same potential and if the reaction is diffusion-limited, the occurrence of shielding is determined by the geometric parameters of the array, i.e. the electrode radius r and the interelectrode spacing W [18-21]. As previously described in Chapter 1, transition from planar to non-planar diffusion may take place within the time frame of the experiment.

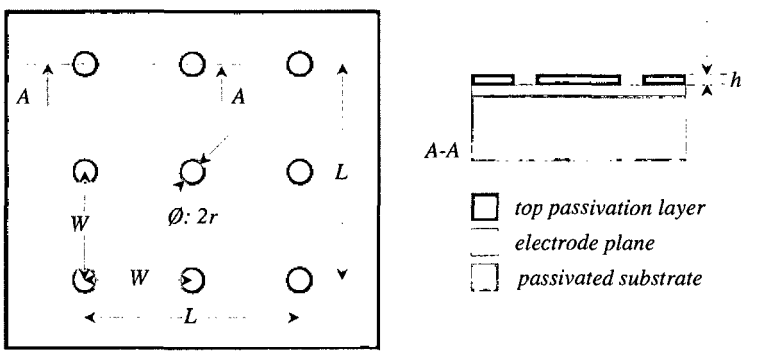

Figure 3.1: Schematic and cross section view of a microdisk array; definition of the geometric parameters r, W, L and h.

3.2.1 Shielding effect

The amperometric response of an array depends on the time scale of the experiment and the interelectrode distance. Three limiting situations can be envisaged.

short experimental time scales

At very short experimental times, when the diffusion layer thickness does not exceed the value of the microdisk radius, planar diffusion is observed at each element of the array. The electrochemical behavior is akin to that observed at a macroelectrode, i.e. characteristic peak-shaped voltammograms and

Cottrellian amperometric responses are observed. Regardless of the packing density, the microelectrodes behave independently and the current response observed at the array is proportional to the overall active area $m\pi r^2$. For example, the diffusion-limited current following a potential step is governed by the Cottrell equation [22]:

$$t << \frac{r^2}{D} \quad I = m\pi r^2 nFDC^* \left(\frac{1}{\sqrt{\pi Dt}} \right) \quad (3.1)$$

where n, F, D, C^* have their conventional meanings.

long experimental time scales, loosely-packed array

When the duration of the experiment is increased, so that the diffusion layer extends past the microdisk geometry but does not yet coalesce with the neighboring diffusion layers, hemispherical diffusion is established at each sensing element. In the case of a loosely-packed array, i.e. when $r<<W$, a steady-state regime is eventually reached. The microelectrodes still behave independently and the amperometric response of the array tends to the limiting expression of a microdisk steady-state current scaled up by the number of elements [23-25]:

$$\frac{r^2}{D} << t << \frac{W^2}{D} \quad I = 4mnFDC^* r \quad (3.2)$$

long experimental time scales, loosely-packed array

In the case of a densely-packed array, a steady-state regime cannot be reached. The individual diffusion layers developing at each microelectrode merge together and form an apparent planar diffusion layer that extends all over the ensemble of microelectrodes. Under this condition, the array behaves as a macroelectrode whose surface area A_{tot} corresponds to the overall geometric area of the device (active and non active area). The corresponding current again follows the Cottrell equation and is described by:

$$\frac{W^2}{D} << t \quad I = \frac{A_{tot} nFDC^*}{\sqrt{\pi Dt}} \quad (3.3)$$

3.2.2 Simulation and analytical expressions

Based on digital simulations, Shoup and Szabo have proposed a semi-empirical expression encompassing the different operation regimes of hexagonal microdisk arrays [26]. The current intensity is expressed as:

$$I = 4mnFDC^{*}rf(\tau,\theta) \quad (3.4)$$

where $f(\tau,\theta)$ is a function involving the diffusion time and the geometric parameters of the array ($\tau = 4Dt/r^2$, $\theta = (1-2r/W)^2$, $B = 0.7823$):

$$f(\tau,\theta) = \frac{\sqrt{\pi}}{2\sqrt{\tau}} + \frac{\pi}{4} + \left(1-\frac{\pi}{4}\right)exp\left(\frac{-B\theta^2(3-2\theta)}{\sqrt{\tau}}\right) - exp\left\{-\left[\frac{\sqrt{\pi}}{2}\left(\frac{\theta}{1-\theta}\right) + B\left(1-\frac{\pi}{4}\right)\theta^2(3-2\theta)\right]\Big/\sqrt{\tau}\right\}\left(1+\frac{3}{2}\frac{\sqrt{\pi}}{\tau}\frac{\theta^3}{1-\theta}\right)^{-1} \quad (3.5)$$

This analytical approximation remains qualitatively valid for quadratic arrays and can be used to assess experimental data obtained with such arrays.

3.2.3 Effects of a recessed geometry

Microdisks fabricated by thin-film technology usually present a recessed geometry as depicted in figure 3.1. The slight recess of the electrode surface, arising from the thickness h of the top passivation layer, possibly hinders the diffusion of electroactive species to the electrode surface. Comparison of the chronoamperometric response at inlaid and recessed microdisk geometry has been addressed by Bond et al [27]. It has been proposed that, in the absence of forced convection and at short experimental times, the diffusion-limited current response of a recessed microdisk, and by extension that of an array of recessed microdisks, is readily given by eq. 3.1. On the other hand, at long experimental times, eq. 3.2 must be modified to take into account the recessed geometry:

$$I = 4mnFDC^{*}r\frac{1}{\frac{4h}{\pi r}+1} \quad (3.6)$$

where h is the step height of the passivation layer (fig. 3.1).

3.3 Fabrication of the Device

3.3.1 Design

Microdisk arrays are fabricated as described in section 2.1, by patterning a LPCVD Si_3N_4 passivation layer deposited on top of a thin-film of Ir (fig. 3.1). All microdisks are therefore interconnected and will operate in parallel. The design of the array consists of 100 interconnected Ir microdisks of 2.5 μm radius, arranged in a quadratic matrix of dimension 10 x 10. In order to minimize shielding effects, the aspect ratio of the interelectrode spacing to the electrode radius must be larger than at least 10 [19]. Electrode spacing of 150 μm has been chosen, resulting in an aspect ratio of 60.

3.3.2 Technological parameters

The devices are fabricated on a 3 inch silicon wafer. The substrate is passivated with a layer of 2000 Å LPCVD Si_3N_4. A Ta layer with a thickness of 200 Å is e-gun evaporated as adhesion promoter prior the deposition of 2000 Å of Ir. The deposition is carried out in one pump-down process. The top passivation layer is formed with 2000 Å of LPCVD Si_3N_4. A standard photolithographic procedure is followed with the AZ 1518 to produce a photoresist mask defining the microelectrode arrays and the connection pads. Unmasked Si_3N_4 surfaces are etched in SF_6/O_2 plasma with the etch parameters given in table 2.6. The photoresist mask is removed in acetone. The wafer is rinsed in isopropanol and blown dry with N_2. When photoresist residues are observed upon visually inspecting the wafer surface, the H_2SO_4/H_2O_2 stripping procedure described in section 2.2.2 is used. The wafer is then rinsed in DI water, dried and saw diced in square chips of 4 mm side, each chip containing a quadratic array of a 10 x 10 microdisks. The circuit is mounted on a printed circuit board, and bonded using Al or Au bonding wires. The mounted device is encapsulated using epoxy resin, to protect the connections from mechanical and chemical damages.

The SEM and AFM images shown in figure 3.2 are representative of the typically clearly defined microdisk surfaces achieved by plasma. Further investigation of the thin-film electrode surface by AFM shows very regular features of about 6 nm in height across the whole microdisk surface.

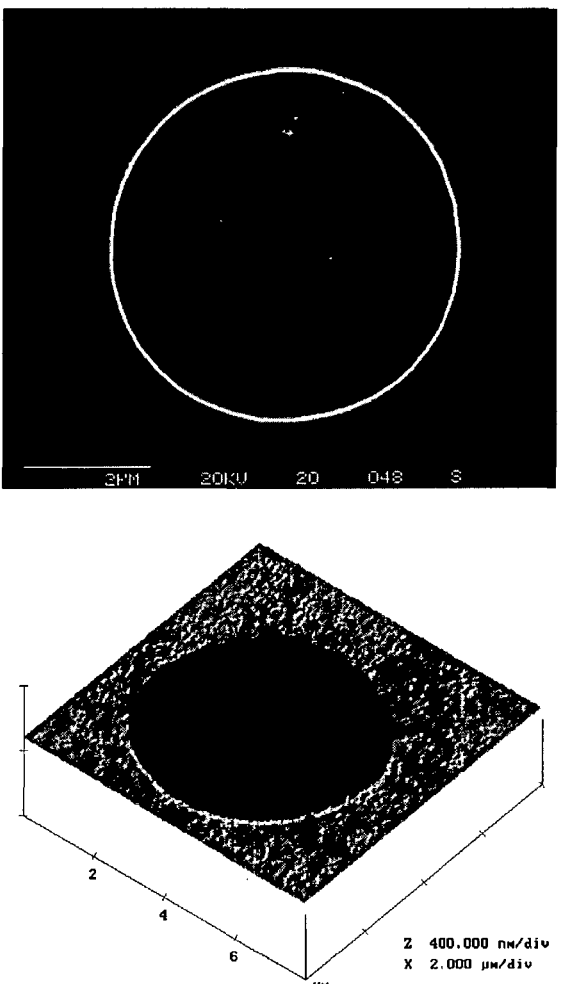

Figure 3.2: SEM (up) and AFM (bottom) pictures of one of the 100 microdisk forming the array; measured electrode diameter: 5.4 µm, estimated surface roughness: ≈ 6 nm.

3.4 Characterization of the Microdisk Array

Prior undertaking the Hg-plating step, the absence of shielding is first investigated by cyclic voltammetry and chronoamperometry, using ferrocyanide (ferro-CN) oxidation as a benchmark. In spite of the fact that the kinetics of ferro/ferricyanide couple may not as simple as often suggested [28, 29], this redox couple remains the most popular to assess the diffusional behavior of microelectrodes.

The Hg-deposition and analytical application have been performed at the "Departement de Chimie Minérale, Analytique et Appliquée" of the University of Geneva, in the group of Prof. J. Buffle. The deposition technique and some of the analytical results are summarized hereafter. A more detailed description of the analytical procedure and results can be found elsewhere [1].

chemicals and apparatus

Preliminary electrochemical characterization is carried out on a panel of Ir microdisk arrays using a three electrode cell of 25 ml (Metrohm), with a Pt wire as counter electrode and a saturated calomel reference electrode (SCE). All potentials are quoted with respect of this reference. Analytical grade ferro-CN ($K_4[Fe(CN)_6]$) is purchased from Merck and solutions of 1 mM are freshly prepared in 1 M KCl. Solutions are degassed with nitrogen prior undertaking any measurement. Conventional cyclic voltammetry and chronoamperometry are performed with an IBM Voltammetric Analyzer (EC/225). The electrode potential is either varied linearly from 0 to 0.6 V, at different sweep rates, or stepped from 0 to 0.6 V. The cyclic voltammograms are recorded on XY-t chart recorder (Kipp and Zonen) and chronoamperometric responses are visualized on a digital oscilloscope (Hewlett Packard). Background current is systematically recorded.

Deposition of Hg and analytical measurements are performed with an AMEL (433A) polarograph. A home made amplifier based on the system developed by Huang et al. [30] set to a gain of 100 is also employed. A three electrode system is used. The reference electrode consists of a Metrohm Ag/AgCl/3M KCl, protected by an additional bridge of 0.1 M $NaNO_3$ to avoid contamination. The counter electrode is a Pt wire. A Plexiglas cell is used to minimize adsorption and desorption effects.

3.4.1 Electrochemical behavior

The electrochemical behavior of the microdisk array is first characterized by cyclic voltammetry. No background features are observed when cycling the microelectrode array in background electrolyte (1 M KCl). S-shaped response characteristic of microdisk electrodes is observed at a low sweep rate (5 mV/s), with a small hysterisis between the forward and reverse sweep (fig. 3.3). Owing to the fact that each element of the array is sufficiently placed apart, overlap of the diffusion layer does not occurs within this experimental time frame. The reproducibility of this characteristic is assessed by running multiple voltammetric experiments on a panel of devices issued from the same fabrication batch (n=10). After background correction, an average diffusion-limited steady-state current of 62.5 nA with a standard deviation of less than 2% is found. This experimental result is in good agreement with the value of 61 nA given by eq.. 3.6, calculated with *m:* 100, *F:* 96484 C/eq, *C:* 10^{-6} mol/cm^3, *D:* 6.3 cm^2/s [28], *r:* 2.7 10^{-4} cm, *h*: 2000 10^{-8} cm). The same reproducibility is observed from batch to batch.

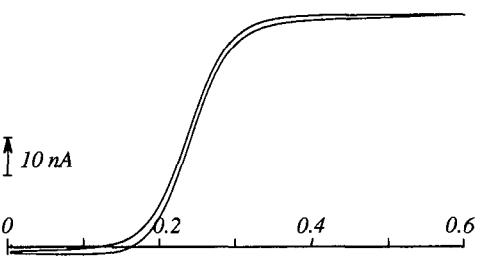

Figure 3.3: Cyclic voltammogram recorded with an Ir microdisk array (radius measured by SEM r: 2.75 μm), in a solution of 1 M KCl containing 1 mM ferro-CN; potential range: 0 to 0.6 V (SCE), sweep rate 5 mV/s.

The absence of shielding is confirmed by chronoamperometry. Figure 3.4 shows the typical result of a chronoamperometric measurement in the long time range (1 - 60 sec), the approximation of Shoup and Szabo (eq. 3.4) and the diffusion-limited current value for a recessed microdisk surface (eq. 3.6).

It can be seen that the experimental results follow the theoretical predictions. As the semi-empirical expression proposed by Shoup and Szabo does not take into account the recessed aspect of the electrode surfaces, the predicted current is larger by ca. 10%. On the other hand, the diffusion limited steady-state current measured with the array tends to the limiting value calculated for a recessed geometry. Further investigation shows that the time needed to reach 95% of the steady-state value is about 6 seconds for the given geometric parameters and experimental conditions. The microdisk radius estimated from the measured chronoamperometric and voltammetric steady-state current (*r*: 2.8 μm) is in very close match to that observed under SEM.

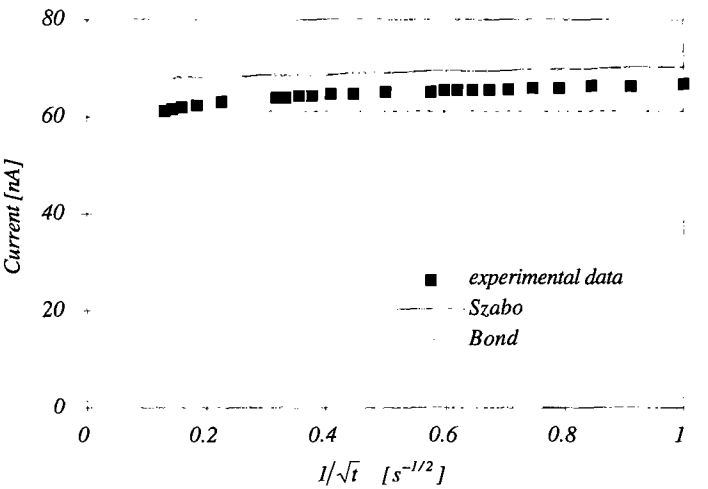

Figure 3.4: Chronoamperometric current vs. square root of time; experimental data, Shoup and Szabo's approximation (eq. 3.4) and diffusion limited steady-state current for a recessed geometry (eq. 3.6).

3.4.2 Hg-film deposition and reoxidation

The mercury film is formed on the surface of the Ir microdisks by reduction of Hg(II) from a solution of 0.1 M $HClO_4$ containing 5 mM $Hg(CH_3COO)_2$ [14]. A deposition time of 10 minutes at -400 mV forms 100 homogeneous droplets of 5-7 μm radius covering each microdisks (fig. 3.5). Mercury is

removed from the electrodes surface by reoxidation of Hg in 1 M KSCN. The electrode potential is varied linearly from -300 mV to 300 mV, at 5 mV/s. Estimation of the mercury layer geometry can be obtained from the charge Q_{red} consumed during the reduction of Hg(II) or from the stripping charge Q_{ox} corresponding to the mercury reoxidation. Assuming that each microelectrode is equally active, the total charge passed during deposition Q_{red} (or reoxidation Q_{ox}) divided by the number of elements in the array m, defines an approximate radius r for each mercury droplet. Based on Faraday's law, the following equation gives for r [cm]:

$$r = \sqrt[3]{\frac{3}{4\pi nF}\frac{M}{\rho}\frac{Q}{m}} \quad (3.8)$$

where M: atomic weight of Hg (200.59 g/mol), ρ: density of Hg (13.55 g/cm^3 at 25°C), Q [C]: Q_{red} or Q_{ox}, and n= 2. The estimated radii are confirmed visually with a Leitz Diavert inverted microscope and a Laborlux normal microscope.

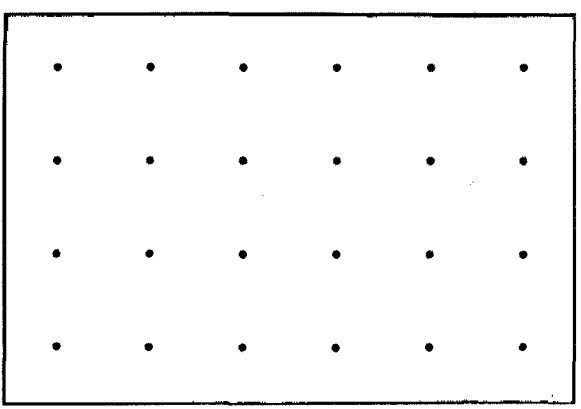

Figure 3.5: Microphotograph of Hg-plated microdisks; hemisphere radius r≈ 6 μm; electrode spacing 150 μm.

The Q_{ox}/Q_{red} ratio is defined as figure of merit assessing the quality and integrity of the Ir surface [14]. Typical values of 0.9 to 1 obtained with the array are indicative of a reproducible Ir surface preparation and a good Hg deposition yield. Same experimental values are obtained regardless to

whether the reoxidation of the Hg film is performed before or after using the device for trace metal measurements. These results attest that i) the Hg hemispheres have a good mechanical stability on the thin-film Ir substrate, i.e. the Hg-plated array can be left at open circuit, dip-rinsed in water and transferred to another cell without altering the Hg film, and ii) the surface integrity of the substrate is not affected by the Hg deposition. A given array is able to sustain at least 10 Hg-film deposition/stripping procedures.

The reproducibility of the Hg film formation is checked by making replicate experiments on a given array and comparing the values of Q_{ox}/Q_{red}. Table 3.1 illustrates the experimental values obtained with a thin-film array and shows for comparison those reported for a sealed-wire microdisks [14]. Comparable values of Q_{ox}/Q_{red} confirm that the thin-film technology is a suitable approach for the fabrication of arrays of Hg-plated microdisks. Very small standard deviations are obtained when considering the estimated radii r_{ox} (1.2%) and r_{red} (1.1%).

thin-film	Q_{red} [μC]	r_{red} [μm]	Q_{ox} [μC]	r_{ox} [μm]	Q_{ox}/Q_{red}
1	*1274*	*6.16*	*1252*	*6.12*	*0.98*
2	*1315*	*6.22*	*1206*	*6.04*	*0.92*
3	*1265*	*6.14*	*1164*	*5.97*	*0.92*
4	*1214*	*6.06*	*1152*	*5.95*	*0.95*
5	*1216*	*6.06*	*1151*	*5.95*	*0.95*
sealed wire	Q_{red} [μC]	r_{red} [μm]	Q_{ox} [μC]	r_{ox} [μm]	Q_{ox}/Q_{red}
1	*24*	*7.60*	*23*	*7.50*	*0.96*
2	*28*	*8.00*	*27*	*7.91*	*0.96*
3	*24*	*7.60*	*21*	*7.27*	*0.88*
4	*23*	*7.50*	*23*	*7.50*	*1.00*
5	*24*	*7.60*	*23*	*7.50*	*0.96*

Table 3.1: Radii of Hg hemispheres calculated from Q_{red} and Q_{ox}, ratio Q_{ox}/Q_{red} for 5 deposition and reoxidation replicates; experimental results obtained with an Ir-based microdisk array and an Ir sealed-wire of 7 μm± 1 radius [14]; deposition time 10 min.; details of the experimental conditions are given in the text.

3.4.3 Trace metal detection

The performance the Hg-plated array is investigated by measuring trace amounts of two metals in a synthetic solution by square wave anodic stripping voltammetry (SWASV) [11,31-34]. The metals of interest are Pb(II) and Cd(II) in deaerated 0.1 M $NaNO_3$ at concentration levels not exceeding 10 nM. After a cleaning phase at -0.1 V for 1 min, metals are preconcentrated in the Hg film at -1.1 V for 5 min. The potential is then increased from -1.1 V to -0.1 V, with a pulse amplitude E_{sw}: 25 mV, a step amplitude ΔE_s: 8 mV and a frequency f: 50 Hz. Owing to the to enhanced diffusion properties associated with microelectrodes, stirring is not used.
The linear calibration curves obtained for both metals in the range of 1 to 10 nM show a very good linear relationship, with slopes of 22 ± 4 nA/nM for Pb(II) (r: 0.996) and 15 ± 2 nA/nM for Cd(II) (r: 0.999). The small variability of these slopes further confirm the reliability of the device. For a preconcentration time of 5 min, detection limits of 0.5 nM and 1 nM for Pb(II) and Cd(II) are respectively achieved. In spite of the fact that these detection limits are similar to those obtained in a single Hg-plated Ir sealed-wire of same radius, the sensitivity is expectedly 100 times higher. This confirms that the elements forming the array behave independently, and that the amplification factor is directly related to the number of sensing elements.

In order to verify that the individual diffusion fields of each Hg-plated microdisks are still independent when long preconcentration times are used, a series of measurement is carried out at different preconcentration times in a 0.1 M $NaNO_3$ solution containing 4.8 nM Pb(II). The eventual occurrence of shielding is detected by a departure from the linear relationship between the peak current intensity and the preconcentration time, as overlapping diffusion fields would cause a hindered mass transfer of metals ions towards the electrode surface, i.e. a decrease of the peak current intensity.
Good linearity is observed for preconcentration times as long as 15 min (r: 0.999), suggesting that shielding effects are not observed in this experimental time frame and for the given geometric parameters of the array (interelectrode spacing: 150 µm, r_{red}: 6.3 µm).

The reliability of a given array for routine measurements has been tested by monitoring the evolution of the concentration signals for several hours, with

the MFE array being left at open circuit between measurements. Systematic trace metal analysis are performed in a solution of 9.65 nM Pb(II) and 8.89 nM Cd(II) without renewing the Hg film. Excellent reproducibility is observed over a 5 hour period. For the repeated 15 measurements, a standard deviation in the order of 4% for both Pb(II) and Cd(II) is found. These results confirm that the Hg film remains stable even when the Ir-based MFE array is left at open circuit, and additionally show that no adsorption of trace metal or release of organic compounds by the epoxy resin used for the encapsulation occurs. Comparable results are obtained with arrays issued from different fabrication batches.

It has been discussed in the case of the sealed-wire, that the quality of the electrical contact between the Ir and the Cu wires has a strong effect on the measurements reproducibility. It has also been established that optimum performances are achieved when the soldering of Ir and Cu is performed by electron bombardment under vacuum [14]. The good results obtained in our case suggest that wire bonding is a simple and suitable technique for achieving reliable electrical connections.

3.4.4 Environmental application

In order to assess the electroanalytical behavior of the Ir-based MFE array, measurement are performed in natural water from the Arve river. This system has already been investigated in terms of total, colloidal and mobile Pb(II) and Cd(II) concentration using a single Hg-plated Ir microdisk [14]. The mobile metal ions are analyzed in water samples at their original pH (8.1-8.2), less than 30 min after sampling. The solution is degassed with a mixture of N_2 and CO_2 to maintain a constant pH. The total concentration is measured in N_2 degassed samples stored at 4 °C during 48 hours after acidification at pH 2. The SWASV parameters are kept unchanged, except that preconcentration time is set to 15 min, and preconcentration potential is changed to -1V for the acidified samples. Internal calibration is carried out on samples filtrated with a 0.2 µm pore size membrane by successive addition of 0.965 nM Pb(II) and 0.889 nM Cd(II) (fig. 3.6). Comparison of metal titration on the river Arve water and on synthetic water have shown

that added metal ions negligibly adsorb on particles of size < 0.2 μm in the time frame of the calibration (2-3 hr.).

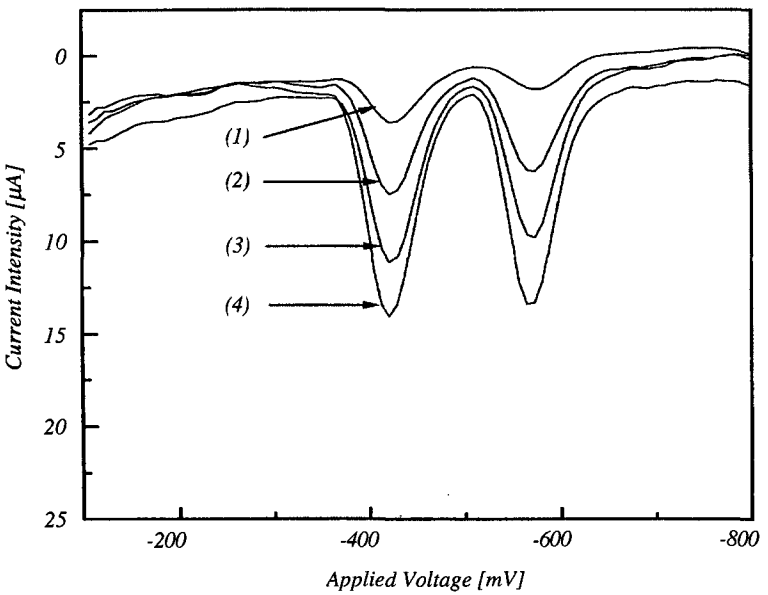

Figure 3.6: SWASV of non acidified Arve river sample; (1) raw sample, (2-4) 0.2 μm filtrates with successive additions of 0.965 nM Pb(II) and 0.889 nM Cd(II). Preconcentration parameters: -1.1 V for 15 min; SWASV parameters: E_{sw}: 25 mV, ΔE_s: 8 mV and a frequency f: 50 Hz.

The mobile and the total concentrations of Pb(II) measured with the Ir-based MFE array are respectively 0.4 ± 0.1 nM and 13 ± 1 nM. These experiment results are in a very good agreement to those obtained with a single Ir-microdisk MFE (0.2 ± 0.1 nM and 13 ± 1 nM), particularly when considering that the measured mobile concentration is close to the detection limit of 50 pM. Note that due to the large amount of suspended particles (70 mg/l) the percentage of free metal ions with respect of the total metal ions is low (1-3%). These results have been successfully cross-checked by Supported Liquid Membrane selective preconcentration followed by atomic adsorption and direct atomic adsorption [1].

3.5 Conclusion

Mercury-plated iridium microelectrode arrays have been proposed for trace metal analysis in environmental measurements. The devices consist in 100 interconnected microdisks of 2.5 μm radius, arranged in a quadratic matrix of dimension 10 x 10. The control of the geometric parameters of the array is accomplished by photolithography. Microdisk surfaces with sharp and clean edges are achieved by plasma etch. The electrochemical behavior of the array is in good agreement with the theoretical predictions. As shielding is not observed for the considered experimental time scale, the amperometric response is amplified by the number of microelectrodes. The sensitivity of the device is therefore increased by a factor of 100, when compared to that of a single microdisk.

Successful Hg-plating, trace metal measurements and film removal can be repeated up to 10 times before the performances of the device start to degrade. The response of the mercury-plated array shows a very good linear relationship with the concentration of Cd(II) and Pb(II) up to 50 nM, with a minimum detectable amount of 50 pM. Good reproducibility (4%) of the long term measurements (5 hr) emphasizes the viability of the fabrication process. Experimental results obtained in natural water are comparable to those obtained with the sealed-wire microdisk and by other measuring techniques.

The good fabrication yield and the large throughput of devices with reproducible characteristics confirm that the proposed technological sequence is a suitable choice for the batch production of mercury film electrode arrays. In addition to the fact that the manufacture of regular arrays by the sealed microwire approach is not straightforward, considerable simplification and control of the electrode preparation steps is achieved by using the thin-film technology.

References

[1] Belmont C., Tercier M.L., Buffle J., Fiaccabrino G.C., Koudelka-Hep M., Anal. Chim. Acta, 329 (1996) 203-214

[2] Tercier M.L., Buffle J., Electroanalysis, 5 (1993) 187-200

[3] Golaz J., Osteryoung J., Anal. Chim. Acta, 181 (1986) 211-218

[4] Adeloju S.B.O., Pablo F., Anal. Chim. Acta, 288 (1994) 157-166

[5] Wang J., Rongrong X., Baomin T., Wang J., Renschler C.L., White C.A., Anal. Chim. Acta., 293 (1994) 43-48

[6] Adeloju S.B.O., Pablo F., Electroanalysis, 7 (1995) 750-755

[7] Uhlig A., Paeschke M., Schnakenberg U., Hintsche R., Diederich H.J., Scholz F., Sensors and Actuators, B 24-25 (1995) 899-903

[8] Wang J., "Stripping Analysis: principles, instrumentation and application", VCH, New York, 1985

[9] S.P. Kounaves, J. Buffle, J. Electrochem. Soc., 113 (1986), p. 2495-2498

[10] Golas J., Galus Z., Osteryoung J., Anal. Chem., 59 (1987) 389-392

[11] Wetcher C., Osteryoung J., Anal. Chem., 61 (1989) 2092-2097

[12] Kounaves S.P., Deng W., J. Electroanal. Chem., 301 (1991) 77-85

[13] Kounaves S.P., Deng W., Anal. Chem., 65 (1993) 375-379

[14] Tercier M.-L., Parthasarathy N., Buffle J., Electroanalysis, 7 (1995) 55-63

[15] Kounaves S.P., Deng W., Hallock P.R., Kovacs G.T.A., Storment C.W., Anal. Chem., 66 (1994) 418-423

[16] Kovacs G.T.A., Storment C.W., Kounaves S.P., Sensors and Actuators, B23 (1995) 41-47

[17] Kounaves S.P., Kovacs G.T.A., Storment C.W., US patent 5378343

[18] Reller H., Kirowa-Eisner E., Gileadi E., J. ELectroanal. Chem., 161 (1984) 247-268

[19] West A.C., J. Electrochem. Soc., 140 (1993) 134-139

[20] Amatore C., in "Physical Electrochemistry: principles, methods and applications", ed. Rubinstein I., Marcel Dekker, New York, 1995, 156-163

[21] Scharifker B.R., J. Electroanal. Chem., 240 (1988) 61-76

[22] Bard A.J., Faulkner L.R., "Electrochemical Methods: fundamentals and applications", John Wiley & Sons, New York, 1980

[23] Saito Y., Rev. Pol. Japan, 15 (1968), 177-187

[24] Oldham K.B., J. Electroanal. Chem., 122 (1981) 1-17

[25] Shoup D., Szabo A., J. Electroanal. Chem., 140 (1982) 237-245

[26] Shoup D., Szabo A., J. Electroanal. Chem., 160 (1984) 19-26

[27] Bond A.M., Luscombe D., Oldham K.B., Zoski C.G., J. ELectroanal. Chem., 249 (1988) 1-14

[28] Beriet C., Pletcher D., J. Electroanal. Chem., 361 (1993) 93-101

[29] Winkler K., J. Electroanal. Chem., 388 (1995) 151-159

[30] Hung H.J., He P., Faulkner L.R., Anal. Chem., 58 (1986) 2889

[31] Osteryoung J.G., Osteryoung R.A., Anal. Chem., 57 (1985) 101A-110A

[32] Whelan D.P., O'Dea J.J., Osteryoung J., J. Electroanal. Chem., 202 (1986) 23-36

[33] Kounaves S.P., O'Dea J.J., Chadresekhar P., Osteryoung J., Anal. Chem., 386-389

[34] Wikiel K., Osteryoung J., Anal. Chem., 61 (1981) 2086-2092

Interdigitated Microelectrode Arrays

Carbon electrodes are commonly applied in electroanalysis and have proven to be of adequate use in systems involving biologically important molecules. The objective of the present work consists in combining the benefits offered by interdigitated microelectrode arrays (IDAs) with the advantages related to the electrochemistry of C.
A short introduction on the specific properties of IDAs is given. The fabrication process of Pt and C-IDAs is then detailed. The electrochemical results obtained with the fabricated devices are discussed. Two applications of C-IDAs are presented. Parts of this chapter are taken from a recent publication [1].

4.1 Introduction

Among the various geometries of microelectrode arrays, the IDA appears to be of great interest for many analytical applications where particularly low detection limits are needed. Its improved signal-to-noise ratio makes it ideally suited for a use as electrochemical detector in liquid capillary chromatography and electrophoresis [2-6]. In addition to the achievement of a steady-state regime, the redox cycling effect arising from the proximity of the interdigitated electrodes leads to enhanced detection sensitivity for reversible or quasi reversible charge transfer reactions. Approximations and simulations of these particular characteristics have been addressed under various experimental conditions, for the double-, triple-band electrodes and interdigitated configuration [7-19].
The early contributions of Sanderson and Anderson published in the mid '80s are generally cited as pioneering work on interdigitated arrays of thin-film microelectrodes [16-19]. More recently, the marked interest on the particular

electroanalytical properties of IDAs has been embodied by a substantial and innovative work carried out by Niwa, Morita and Tabei, at the NTT Basic Research Laboratories. The advantageous aspects of electroanalysis related to the use of IDAs and other pertinent references on the topic can be found in the recent review of Niwa [20]. Among the various analytical applications, detection of dopamine and other neurotransmitters [2-6, 21-25], mediators and proteins [4, 26-33], pharmaceutical compounds [1] and trace metal amounts [34-36] have been reported. The interdigitated geometry has also been intensively used as molecule-based electronic devices [37-41], for the characterization of redox polymers [42-44], and in electrosynthesis [45, 46].

A wide potential window towards negative potentials, convenience for surface chemical modifications and enhanced electron transfer reaction of many biologically important molecules are especially interesting features outlining the use of carbon electrodes [47-53]. Researchers have taken advantage of semiconductor processing techniques to pattern thin-film electrodes made from noble metals, and thus obtain complex structures in the micrometer range. Carbon, however, has proved more difficult to adapt to the thin-film technology. Several technical aspects, such as controlled bulk resistivity and electrochemical properties, good adhesion, reliable deposition and patterning processes, are to be solved to ensure reproducible electrodes. The deposition by pyrolysis is the most frequent technique that is used technique for producing carbon thin-films presenting good electrochemical characteristics [54-56]. Based on this approach, recent contributions describe the fabrication of interdigitated carbon electrodes at a pyrolysis temperature of 1000 °C, with a bulk resistivity in the order of 10^{-3} Ωcm [6, 23-26]. The magnetron sputtering technique is chosen in this work as an alternative to the high temperature pyrolytic approach, allowing depositions to be performed at substrates temperature not exceeding 120 °C [57, 58]. The influence of the sputtering parameters on the film characteristics has been qualitatively determined through a systematic approach to set up a reproducible process. To date and to the author knowledge, no reports have yet been made on such sputtered-C microelectrodes, exhibiting a low sheet resistance ($\approx 10^{-3}$ Ωcm), a good adhesion and electrochemical behavior.

4.2 Theoretical Aspects

IDA is composed of two sets of microband arrays, forming two comb-like electrodes facing each other (fig. 4.1). Apart from the benefits related to i) the microband geometry and ii) the arrangement in array, the particular electrochemical behavior of IDA arises from the close spacing of the interdigitated electrodes. These effects, known as redox cycling and shielding are addressed in the following section. The microbands are assumed to all have equal width W_e and length b.

4.2.1 Redox cycling

The electrochemical amplification results from the feedback effect described in Chapter 1, when the diffusion fronts of two closely spaced anode and cathode overlap. For a reversible or a quasi-reversible reaction, the proximity of these two electrodes causes reactants to be generated primarily at the closely spaced electrodes rather than being transported from the bulk. As the product generated at one electrode (generator) diffuses across a narrow interelectrode spacing (gap) and reaches the second electrode (collector), it is

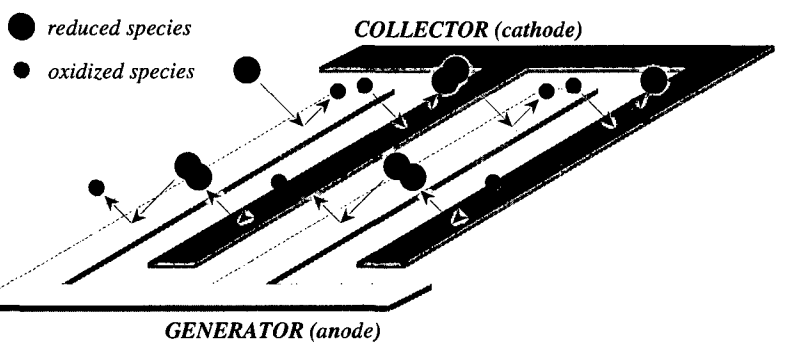

Figure 4.1: Schematic of a redox cycling at interdigitated electrodes. The oxidized species generated at the anode diffuses towards the cathode, where it is reduced. This converted species diffuses back to the anode where it is again oxidized.

eventually converted there to its initial state by a reverse reaction (fig. 4.1). This regenerated species diffuses back to the generator and provides an additional amount of reactants. The multiple oxidation and reduction process (redox cycling) results in a mutual feedback of reactants that prevents the depletion of species in the vicinity of the electrodes. Therefore the evolution of the diffusion fronts towards the bulk solution is limited, and quasi-steady-state concentration gradients of oxidized and reduced species are established within the gap. The smaller is the gap, the steeper the concentration gradient and the higher the current. A corresponding amplification of the generator and the collector currents is observed.

In a generation-collection experiment, the generator is either cycled within a defined potential range or held at a fixed potential to initiate the redox reaction, while the collector is set at a constant potential value for which the opposite reaction occurs. Hence, after the initial double layer charging, the collector current is no longer affected by a capacitive contribution and is solely related to the diffusion process of the species across the gap. This operation is referred to as *dual mode* and requires the use of a bipotentiostat. The combination of the electrochemical amplification, the steady-state regime together with the absence of charging current at the collector contributes to the significant lowering of the achievable detection limit.

The collection efficiency ϕ_{ss}, as defined by Bard A.J. et al. [7], is given by the ratio of the magnitudes of the diffusion-limited currents at the collector I_c and the generator I_g :

$$\phi_{ss} = \frac{|I_c|}{|I_g|} \quad (4.1)$$

When diffusion is the dominant mass transport mode and in the absence of coupled reactions, ϕ_{ss} is only dependent of the geometric parameters of the IDA, i.e. electrodes width and gap. Large electrode spacing lead to small values of the collection efficiency, as a significant amount of generated species diffuses to the bulk solution. Conversely, ϕ_{ss} tending to unity implies that a very limited amount of species escapes into the bulk. The steady-state regime would only be achieved if $\phi_{ss}=1$.
The effect of coupled chemical reaction, e.g. catalytic or homogeneous reactions, on ϕ_{ss} are discussed hereafter.

Niwa O. et al. [4] have shown that the average diffusion length W_d $[\mu m]$ between the generator and the collector can be described by:

$$W_d = \frac{W_e}{4} + W_g \quad (4.2)$$

where W_e is the width of the interdigitated electrodes, and W_g the gap. The same authors have suggested that the collection efficiency is correlated to W_d, i.e. the smaller the value of W_d the higher is ϕ_{ss}.

The amplification rate A_r is defined as:

$$A_r = \frac{I_g}{I_{g,o}} \quad (4.3)$$

where $I_{g,o}$ is the magnitude of the quasi-steady-state generator current in a single mode operation (collector at open circuit) and I_g that observed in a dual mode operation. It is also assumed that A_r corresponds to the average number of redox cycles N_{rc}, and that both are dependent on W_d.
The average number of redox cycles can also be calculated from:

$$N_{rc} = \frac{1}{1-\phi_1\phi_2} \quad (4.4)$$

where ϕ_1 and ϕ_2 are the collection efficiencies in a normal generator/collector operation, and that when the role of the generator and collector are exchanged. For a symmetric geometry, i.e. when the widths and lengths of the fingers forming the generator and the collector are equal, similar values of ϕ_1 and ϕ_2 should be obtained.

Alternatively, the feedback factor F_b introduced by Bard et al. [7] may also be used to characterize the electrochemical feedback:

$$F_b = 1 - \frac{1}{A_r} \quad (4.5)$$

An approximation of the limiting quasi steady-state currents at both the generator and collector is proposed by Aoki et al. [10], by analytically solving the two dimensional Laplace equation. The following approximation has less than a 2% error for $W_g/W < 0.85$, and predicts that the ratio I_{lim}/m

does not vary with the absolute values of W_g and W as long as the ratio W/W_g is retained:

$$I_{lim} = mbnFC^*D\left[0.632\ln\left(2.55\frac{W}{W_g}\right) - 0.19\left(\frac{W_g}{W}\right)^2\right] \quad (4.6)$$

where m is the number of generator/collector pairs, b *[cm]* is the length of the electrodes, n and F have their usual meaning, C^* *[mol/l]* is the sum of the bulk concentration of the oxidized and reduced species, D *[cm²/s]* is taken as a common diffusion coefficient for both species and $W = W_e + W_g$ *[cm]* when the widths of the generator and collector electrodes are equal.

The time needed to reach a limiting quasi-steady-state current is approximated by the time t_{gap} required by the species to diffuse across the gap:

$$t_{gap} \approx \frac{W_g^2}{2D} \quad (4.7)$$

where D is a common diffusion coefficient for both species. Equating this approximation with the characteristic time of cyclic voltammetric experiments, i.e. $t = RT/nFv$, yields a condition on the sweep rate v:

$$v < \frac{RT}{nF}\frac{2D}{W_g^2} \quad (4.8)$$

This condition on the experimental time scale also sets an order of magnitude of the time constant of the coupled reactions that can be detected at the collector [9]. If the rate of the following reaction is sufficiently fast, the generated species are consumed in the chemical or catalytic reaction before being able to reach the collector. The half life of the coupled reaction, $t_{rxn} = (k_{EC})^{-1}$ where k_{EC} is the corresponding rate constant, can be compared to time needed for the generated products to diffuse across the gap t_{gap}. Therefore, if $t_{rxn} >> t_{gap}$, the chemical step is not detected. The rate of the coupled reaction is too slow to prevent the generated product from reaching the collector. Conversely, if $t_{rxn} << t_{gap}$, a fraction of generated product participates in the coupled reaction, thus reducing the amount of collected species. The decrease of ϕ_{ss} is function of the diffusion coefficient, the gap and the rate constant of the coupled reaction.

4.2.2 Shielding effect

Shielding and feedback are two mutually exclusive effects depending on the operation mode of the electrodes. In a *single mode* operation, one side of the IDA is potentiostated while the other is left unconnected, i.e. at open circuit. As each element of the array is operated at a common potential, no feedback is observed. Yet, due to the proximity of the electrode, a shielding phenomenon appears when each element of the array is within the diffusion layer of its neighbor [7, 15]. Unlike the case of the microdisk arrays discussed in chapter 3, the interelectrode spacing may not sufficient for a transition from planar to non-planar diffusion to occur.

At a very short experimental time, when the diffusion layer thickness does not exceed the value of the microband width, planar diffusion occurs at each individual microband. The electrochemical behavior resembles to that observed at a macroelectrode. Peak-shaped voltammograms and time decaying chronoamperometric responses are observed. The microelectrodes behave independently and the current magnitude observed at the array is proportional to the sum of the microbands area.

By increasing the experimental time, each individual diffusion layer extend past the microband geometry. Yet, due to the proximity of the interdigitated electrodes, the hemicylindrical diffusion layers developing at adjacent microbands interpenetrate before a steady-state diffusion regime can be established. The electrochemical behavior of the IDA remains that of a planar macroelectrode, whose effective electrode surface is now equivalent to the entire geometric area occupied by the comb-like electrodes, i.e. including non active surfaces inscribed in the geometry (gaps and unconnected electrode). Note that this macroelectrode behavior is accentuated even more if both sides of IDA are shorted together.

If the experimental time is further increased, the diffusion layer extends past the entire geometric area and a non planar diffusion field may possibly be established . As discussed in chapter 1, this transition may not occur if the thickness of the diffusion layer becomes comparable to that of the convection layer.

4.3 Fabrication of the Devices

The IDAs are fabricated according to the technological sequence described in Chapter 2.

4.3.1 Design

Three different designs are generated by varying W_e and W_g in order to evaluate the incidence of these geometric parameters on the performances of the IDA (table 4.1). In each design, the microbands are 1 mm long and the generator/collector pairs are replicated m times over a total area of 1 mm^2. The size of the chip is 2.5 x 10 mm^2 and accommodates two different designs (A and B, B and C)
To precisely calculate ϕ_{ss} and N_{rc}, a top passivation layer must be patterned to only expose the interdigitated electrodes. Pt-devices are passivated with an LPCVD Si_3N_4 for that purpose. It is worth noting that the absence of a top passivation layer does not compromise the use of unpassivated C-devices. As the redox cycling is a phenomenon related to the close spacing of the anode/cathode arrangement, the species generated at the interconnection line of the generator most likely diffuse into the bulk solution and do not participate to the feedback process. It can be assumed that, provided that no interfering reaction occurs at the collection potential, the collector current is solely determined by the redox cycling taking place at the closely spaced microbands. It is also expected that for long experimental times the generator current finally resumes to the steady-state value caused by redox cycling. Unpassivated IDAs retain their attractive properties and can therefore be used in most applications.

design	*W_e [µm]:*	*W_g [µm]:*	*m:*
A	*2*	*2*	*125*
B	*5*	*5*	*50*
C	*10*	*10*	*25*

Table 4.1: Geometric parameters of the array and corresponding number of interdigitated pairs of microbands.

4.3.2 Technological parameters

Pt-IDAs

The devices are fabricated on a 3 inch silicon wafer passivated by 2000 Å of LPCVD Si_3N_4. Before undertaking the photolithographic procedure, the wafer is dehydrated for 30 min at 200 °C and primed in a vapor phase of HMDS for 15 min. The photoresist AZ 1518 is then spin coated on the wafer with a sequence of 3 s at 1000 rpm and 40 s at 4000 rpm. The coated wafer is prebaked for 30 min at 80°C. The substrate is exposed to a U.V. light source at an energy of 55 mJ/cm^2, on a vacuum contact mode. The wafer is immersed in chlorobenzene for 5 min and blown dry with N_2. The development is performed in a solution of AZ 351/DI water (1:4) for 60 s. The photoresist is cured for 20 min at 120 °C.
A Ta adhesion layer of 200 Å thickness is deposited by e-gun evaporation, followed by the deposition of Pt at a thickness of 1500 Å. The interdigitated structures are revealed by lift-off, upon dissolving the underlying photoresist in acetone. The wafer is rinsed in isopropanol, blown dry with N_2. Note that gold IDAs are similarly obtained by replacing Pt with Au.
A layer of 2000 Å thick LPCVD Si_3N_4 is deposited on the Pt devices only. Openings in the passivation layer are defined by photolithography above the interdigitated structures and the bonding pads. A standard photolithographic procedure is applied using the AZ 1518, i.e. as described earlier with the exception of the chlorobenzene pretreatment. The Si_3N_4 is etched in an SF_6/O_2 using the operation parameters given in table 2.6. The etch time is adjusted to remove 2000 Å of passivation with an extra 5% over etch to insure that Pt features are properly exposed. The photoresist is stripped using H_2SO_4 as described in § 2.2.2.
The wafer is saw-diced into individual devices of 2.5 mm by 10 mm. Each chip is mounted on a PCB and is electrically connected by wire bonding. These interconnections and the PCB are carefully encapsulated with an epoxy resin.

The lift-off introduces a bias of $\approx$ +0.25 µm affecting the line width. Consequently, the effective electrode width is increased by twice the amount of the bias while the gap is reduced by as much, e.g. 2 µm electrode width and 2 µm gap respectively results in a 2.5 µ and 1.5 µm (fig. 4.2).

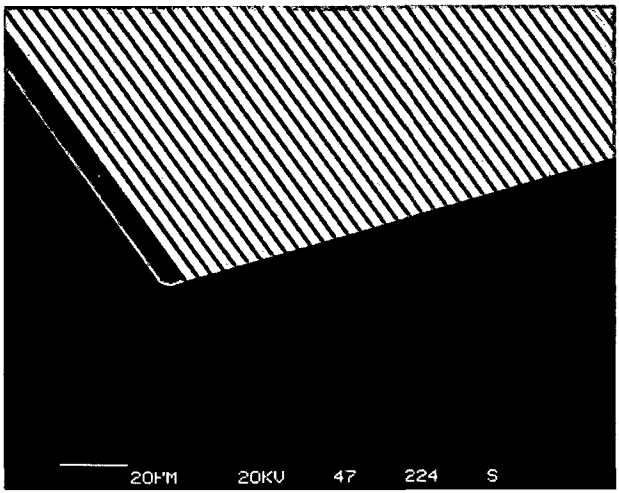

Figure 4.2: SEM photograph of Pt-IDA of type A (side view); electrode width: 2.5 µm, gap: 1.5 µm, active area 1 x 1 mm² defined by a patterned Si_3N_4 top passivation.

C-IDAs

The fabrication of the IDAs starts with the sputtering of 4000 Å thick C layer on top of the Si_3N_4 passivated wafer. The patterning of the layer is performed in O_2 plasma with the operation parameters listed in table 2.6. Depending of the choice of the masking material (photoresist or metal), one of the two following procedures is used.

a) The photoresist mask is generated using the AZ 1518. After dehydration and HMDS priming steps, the photoresist is spin coated on the wafer with a sequence of 3 s at 1000 rpm and 40 s at 4000 rpm. The coated wafer is prebaked for 30 min at 80°C. The substrate is exposed to a U.V. light source at an energy of 55 mJ/cm², in a vacuum contact mode. The development is performed in a solution of AZ 351/DI water (1:4) for 60 s. The photoresist is cured for 30 min at 120 °C.

As photoresist and C are respectively etched at a rate of 2000 Å/min and 440 Å/min, a photoresist mask with a thickness of 1.8 µm is sufficient to withstand the full patterning of the C layer and yet be completely removed upon terminating the process. No photoresist stripping in acetone is necessary as etch time is usually increased by 5% to insure a complete pattern transfer and photoresist removal. Note that the thickness of the

photoresist can be tailored by varying the rotation speed of the spinner or by using more or less viscous photoresists. Thicker masks offer better protection by lasting longer, however at the expenses of a poorer resolution.

b) The metallic mask is obtained by the deposition of Ti layer (500 Å) on top of the wafer. A standard photolithographic procedure is carried out with the AZ 1518. Unprotected parts of Ti are removed in BHF (7:1), leaving on the wafer the image of the microelectrodes. After a careful rinse in DI water and drying with N_2, the photoresist is removed in acetone. The wafer is rinsed in isopropanol and blown dry with N_2. After the completion of the C patterning in O_2 plasma, the metallic mask is removed in BHF (7:1). The wafer is rinsed in DI water and blown dry with N_2.

The wafer is saw-diced into individual devices of 2.5 mm by 10 mm. Each chip is mounted on a printed circuit board (PCB) and is electrically using a conductive silver epoxy resin. These interconnections and the PCB are carefully encapsulated with an epoxy resin.

C devices are affected by a bias of ≈ -0.25 μm due to the undercuts produced by the plasma etch process. The electrode width in this case is diminished by twice the amount of bias, whereas the gap is increased by as much (fig. 4.3).

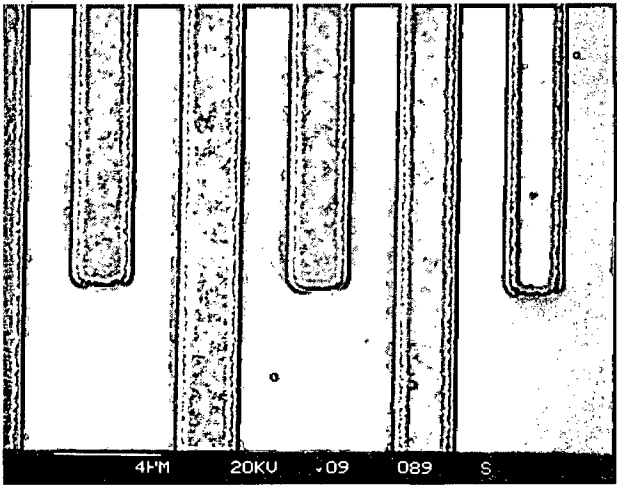

Figure 4.3: SEM photograph of C-IDA of type A (top view); electrode width 1.9 μm, gap: 2.2 μm. Eroded top edges are caused by undercutting during O_2 plasma etch.

4.4 Characterization of the Pt-IDAs

Unlike C or Au-IDAs, Pt-IDAs have a top passivation layer that defines an active area and prevents non-interdigitated features (leads and side of the combs) from participating to electrochemical reaction. Therefore, these devices are the most adequate for evaluating the dependence of ϕ_{ss} and N_{rc} with the different geometric parameters. Ferrocyanide (ferro-CN) is used as redox model to investigate the electrochemical behavior of the IDAs.

chemicals , apparatus and procedure

Electrochemical experiments are performed using a three electrode cell of 25 ml (Metrohm), with a Pt wire as counter electrode and a saturated calomel reference electrode (SCE). All potentials are quoted with respect of this reference. Analytical grade sulfuric acid is diluted to 1 M concentration in deionized water. Ferro-CN ($K_4[Fe(CN)_6]$) is purchased from Merck and solutions of 1 mM are freshly prepared in 1 M KCl. Conventional cyclic voltammetric measurements are performed with an IBM Voltammetric Analyzer (EC/225). An in-house built bipotentiostat is used for the generation-collection experiments (Appendix A). New electrodes are used for each set of experiments and background currents are monitored systematically. All solutions are degassed with N_2 prior any measurement for 15 minutes.

4.4.1 Electrochemical behavior of Pt-IDAs

Pt electrode material

Preliminary electrochemical characterization of Pt-IDAs has been carried out in H_2SO_4 to evaluate the quality of the bulk material. The electrodes are cycled ten times between -0.655 and +0.900 vs. a saturated sulfate reference electrode, at 100 mV/s. Characteristic hydrogen adsorption/desorption peaks similar to those depicted in chapter 2 (fig. 2.11) are observed, suggesting that the electrode surface is electrochemically clean and that the high temperature LPCVD deposition process has not affected the electrochemical properties of the Pt thin-film.

single mode operation

The electrochemical response of Pt-IDAs is assessed by cyclic voltammetry of 1 mM ferro-CN in 1M KCl, with a device of type A operated in a single mode operation, i) when one side of the IDA is potentiostated and the other is left at open circuit, and ii) when both sides of the IDA are shorted together and potentiostated (fig. 4.4). The potential is varied linearly at 50 mV/s from -0.2 to 0.6 V.

A peak-shaped response attributed to the overlap of the diffusion fronts at each microband is observed. This shielding effect is confirmed upon operating both sides of the IDA (ii), as the current magnitude observed in this case does not corresponds to twice the value of (i).
The degree of reversibility of the electrochemical reaction is evaluated by measuring the peak separation ΔE_p. Experimental values measured in the case (i) and (ii) are respectively ΔE_p: 75 mV and 65 mV. In spite of the fact that

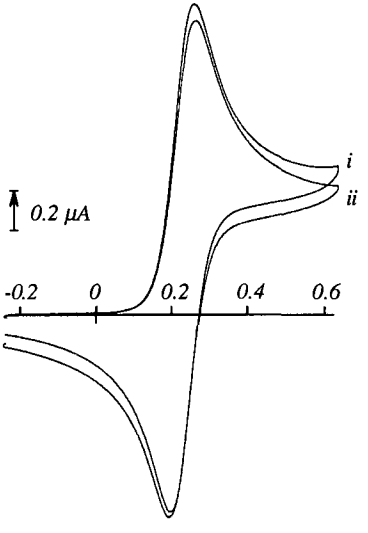

Figure 4.4: Cyclic voltammogram of 1 mM ferro-CN in 1M KCl at Pt-IDA of type A, in a single mode operation; (i) generator cycled and collector at open circuit, E_{pa}: 270 mV, ΔE_p: 75 mV; (ii) both generator and collector shorted together and cycled, E_{pa}: 260 mV, ΔE_p: 65 mV; sweep rate 50 mV/s, potential scan: -0.2 to 0.6 V.

these results depart from the theoretical 59 mV, it is worth noting that the overall diffusion field developing at the array under these experimental conditions may not be truly planar. The distortion of the diffusion flux lines at the vicinity of the microbands possibly affects the kinetics of the charge transfer process. Identical experiments performed with Pt macroelectrodes of 0.32 cm^2 have shown ΔE_p in the order 59 mV.

To investigate the transition from planar diffusion at long experimental times to again planar diffusion at short experimental times, the magnitude of the peak current observed by cyclic voltammetry is reported vs. different sweep rates. When the IDA is used in a single mode operation, the distance separating each fingers corresponds in this case to $2(W_g + W_e)$. Shielding is expected to arise as soon as the diffusion fields of each microband have met halfway. Approximating the diffusion layer thickness by the "random walk" estimation [59], the time scale of the experiment must then be kept smaller than:

$$t < (W_g + W_e)^2 / 2D \quad (4.9)$$

which gives the following condition on the sweep rate:

$$v > \frac{RT}{nF} \frac{2D}{\left(W_g + W_e\right)^2} \quad (4.10)$$

Based on computer simulation, Samuelson et al [60] have formulated that the time needed for the individual diffusion fronts of the microbands to meet halfway is given by: $t = d^2 e^{\gamma} / 4D$, where γ is the Euler's constant (γ: 0.57722) and d the diffusion length. This approximation give similar orders of magnitude for the experimental time scale than the "random" walk model.

On the other hand, edge effect initiates as soon as the diffusion field extend past the microband geometry. Similarly, the time needed for species to diffuse past the microband width is approximated by:

$$t > (W_e)^2 / 2D \quad (4.11)$$

which corresponds to sweep rates of:

$$v < \frac{RT}{nF} \frac{2D}{W_e^2} \quad (4.12)$$

For devices of type C and using D: 6.3 10^{-6} cm^2/s for 1 mM ferro-CN in 1M KCl [61], the sweep rate of interest ranges from ≈ 80 mV/s to 320 mV/s. The voltammograms present a peak-shaped response characteristic of a planar diffusion from 5 mV/s to 400 mV/s, suggesting that no steady-state regime is established under these experimental conditions. Assuming that, at low sweep rates, the IDA behaves as a macroelectrode due to shielding effects, the values of the measured peak current should tend to those calculated using the approximation for a large planar electrode [59]:

$$I_p = 0.4463 nFA_{tot} C^* \sqrt{D \frac{nF}{RT} v} \quad (4.13)$$

where A_{tot}: 0.01 cm^2 corresponds to the entire surface occupied by the array. On the other hand, at high sweep rates, if the IDA behaves as a sum of m independent microbands, the measured values should be comparable to the those given by the approximation of the peak current at a single microband [62], multiplied by m:

$$I_p = mnFDC^* b \left(0.439p + 0.713p^{0.108} + 0.614p/\left(1 + 10.9p^2\right)\right) \quad (4.14)$$

where:

$$p = \sqrt{nFvW_e^2/RTD}$$

These assumptions are confirmed in figure 4.5, where the measured and the calculated values are reported versus the square root of scan speed. It can be seen that, the experimental curve follows eq. 4.14 at sweep rates higher than 360 mV/s, whereas it tends to eq. 4.13 at low sweep rates until convection sets in. Quasi steady-state regime is not established, and the diffusion field evolves from one planar diffusion to another. Similar observation are made with devices of type B and C. These experimental results confirm that the hemicylindrical diffusion fields developing at the adjacent microbands interpenetrate before a steady-state diffusion regime is reached.

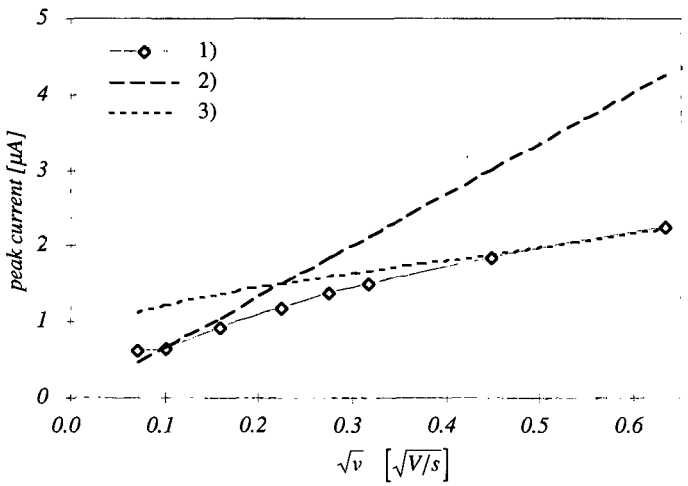

Figure 4.5: Peak current (background corrected) vs. square root of scan speed for 1 mM ferro-CN in 1M KCl, in a single mode operation, generator potentiostated (-0.2 to 0.6 V) and collector at open circuit; sweep rates of 5, 10, 25, 50, 75, 100, 200, and 400 mV/s; 1) measured peak current with IDAs of type C; 2) calculated peak current for long time scale experiments (eq. 4.13); 3) calculated peak current for planar diffusion for short time scale experiments (eq. 4.14). Experimental data recorded by digital oscilloscope (Hewlett Packard).

dual mode operation

Generation-collection experiments are carried out by cyclic voltammetry in 1 mM ferro-CN in 1 M KCl. The generator potential is varied linearly from -0.2 to 0.6 V at a sweep rate of 50 mV/s, while the collector is held at -0.2 V. Background currents are measured in degassed solution prior adding the ferro-CN. The generator and collector limiting currents, the collection efficiencies ϕ_{ss} and the number of redox cycles N_{rc} are summarized in table 4.2 for the different geometric parameters. ϕ_{ss} and N_{rc} are respectively calculated with eq. 4.1 and 4.4. The real electrode width and gap are evaluated by scanning electron microscopy (Stereoscan, Cambridge).

Figure 4.6a shows cyclic voltammograms of generation-collection experiments with IDAs of type A, B and C. The generator current I_g (upper traces) corresponds to the oxidation of Fe^{2+} to Fe^{3+}, whereas the collector

current I_c (lower traces) is representative of the reduction of Fe^{3+} to Fe^{2+}. In spite of the fact that the collector is held at a constant potential value, the aspect of I_c is similar to I_g, provided that most of the produced Fe^{3+} reaches the collector and that most of the converted Fe^{2+} diffuses back to the generator. For the three sets of experiment, I_g and I_c show diffusion limited "plateaus" characteristic of a steady-state diffusion regime. These steady-state currents are observed from 5 to 200 mV/s, with no change in the collector response, whilst the generator response becomes affected by charging current as the sweep rate increases.

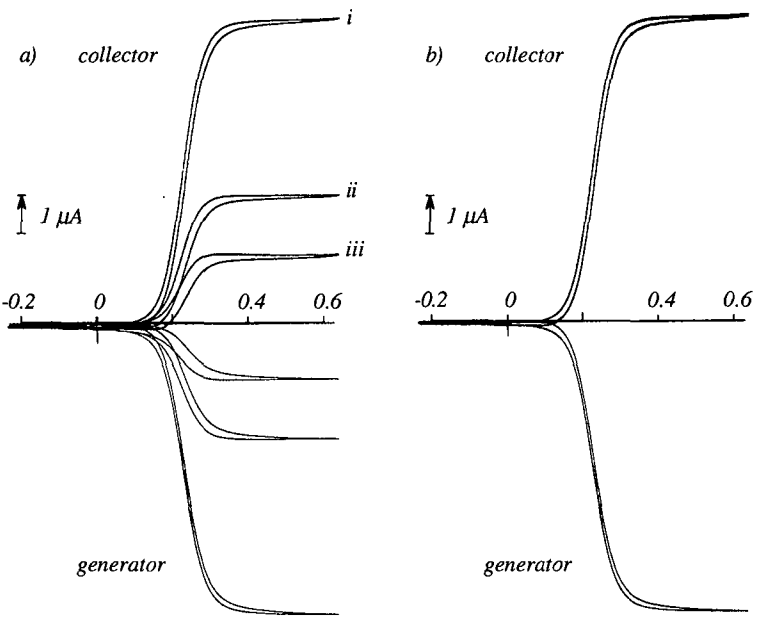

Figure 4.6: a) Cyclic voltammograms of 1mM ferro-CN in 1M KCl at Pt-IDA of type A (i), B (ii), C (iii) in a dual mode operation; sweep rate 50 mV/s, generator potential scan: -0.2 to 0.6 V, collector potential: -0.2 V.
b) Typical overlying cyclic voltammograms recorded at a Pt-IDA of type A in a dual mode operation, when the role of the electrodes acting as generator and collector are exchanged; same experimental conditions as above.

4.4.2 Evaluation of the relevant parameters

When comparing the experimental limiting currents, I_g and I_c, to the values calculated using eq. 4.6, a very good agreement with the generator current is found. When normalizing I_g by m for the three devices A, B, and C gives respectively 64, 66, 68 10^{-9}A/number of pairs, shows that the ratio W/W_g is not perfectly equivalent for all three devices.

The values of ϕ_{ss} are comparable to those obtained in [4] for similar geometric parameters and experimental conditions. The linear regression of ϕ_{ss} with the average diffusion length W_d (eq. 4.2) gives a good linear fit (r: 0.999), and suggests that W_d is a suitable parameter to evaluate the geometry dependence of ϕ_{ss}. Note that identical regression coefficient is obtained when replacing the values of W_d with those corresponding to W_g. This is probably the consequence of very close values of W_g and W_e.

To calculate N_{rc}, ϕ_1 and ϕ_2 must be obtained by using one side of the IDA as generator and the other as collector electrode, and vice versa. exactly overlying voltammograms are obtained for all of the devices (fig. 4.6b). Niwa et al. [4] have suggested that, since the accuracy of N_{rc} is largely governed by the errors on ϕ_1 and ϕ_2 when both are close to unity, N_{rc} can be evaluated from the amplification rate A_r. According to the definition of A_r (eq. 4.3), the generator current without feedback $I_{g,o}$, i.e. in a single mode operation, must be measured in a quasi-steady-state regime. Consequently, the time window of the experiment has to be defined in order to prevent shielding effects in the lower time scale and planar diffusion in the higher time scale. From the preceding experiment in a single mode operation, none of the device A, B nor C have shown a quasi steady-state regime.

Device	W_e [μm]	W_g [μm]	I_c [μA]	I_g [μA]	I_{lim}†[μA]	ϕ_{ss}	N_{rc}
A	*2.3*	*1.7*	*7.7*	*8.0*	*8.3*	*0.96*	*12.8*
B	*5.7*	*4.7*	*3.0*	*3.3*	*3.2*	*0.91*	*5.8*
C	*10.5*	*9.5*	*1.4*	*1.7*	*1.6*	*0.82*	*3.1*

Table 4.2: Geometric parameters W_e and W_g, measured I_g and I_c, calculated I_{lim} and ϕ_{ss}. Composition of the solution and conditions of experiment are reported in figure 4.6a.
†: Limiting current calculated using eq. 4.6, F: 96484 C/eq, D: 6.3 10^{-6} cm^2/s.

4.5 Characterization of the C-IDAs

Emphasis is first put on the physical characteristics of the "as deposited" sputtered-C thin-films, as these layers are obtained by a newly developed deposition process and have not yet been characterized. The electrochemical properties of sputtered-C macroelectrodes and C-IDAs are then evaluated by cyclic voltammetry, with and without pretreating the electrode surface. Ferrocyanide and dopamine are used as redox models. The analytical performances of C-IDAs are finally outlined by two sets of experiments involving dopamine and acetaminophen.

chemicals, apparatus and procedure

The homogeneity of the deposit is checked by visual inspection, optical (Nikon) and scanning electron microscopy (Stereoscan, Cambridge). The surface roughness of the layer is estimated by atomic force microscopy (NanoScopeIIIa, Digital Instruments). The crystallographic arrangement of the sputtered-C is investigated by Raman spectroscopy (Renishaw). The sheet resistivity is measured by a computer driven four-point probe (Prometrix, Omnimap RS50/e).

Electrochemical experiments are performed using a three electrode cell of 25 ml (Metrohm) with, unless noted otherwise, a saturated calomel reference electrode (SCE) and a Pt wire counter electrode. Dopamine (3,4-di hydroxyphenethylamine, DA), acetaminophen (N-acetyl-p-aminophenol, APAP) are purchased from Sigma, and ferro-CN ($K_4[Fe(CN)_6]$) from Merck. Solutions are freshly prepared in a phosphate-saline buffer of pH 7 (PBS) for DA or APAP, and in 1 M KCl for ferro-CN. Cyclic voltammograms are recorded with an IBM Voltammetric Analyzer (EC/225). Unless noted otherwise, the potential is swept at 50 mV/s from -0.2 to 0.6 V for DA and ferro-CN, and from -0.2 to 0.8 V for APAP. For generation-collection experiments, an in-house built bipotentiostat is used (Appendix A). In this case, the generator potential is swept at 50 mV/s, in the same potential range than for a single operation mode, while the collector potential is held constant at -0.2 V. New electrodes are used for each set of experiments and background currents are recorded systematically. All solutions are degassed with N_2 prior any measurement for 15 minutes. Commercial glassy carbon electrodes are a kind donation of Metrohm, CH.

4.5.1 Physical properties of sputtered-C

The deposits present a smooth and mirror-like aspect when inspected visually. Features of typically several nm are distinguished by atomic force microscopy and a typical surface roughness of 3 nm is measured (fig. 4.7).

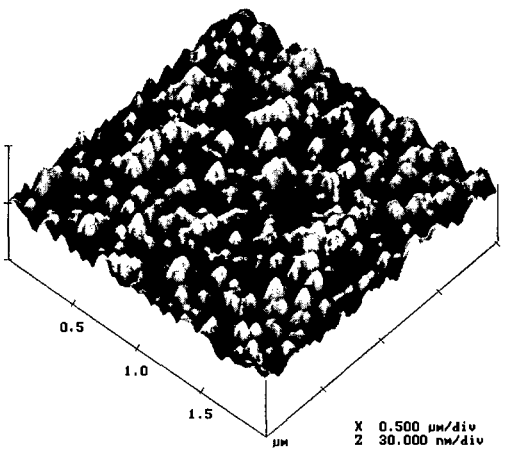

Figure 4.7: Typical AFM picture of "as deposited" sputtered-C layer surface topography; estimated average surface roughness: 2,7 nm.

The Raman spectrum of the "as deposited" thin-film carbon displays two large peaks at 1600 and 1360 cm^{-1}, that resemble to those generally obtained for amorphous or glassy carbon materials (fig. 4.8). Whereas the former vibrational mode is characteristic of all forms of graphite and is associated with crystalline graphite, the latter mode denotes that the graphite microcrystals are small and disordered. This spectrum suggests that the sputtered-C film has a glassy carbon morphology [48, 49, 63-65].

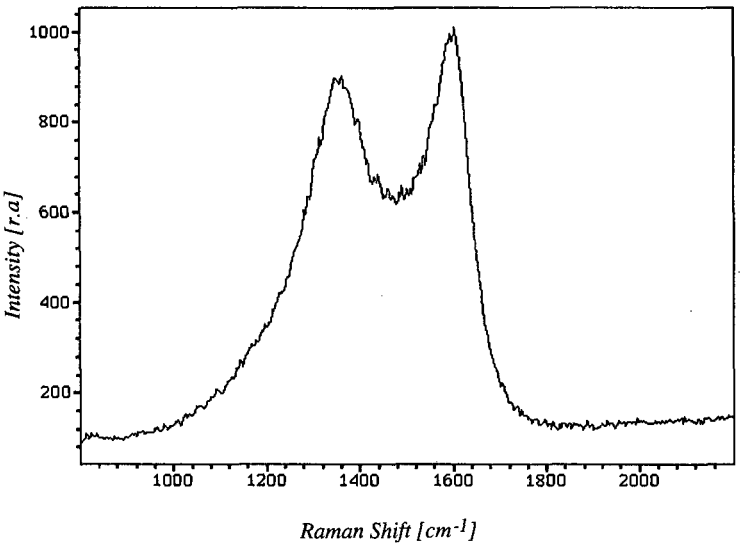

Figure 4.8: Raman spectrum of the sputtered-C deposit.

The sheet resistivity of the C layer is averaged over the entire wafer surface, right after the deposition step. A mean value of 80 Ω/❑ with standard deviation of 4 % (n = 48) is measured from batch to batch. A typical bulk resistivity of 3.2 10^{-3} Ωcm is calculated for films 4000 Å thick. This value falls within the range of those observed for pyrolytic and vitreous carbon [48, 49, 53], and is comparable to that obtained by high temperature pyrolysis [24].

The thickness of the sputtered film is measured after patterning with a surface profilometer Alpha-step 200 from Tencor Instruments (USA). A diamond-coated stylus (ø 12.5 μm) is scanned over the wafer surface to measure the height of a step, from the thin-film surface to the substrate surface. The deflection of the stylus is electronically recorded and converted by software to provide an image of the measured topography. Features in the scale of 100 Å are possibly measured with a vertical resolution ca. 10 Å. Excellent agreement is found between the thickness of the C-deposit estimated from the deposition rate and that measured with the profilometer.

4.5.2 Electrochemical response of "as deposited" sputtered-C layers

The electrochemical response of the sputtered-C layers is first assessed on macroelectrodes (26 ± 2 mm^2) obtained by cleaving section of the wafer right after the deposition process. In this case no patterning is performed and the "as deposited" properties are determined.

background features

The background current for C electrode varies greatly with the history of the electrode surface, through the contribution of the double layer capacitance and the redox process of eventual functional groups [47]. These background features are observed by carrying out cyclic voltammetry in 1 M KCl. For all investigated C thin-films, no peaks attributed to surface contamination or functional groups are observed, and background voltammograms remain unchanged after several scans. The double layer capacitance is calculated from the magnitude of the charging current [59]. Sweep rates between 5 and 100 mV/s are used to check for the linear relationship of the charging current vs. sweep rate. Excellent linear correlation is obtained confirming that the measured current is representative of the charging process. Assuming that the electrode area is 0.26 ± 2 cm^2, a double layer capacitance per unit area in the range of 10-20 $\mu F/cm^2$ is calculated. These experimental results are in good agreement with the values reported in the literature for amorphous carbon [48, 50] and fall between the values for highly ordered and disordered C materials [47].

ferro-CN and DA models

Figure 4.9a shows a typical voltammetric curve of ferro-CN oxidation, recorded with an "as deposited" sputtered-C macroelectrode. A peak separation of ΔE_p : 100 mV is indicative of a quasi-reversible process, and suggests that the sputtered-C surface has a high exposed edge plane density [66, 67]. Typical electrode surface area of ≈ 0.25 cm^2, calculated from the peak current magnitude (eq. 4.13) with a diffusion coefficient of D: 6.3 10^{-6} cm^2/s, agrees fairly well with the geometric surface estimated visually.
The peak separation observed for DA ΔE_p : ≈ 290 mV shows that the kinetics of the DA oxidation is somewhat slower, and that the proton-coupled electron transfer reaction is probably hindered due to the absence of functional groups (fig 4.9b).

4.5.3 Incidence of the electrochemical activation

Surface activation is extensively used to improve the electrochemical response of various carbon materials. As possible improvement mechanism, it has been proposed that surface activation i) increases the concentration of surface functional groups promoting proton-coupled transfer reactions, ii) exposes fresh edge planes susceptible to act as electron transfer sites, and iii) increases the active area by the modification of the surface roughness or the formation of a porous layer. It is also reported that surface activation usually increases the background current. Among the various activation techniques

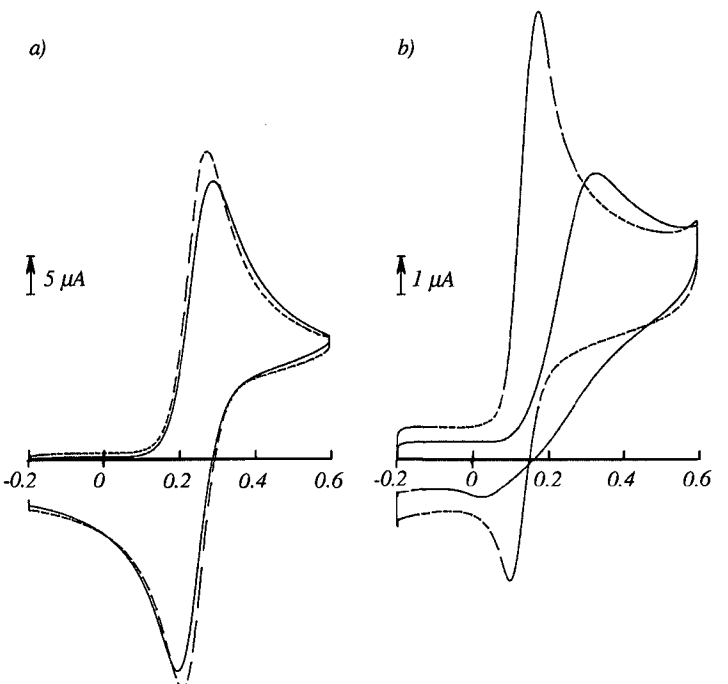

Figure 4.9: Cyclic voltammograms recorded at "as deposited" (solid lines) and electrochemically pretreated (dotted lines) sputtered-C macroelectrodes;
a): 1 mM ferro-CN in 1M KCl; potential range: -0.2 to 0.6 V (SCE); sweep rate 50mV/s; not pretreated: E_{pa}: 290 mV, ΔE_p: 100 mV; pretreated: E_{pa}: 280 mV, ΔE_p: 70 mV;
b): 0.1 mM DA in PBS; potential range: -0.2 to 0.6 V (SCE), sweep rate 50 mV/s; not pretreated: E_{pa}: 330 mV, ΔE_p: 290 mV; pretreated: E_{pa}: 165 mV, ΔE_p: 65 mV.

[48], electrochemical pretreatment is an attractive and simple method [68-70]. On the basis of the best compromise between the advantages of activation and the increase of the background current, the procedure described by Cabanis et al. [71] yields the best results for our sputtered-C electrodes. The activation cycle consists in applying 1.4 V for 1 min followed by 30 s at -0.6 V vs. sulfate reference in non-degassed 1 M H_2SO_4. The surface can be activated several times ($\approx$ 5) with a corresponding increase of the charging current. Repeated activation procedures have demonstrated that carbon films obtained by the actual deposition process retain their adhesion until being fully consumed. C layers obtained by an earlier deposition process have shown poor adhesion as the layers lifted off during intense electrochemical pretreatment.

background features

To observe the presence of activated functional groups on the C surface, voltammograms are either recorded directly after pretreatment in the same H_2SO_4 solution (50 mV/s, -0.6 to 1.4 vs. saturated sulfate reference), or after carefully rinsing the electrode surface in DI water (without drying) and immersing the electrode in a solution of degassed 1 M KCl (50 mV/s, -0.2 to 0.6 V vs. SCE). In either case, the charging current is larger by a factor of 2 to 3, and no peaks attributed to functional groups are observed [72]. AFM pictures of the C surface recorded right after the electrochemical activation indicate that a noticeable surface roughening has occurred as the average roughness measured this time reaches 6.3 nm (fig. 4.10). Since this value is comparable to that of the double layer thickness ($\approx$ 10 nm), it is assumed that the increase of the charging current is mostly caused by a corresponding increased of the electrode surface area. Yet, the presence of eventual non-active groups created at the electrode surface and modifying the properties of the interface cannot be totally excluded.

ferro-CN and DA model

Surface activation slightly improves the kinetics of ferro-CN oxidation. The peak separation decreases from ΔE_p: 100 mV to 70 mV, with a shift of the anodic peak from 290 mV to 280 mV (fig 4.9a). The magnitude of the peak current remains comparable to that observed at the non pretreated electrode, and thus suggests that the electrode surface area has not changed. This

apparent contradiction can be explained by the fact that apparition of a peak current is a diffusion-controlled process. Hence, surface roughness smaller than the diffusion layer thickness does not affect the magnitude of the peak current.

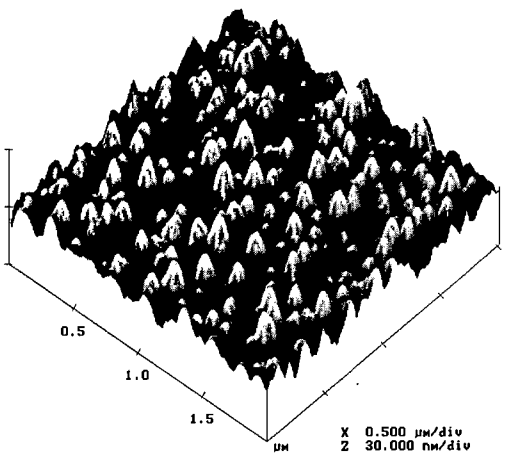

Figure 4.10: AFM picture of the surface topography of a sputtered C layer, after electrochemical pretreatment; estimated average surface roughness : 6.3 nm.

The effect of the surface activation on the reversibility of the DA oxidation reaction is more visible. The oxidation peak potential is shifted from 330 mV at an unpretreated electrode to 165 mV at an activated electrode (fig. 4.9b). Moreover a reduction peak is clearly observed on the reverse sweep at 100 mV, further confirming the enhanced reversibility of the reaction. The peak separation of ΔE_p: 65 mV departs from the theoretical value for a reversible reaction involving a two charges transfer process (28 mV), but is qualitatively comparable to that observed at a commercial glassy C electrode activated by the same procedure (fig. 4.11a). The difference between both current magnitudes arises from slightly different electrode areas.

To assess the duration of surface activation when the electrode are kept under simple storage conditions (unsealed containers), the responses of freshly activated electrodes are compared to those of electrodes that have

been activated 6 months earlier. As shown in the figure 4.11b, the electrochemical pretreatment remains effective as the pretreated surface still offers improved characteristics. It is anticipated that surface activation can be carried out as a manufacturing step to produce ready-to-use electrodes.

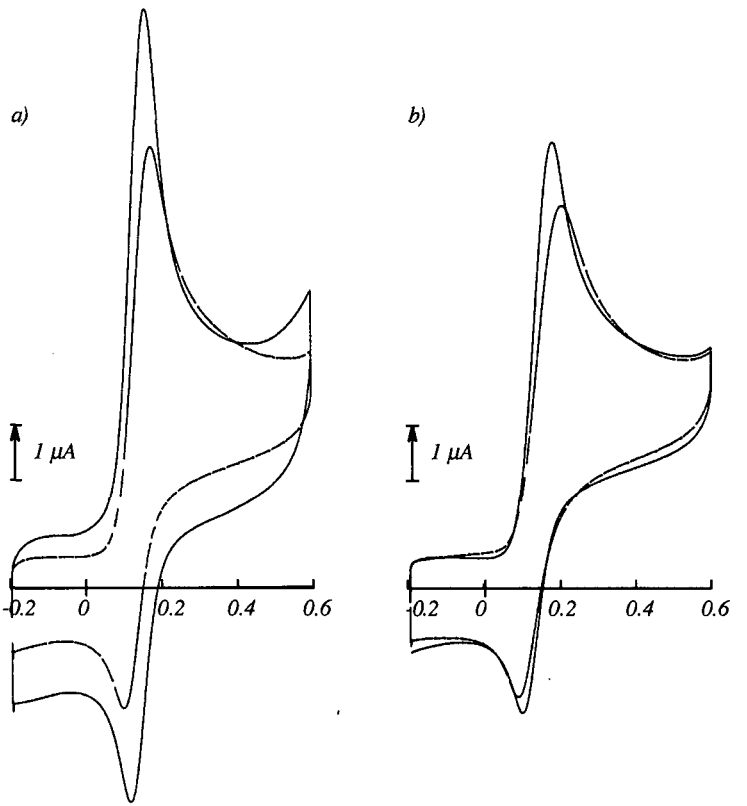

Figure 4.11: Cyclic voltammograms of 0.1 mM DA in PBS; a): electrochemical response of activated sputtered-C macroelectrode (dotted line) vs. activated commercial glassy C electrode (solid line); b): electrochemical response of previously activated (dotted line) vs. newly activated (solid line) sputtered-C macroelectrodes; potential range: -0.2 to 0.6 V (SCE); sweep rate 50 mV/s.

4.5.4 Incidence of the fabrication steps

To distinguish whether the electrochemical response of the C layer is affected by the technological steps involved in the fabrication of C-IDAs, a panel of macroelectrodes of "as deposited" sputtered-C is submitted to simulated process steps. In the case of the fabrication procedure a) the electrodes are exposed to O_2 plasma for a time corresponding to the photoresist stripping (2 min). In the case of procedure b), 500 Å Ti are deposited on the electrodes and removed in BHF (2 min). The incidence of these technological steps on the quality of the electrochemical response is evaluated by cyclic voltammetry using DA oxidation in PBS as diagnostic criterion.

Whereas no significant influence on the background current nor on the DA response is observed after submitting the electrodes to BHF (fig 4.12b), the

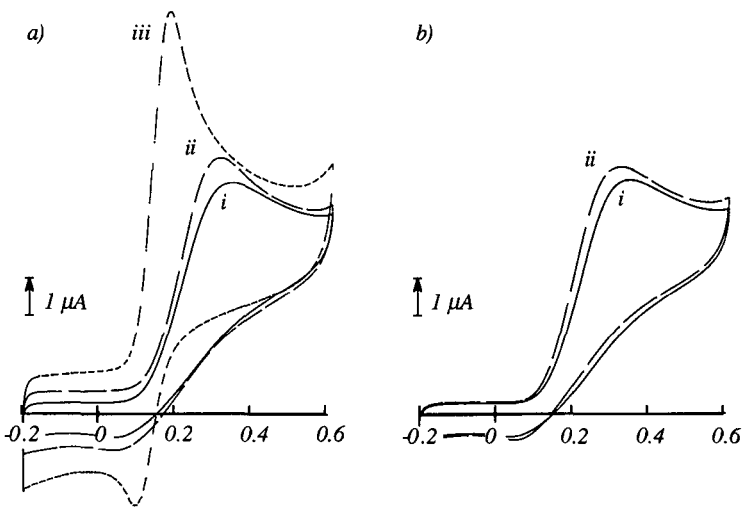

Figure 4.12: 0.1 mM DA oxidation in PBS at sputtered-C; a): i) unpretreated, ii) exposed to O_2 plasma (2 min), iii) electrochemically pretreated; b): i) unpretreated, ii) submitted to BHF (2 min); potential range: -0.2 to 0.6 V (SCE), sweep rate 50 mV/s.

electrodes exposed to O_2 plasma show a slightly modified voltammogram (fig. 4.12a). Although the strong oxidizing environment of O_2 plasma has been reported as means of surface activation [73], no improvement of the DA response is observed in our case. Moreover, since the capacitive current has increased by a factor of 1.5 without any benefits, the choice of a Ti mask for the patterning process in O_2 plasma appears to be the most adequate in terms of background current and is retained for the fabrication of the C-IDAs.

4.5.5 Electrochemical response of C-IDAs

As the bulk resistivity of C is about 3 orders of magnitudes larger than that of most metals, the resistance generated by the electrode geometry can introduce a significant ohmic drop affecting the peak separation. The electrode resistance and the order of magnitude of the ohmic drop are first evaluated. The electrochemical behavior of the C-IDAs is then investigated for a single operation mode, with and without surface activation. As discussed for Pt-IDAs, shielding effect gives rise to peak-shaped voltammograms. The peak separations for ferro-CN or DA can be qualitatively compared to those obtained at C macroelectrodes. Dual mode operation is investigated as for Pt devices.

estimation of the electrode resistance

The resistance corresponding to one side of the IDA is calculated using eq. 2.6, by multiplying the sheet resistivity measured by the four-point probe (80 Ω/❑) by the number of squares L/W given by geometric dimensions of the lead and the microbands. A value of ≈ 800 Ω is found for the three designs (A, B, and C) resulting in an ohmic drop of less than 1 mV for a current of 1 μA. This ohmic drop is however overestimated, as it assumes that the current flows entirely across the electrode resistance, i.e. that the charge transfer only occurs at the tip of the microbands. This is obviously not the case, as besides the fact that the entire surface of the microbands and the lead are exposed to the solution and should participate to the charge transfer, most of the electrode reaction takes place where the electrode resistance is smaller, i.e. the closest to the bonding pads.

single mode operation

Cyclic voltammetry is performed with C-IDAs of type A, both electrodes shorted together. Solutions of 1 mM ferro-CN in 1 M KCl, and 0.1 mM DA in PBS are used. The potential is varied linearly from -0.2 to 0.6 V at 50 mV/s.

The peak separations values for ferro-CN and DA are comparable to those obtained at macroelectrodes (table 4.3). These results suggest that i) under these experimental conditions, the electrochemical process is less affected by the inhomogeneity of the diffusion field, ii) the ohmic drop generated by the geometric dimensions of the electrode for this current magnitude is negligible, and iii) the electrochemical response is not affected by the C-IDA fabrication process.

peak separation	*"as deposited"*	*C-IDAs*
ΔE_p *ferro-CN*	*70 mV (100 mV)*	*75 mV (90 mV)*
ΔE_p *DA*	*65 mV (≈ 290 mV)*	*70 mV (≈ 250 mV)*

Table 4.3: Peak separation after surface activation at "as deposited" macroelectrode and C-IDAs of type A operated in a single mode both electrodes shorted together; values of ΔE_p measured without surface activation are given in brackets.

dual mode operation

Cyclic voltammetry is performed with C-IDAs of type A, B and C, in a solution of 1 mM ferro-CN in 1 M KCl. The generator potential is varied from -0.2 to 0.6 at 50 mV/s, whilst the collection is held at -0.2 V. Collection efficiency ϕ_{ss} and the number of redox cycle N_{rc} are calculated using the eq. 4.1 and 4.4. The collector current is estimated with eq. 4.6, using F: 96484 C/eq and a diffusion coefficient for ferro-CN of D: 6.3 10^{-6} cm^2/s.

The collection efficiency and number of redox cycles obtained at unpassivated C-IDAs cannot be compared to those obtained at the passivated Pt-IDAs. As discussed in section 4.3.1, for unpassivated devices, the generator current is increased by the charge transfer taking place at the lead, whereas the collector current is solely dependent of the redox cycling occurring at the interdigitated microbands. A good estimation of the cycling process can however be made by comparing the limiting currents measured

at the collector of unpassivated and passivated IDAs. As shown in table 4.4, the values of the collector current for the different designs are comparable to those previously observed at Pt-IDAs and are in good agreement with the approximated values of the limiting current. Therefore, in spite of fact that values of ϕ_{ss} and N_{rc} would suggest that less of electrochemical amplification is achieved at unpassivated devices, similar values of collector current confirm that the use of IDAs without passivation remains interesting.

Device	W_e *[μm]*	W_g *[μm]*	I_c *[μA]*	I_g *[μA]*	I_{lim}†*[μA]*	ϕ_{ss}	N_{rc}
A	*2.2*	*1.9*	*8.5*	*9.6*	*8.0*	*0.89*	*4.8*
B	*5.1*	*4.9*	*3.6*	*4.7*	*3.1*	*0.77*	*2.5*
C	*10.1*	*9.9*	*1.7*	*2.8*	*1.6*	*0.61*	*1.6*

Table 4.4: Geometric parameters W_e and W_g, measured I_g and I_c, calculated I_{lim} and ϕ_{ss}. Composition of the solution and conditions of experiment are mentioned in text.
†: Limiting current calculated using eq. 4.6, F: 96484 C/eq, D: 6.3 10^{-6} cm^2/s.

Generation-collection experiments are carried out with C-IDAs of type A, in solution of 0.1 mM DA in PBS. The generator potential is swept between -0.2 and 0.6 at a sweep rate of 50 mV/s and that of the collector is held at -0.2 V. Cyclic voltammograms are successively recorded with no surface activation, after pretreating either the generator or the collector, and after the pretreatment of both electrodes.

The curves reported in figures 4.13 show that the response of DA is greatly improved when the generator is activated, whereas the sole pretreatment of the collector has almost no effect. The case of both electrodes activated appears to be the most favorable in terms of collector response. It is worth noting that, since the collector is held at constant potential, its response is not affected by charging current. The collector can thus be pretreated without decreasing the benefits of surface activation.
Note that the oxidized state of DA is known to be unstable and easily change into an indol form [74]. Since the collection efficiency obtained for DA (ϕ_{ss}: 0.84) is comparable to that observed for ferro-CN, the lifetime of the oxidized DA is sufficiently long to allow the species to cross the gap and be detected at the collector. As discussed in section 4.3.1, values of ϕ_{ss} tending to 0.96 are eventually measured by reducing the sweep rate to 2 mV/s.

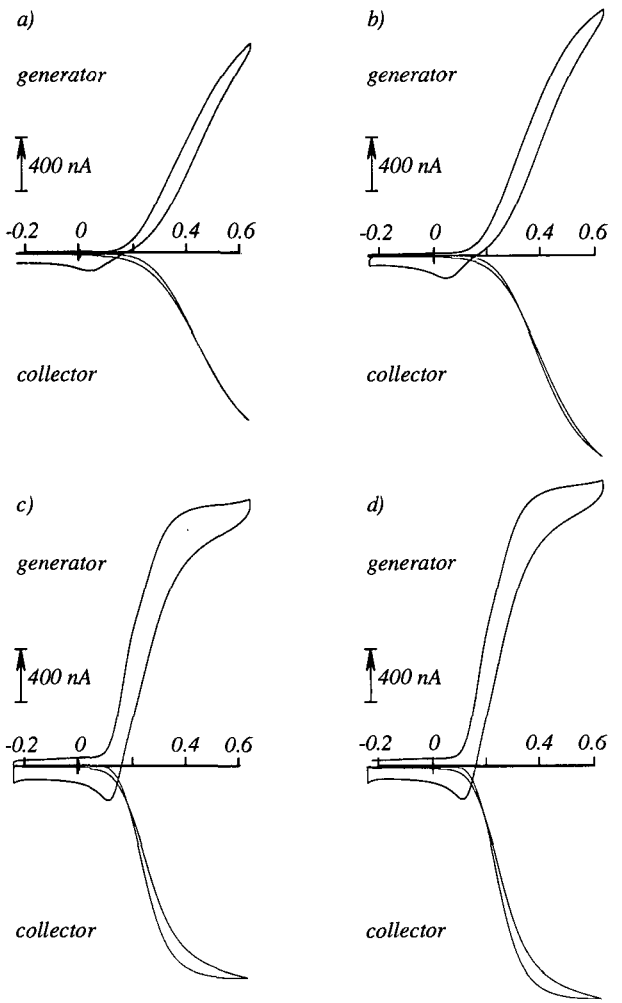

Figure 4.13: Generation collection voltammograms of 100 μM DA in PBS (pH 7) at a C-IDA of type A; a) neither electrode pretreated; b) collector electrode pretreated; c) generator electrode pretreated; d) both collector and generator electrodes pretreated; The generator potential is cycled from -0.2 to 0.6 V at 50 mV/s, the collector potential is held constant at -0.2 V.

4.5.6 Applications of C-IDAs

The electrochemical redox cycling significantly amplifies the current response of reversible and quasi-reversible redox species. Combined with the absence of charging current at the collector electrode, these two features are particularly interesting in electroanalysis. In the following section, the use of C-IDAs in two analytical applications is emphasized.

detection of dopamine

C-IDAs have been conveniently used as electrochemical detector in flow injection analysis or high performance liquid chromatography for the detection of the catecholamines in biological fluids. It has been demonstrated that extremely low detection limits can be achieved by redox cycling [6].

The calibration curve for DA in a PBS (pH 7) is obtained in a dual mode operation with a C-IDA of type A, both collector and generator electrodes electrochemically pretreated according to the surface activation procedure described in section 4.5.3. The calibration plot is built by reporting the current measured at the collector, i.e. the reduction current of DA.

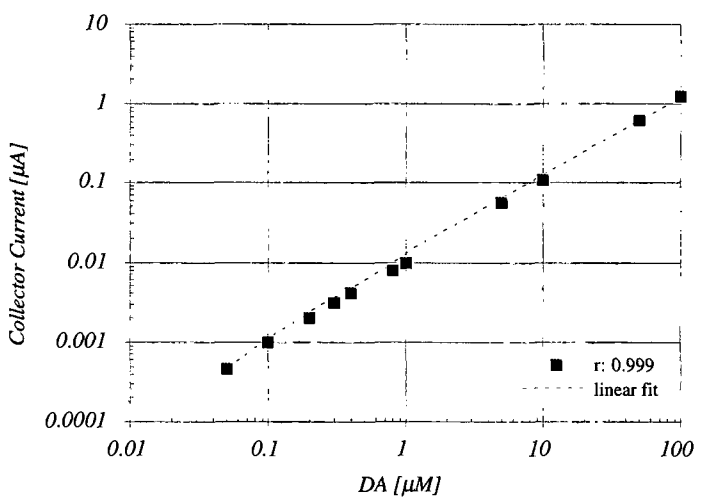

Figure 4.14: Calibration curve of DA in PBS (pH 7); collector current recorded at a C-IDA of type A; concentration range of 50 nM to 100 μM; sensitivity: 12.7 nA/μM.

A very good linear fit (r: 0.999) is found between the response of the collector and DA over a concentration range of 50 nM to 100 μM (fig. 4.14). An average sensitivity of 12.7 nA/μM is measured. Without specially dedicated low noise electronics or Faraday cage, the lowest detectable concentration of DA is of 50 nM. This detection limit is 10 times lower than that obtained in a single mode operation, and 5 to 20 times the values reported for microelectrodes based on carbon fibers [75, 76].

detection of acetaminophen

The electroanalysis of acetaminophen (APAP), an aspirin substitute, and the electrochemistry of its metabolites are of interest for the elucidation of the acetaminophen toxicity mechanism [77-79]. This example clearly illustrates the advantageous features of the IDAs for both aspects of interest, i.e. detection and mechanistic information.

The calibration curve for APAP in a PBS pH 7 solution is obtained in a dual mode operation by reporting the current measured at the collector, i.e. the cathodic current representing the reduction of NAPQI.
Excellent linear relationship (r: 0.999) is found between the collector current

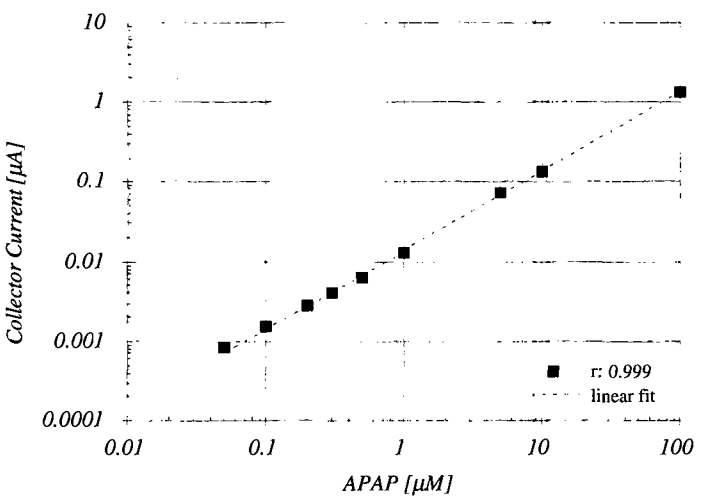

Figure 4.15: Calibration curve of APAP in PBS (pH 7); collector current recorded at a C-IDA of type A; concentration range of 50 nM to 100 μM; sensitivity: 13.6 nA/μM.

and the APAP concentration from 50 nM to 100 μM (fig. 4.15). The average sensitivity corresponds to 13.6 nA/μM. With a collection efficiency of ϕ_{ss}: 0.96, a current amplification by a factor of ca. 13 is achieved. This redox cycling can be thus considered as an alternative approach to the chemical amplification described by Moore et al. [78].

Acetaminophen is electrochemically oxidized in a pH dependent, 2 electron, 2 protons process to *N*-acetyl-*p*-quinoneimine (NAPQI). At pH values ≥ 6, the NAPQI remains in a stable, unprotonated form that is reduced at ≈ -0.2 V (fig. 4.16).
Under more acidic conditions, NAPQI is rapidly protonated yielding an electroactive but unstable form which, upon hydrolysis results in an electroinactive form [80]. The cyclic voltammogram of the APAP in pH 2 solution at C-IDAs operated in a single mode shows no reduction peak on the reverse scan at the sweep rate of 50 mV/s (fig. 4.17). The detection of the unstable protonated NAPQI is however possible in the dual mode operation when the collector potential is set to 0.2 V (fig. 4.18). Note that this unstable form could eventually be detected by conventional cyclic voltammetry by increasing the sweep rate.

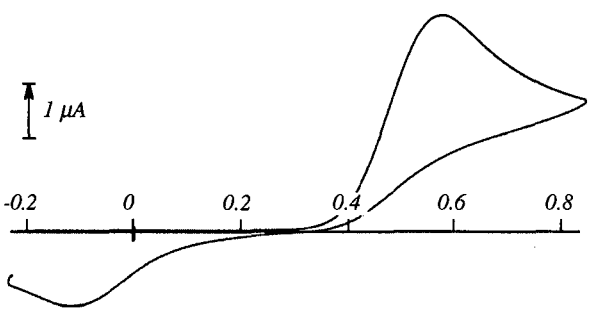

Figure 4.16: Cyclic voltammogram of 1mM APAP in PBS pH 7, at a C-IDA of type A, in a single mode operation; potential range: -0.2 to 0.8V vs. SCE; scan rate: 50 mV/s.

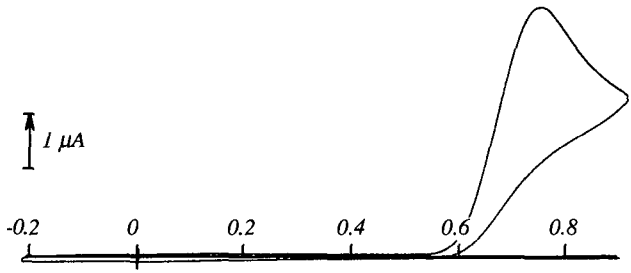

Figure 4.17: Same as figure 4.16, but in a phosphate-citrate buffer pH 2.

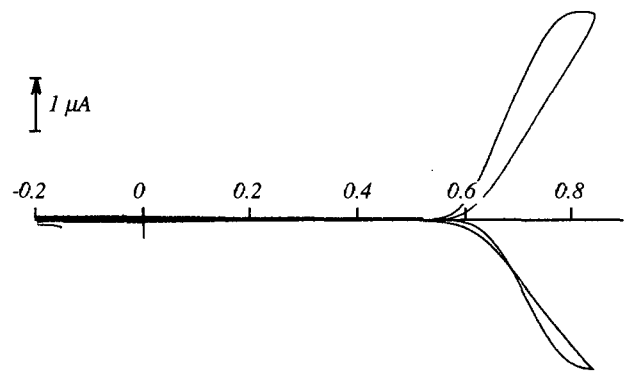

Figure 4.18: Cyclic voltammogram of 1 mM APAP in a phosphate-citrate buffer pH 2, at s C-IDA of type A in a dual mode operation; generator cycled from -0.2 to 0.8 V vs. SCE at 50 mV/s, collector held at 0.2 V vs. SCE; reduction of the protonated NAPQI is observed at the collector.

4.6 Conclusion

Carbon thin-films obtained by a low temperature sputtering deposition process have been systematically characterized. Process parameters have been optimized to achieve carbon layers presenting a good adhesion to the substrate, a low bulk resistivity and valuable electrochemical properties. The results obtained for these optimized layers have been presented.

The crystallographic arrangement and the electrochemical behavior of the sputtered carbon layer are characteristic of a glassy carbon morphology. Typical double layer capacitance of 20 µF/cm2 and bulk resistivity in the order of 3.10^{-3} Ωcm are measured. Surface activation by electrochemical pretreatment improves the kinetics of proton-coupled reactions (DA or APAP), whereas no significant effect is noticed for a direct electron transfer (ferro-CN). The electrochemical response obtained at pretreated thin-film electrodes is qualitatively comparable to that observed at commercial electrodes pretreated by the same activation procedure. Benefits of surface activation remain effective over 6 months in simple storage conditions.

Patterning in O_2 plasma with a resolution of 2 µm is demonstrated by the successful fabrication of interdigitated microelectrode arrays. The analytical performances of these devices are emphasized by the detection of two biologically important molecules, dopamine and acetaminophen. Mechanistic information on acetaminophen metabolites is assessed. Excellent linear calibration curves are obtained in both cases over a concentration range of 50 nM to 100 µm, with a detection limit of several tens of nM. Significant improvement of the detection limit is achieved by means of redox cycling.

It is observed that the valuable analytical performances of IDAs are retained without passivation. Therefore any application for which solely the collector current is measured does not require the use a top passivation layer. This observation leads to the simplification of the fabrication sequence, and allows the use of simple substrate materials that are incompatible with the deposition of LPCVD or PECVD Si_3N_4.

References

[1] Fiaccabrino G.C., Tang X.M., Skinner N., de Rooij N.F., Koudelka-Hep M., Anal. Chim. Acta, 326 (1996) 155-161

[2] Aoki A., Matsue T., Uchida I., Anal. Chem., 62 (1990) 2206-2210

[3] Slater J.M., Watt E.J., Analyst, 119 (1994) 2303-2307

[4] Niwa O., Morita M., Tabei H., Anal. Chem., 62 (1990) 447-452

[5] Takahashi M., Morita M., Niwa O., Tabei H., J. Electroanal. Chem., 335 (1992) 253-262

[6] Tabei H., Takahashi M., Hoshino S., Niwa O., Horiuchi T., Anal. Chem., 66 (1994) 3500-3502

[7] Bard A.J., Crayston J.A., Kittlesen G.P., Varco Shea T., Wrighton M.S., Anal. Chem., 58 (1986) 2321-2331

[8] Cope D.K., Tallman D.E, J. Electroana. Chem., 205 (1986) 101-123

[9] Varco Shea T., Bard A.J., Anal. Chem. 59 (1987) 2101-2111

[10] Aoki K., Morita M., Niwa O., Tabei H., J. Electroanal. Chem., 256 (1988) 269-282

[11] Aoki K., J. Electroanal. Chem., 284 (1990) 35-42

[12] Fosset B., Amatore C., Bartlet J.E., Michael A.C., Wightman M.R., Anal. Chem., 63 (1991) 306-314

[13] Fosset B., Amatore C., Bartlet J., Wightman, Anal. Chem., 63 (1991) 1403-1408

[14] Seddon B.J., Girault H.H., Eddowes M.J., J. Electroanal. Chem., 266 (1989) 227-238

[15] Amatore C., "Electrochemistry at Ultramicroelectrodes" in Physical Electrochemistry, Ed. Rubinstein, Marcel Dekker, 1995, New-York, pp 131-208

[16] Sanderson D.G., Anderson L.B., Anal. Chem., 57 (1985) 2388-2393

[17] Anderson J.L., OU T.S, Moldeveanu S., J. Electroanal. Chem., 196 (1985) 213-226

[18] Fosdick L.E., Anderson J.L., Baginski T.A, Jaeger R.C., Anal. Chem., 58 (1986) 2750-2756

[19] Fosdick LE., Anderson J., Anal. Chem., 58 (1986) 2481-2485

[20] Niwa O., Electroanalysis, 7 (1995) 606-613

[21] Niwa O., Morita M., Tabei H., Electroanalysis, 3 (1991) 163-168

[22] Niwa O., Morita M., Tabei H., Electroanalysis, 6 (1994) 237-243

[23] Niwa O., Horiuchi T., Tabei H., J. Electroanal. Chem., 367 (1994) 265-269

[24] Niwa O., Tabei H., Anal. Chem., 66 (1994) 285-289

[25] Niwa O., Morita M., Anal. Chem., 68 (1996) 355-359

[26] Tabei H., Morita M., Niwa O., Horiuchi T., J. Electroanal. Chem., 334 (1992) 25-33

[27] Niwa O., Morita M., Tabei H., J. Electroanal. Chem., 267 (1989) 291-297

[28] Tabei H., Horiuchi T., Niwa O., Morita M., J. Electroanal. Chem., 326 (1992) 339-343

[29] Niwa O., Xu Y., Halsall H.B., Heineman W.R., Anal. Chem., 65 (1993) 1559-1563

[30] Thormann W., van der Bosh, Bond A.M., Anal. Chem.., 57 (1985) 2764-2770

[31] Wollenberger U., Paeschke M., Hintsche R., Analyst, 119 (1994) 1245-1249

[32] Paeschke M., Hintsche R., Wollenberger U., Jin W., Scheller F., J. Electroanal. Chem., 393 (1995) 131-135

[33] Paeschke M., Wollenberger U., Köhler C., Lisec T., Schnakenberg U., Hintsche R., Anal. Chim. Acta, 305 (1995) 126-136

[34] Horiuchi T., Niwa O., Morita M., Tabei H., Anal. Chem., 64 (1992) 3206-3208

[35] Horiuchi T., Niwa O., Tabei H., Anal. Chem., 66 (1994) 1224-1230

[36] Bustin D., S. Mesaros, Tomcik P., Rievaj M., Tvarozek V., Anal. Chim. Acta, 305 (1995) 121-125

[37] White H.S., Kittlesen G.P., Wrighton M.S., J. Am. Chem. Soc., 106 (1984) 5375-5377

[38] Kittlesen G.P., White H.S., Wrighton M.S., J. Am. Chem. Soc., 106 (1984) 7389-7396

[39] Kittlesen G.P., White H.S., Wrighton M.S., J. Am. Chem. Soc., 107 (1985) 7373-7380

[40] Paul E.W., Ricco J.A., Wrighton M.S., J. Phys. Chem., 89 (1985) 1441-1447

[41] Nishizawa M., Matsue T., Uchida I., Anal. Chem., 64 (1992) 2642-2644

[42] Chidsey C.E., Feldman B.J., Lundgren C., Murray R.W., Anal. Chem., 58 (1986) 601-607

[43] Fritsch-Faules I., Faulkner L.R., Anal. Chem., 64 (1992) 1118-1127

[44] Feldman B.J., Feldberg S.W., Murray R.W., J. Phys. Chem., 91 (1987) 6558-6560

[45] Belmont C., Girault H.H., J. Appl. Electrochem., 24 (1994) 475-480

[46] Belmont C., Girault H.H., J. Appl. Electrochem., 24 (1994) 719-724

[47] Randin J.P., "Carbon" in Encyclopedia of Electrochemistry of the Elements, vol 7, Ed. Bard A.J., Marcel Dekker, 1976, New-York

[48] Kinoshita K., "Carbon: electrochemical and physicochemical properties", John Wiley & Sons, 1988, New York

[49] McCreery L.M., "Carbon Electrodes: structural effects on electron tranfer kinetics" in Electroanalytical Chemistry, a Series of Adances,vol 17, Ed. Bard A.J., Mercel Dekker, 1991, New-York

[50] Leon y Leon C.A., Radovic L.R., "Interfacial Chemistry and Electrochemistry of Carbon Surfaces" in Chemistry and Physics of Carbon, vol.24, Ed. Thrower P.A., Marcel Dekker, 1994 , New-York, pp 213-310

[51] Dryhurst G., McAllister D.L., "Carbon Electrodes" in Laboratory Techniques in Electroanalytical Chemistry, Marcel Dekker, 1984, New-York

[52] Gilmartin M.A.T., Hart J.P., Analyst, 120 (1995) 1029-1045

[53] Van der Linden W.E., Dieker J.W., Analytica Chimica Acta, 119 (1980) 1-24

[54] Eriksson A., Norekrans A.S., Carlsson J.O., J. Electroanal. Chem., 324 (1992) 291-305

[55] McFadden C., Russell L.L., Melaragno P.R., Davis J.A., Anal. Chem., 64 (1992) 1521-1527

[56] Saraceno R.A., Engstrom C.E., Rose M., Ewing A.G., Anal. Chem., 61 (1989) 560-565

[57] Petrov I., Ivanov I., Orlinov V., Kourtev J., Jelev J., Thin Solid Films, 185 (1990) 247-256

[58] Petrov I., Ivanov I., Orlinov V., Kourtev J., Jelev J., Thin Solid Films, 168 (1990) 239-248

[59] Bard A.J., Faulkner L.R., "Electrochemical Methods: fundamentals and applications", John Wiley & Sons, 1980, New York

[60] Samuelsson M., Armgarth M., Nylander C., Anal. Chem., 63 (1991) 931-936

[61] Adams R.N., "Electrochemistry at Solid Electrodes", Marcel Dekker, 1969, New York

[62] Aoki K., Tokuda K., J. Electroanal. Chem., 237 (1987) 163-170

[63] McCreery R.L., Packard R.T, Am. Chem. Soc, 61 (1989) 775A-788A

[64] Bowling R., Packard R., McCreery R.L., J. Electrochem. Soc., 135 (1988) 1605-1606

[65] Tamor M.A., Vassell W.C., J. Appl. Phys., 76 (1994) 3823-3830

[66] Rice R.J., Pontikos N.M., McCreery R.L., J. Am. Chem. Soc., 112 (1990) 4617-4622

[67] Kneten K., McCreery R.L., Anal. Chem., 64 (1992) 2518-2524

[68] Kepley L.J., Bard A.J., Anal. Chem., 60 (1988) 1459-1467

[69] Beilby A.L., Sasaki T.A., Stern H.M., Anal. Chem., 67 (1995) 976-980

[70] Feng J.X., Brazell M., Renner K., Kasse R., Adams R.N., Anal. Chem. 59 (1987) 1863-1867

[71] Cabanis G.E., Diamantis A.A., Murphy W.R. Jr., Linton R.W., Meyer T.J., J. Am. Chem. Soc., 107 (1985) 1845-1853

[72] Blurton K.F., Electrochim. Acta, 18 (1973) 869-875

[73] Evans J.F., Kunawa T., Henne M.T., Royer G.P., J. Electroanal. Chem., 80 (1977) 409

[74] Hawley M.D., Tatawawadi S.V., Piekarski S., Adams R.N., J. Am. Chem. Soc., 89 (1967) 447-450

[75] Kim Y.T.,Scarnulis D.M., Ewing A.G., Anal. Chem., 58 (1986) 1782-1786

[76] Kawagoe K.T., Jankowski J.A., Wightman R.M., Anal. Chem., 63 (1991) 1589-1594

[77] Vaughan P.A., Scott L.D.L., McAleer J.F., Anal. Chim. Acta, 248 (1991) 361-365

[78] Moore T.J., Nam G.G. , Pipes L.C., Coury L.A. , Anal. Chem., 66 (1994) 3158-3163

[79] Gilmartin M.A.T., Hart J.P., Analyst, 119 (1994) 2431-2437

[80] van Benschoten J.J. , Lewis J.Y., Heineman W.R., Roston D.R., Kissinger P.T., J. Chem. Ed., 60 (1983) 772-776

Individually Addressable Microelectrode Arrays

The aim of this work is to demonstrate the feasibility of a two dimensional array of 100 individually addressable microelectrodes for the mapping of electroactive species. In order to reduce the number of external connections, a multiplex is integrated "on-chip". The addressing unit is designed to offer a good signal to noise ratio for a current range of 1-100 nA.
In the following chapter, the addressing principle and the fabrication of the device are first described. The characterization of the integrated multiplex is then presented. The performances of the array are outlined by two sets of experiments illustrating the mapping properties of the device. Parts of this chapter have been published in [1,2].

5.1 Introduction

A set of microelectrodes is currently referred to as an array, regardless of its operation mode. The microelectrodes can be used simultaneously at the same potential to provide a large signal and yet exhibit a dynamic behavior similar to that of a single sensing element. Such operation mode has been discussed in chapter 3. Microelectrodes can also be individually addressed and thus offer the opportunity to collect a localized information. This ability to assess the spatial distribution of electroactive species enables prospecting fields of electrochemistry for which the electrochemical response has to be correlated to the position of the measurement, e.g. mapping of concentration gradient at interfaces [3], investigation on the interfacial mass transport [4] or extracellular detection of electroactivity in cultured cells [5-8]. This approach can be seen as complementary to the scanning electrochemical microscopy [9], and opens new possible applications where the positioning of a micromanipulator or the conditioning of the analyte sample is not

possible, such as "in situ" measurements of trace metals at sediment/water or water/air interfaces. With the same objectives and in parallel to the present work, comparable individually addressable microelectrode have been developed [10-14].

The penalty to pay when using numerous sensing elements is the corresponding large number of external connections. This problem is circumvented hereafter by choosing a simple "on chip" multiplex approach. In this case, each element of the array is sequentially addressed. The response of the selected microelectrode is collected by a single output line connected to an external potentiostat.

5.2 Theoretical Aspects

5.2.1 Addressing principle

When considering the case of a set of microelectrodes arranged in a quadratic pattern, each microelectrode can be seen as an element of a matrix of dimension n x n, and thus be referenced by the indexes of the column and the row corresponding to its location in the matrix (fig. 5.1a).
The multiplexing function is obtained by assigning two electronic switches to each microelectrode, operated by its "row" and "column" address lines (fig. 5.1b). The simultaneous activation of both address lines close the electrical circuit and connects the selected microelectrode to the potentiostat (fig. 5.2). Activating only one address line or none, leaves the microelectrode at open circuit, i.e. at the high impedance of the switch in the off mode (R_{off}). The switches are realized using the transmission gate principle [15,16], one nMOS per switch. The advantages of such multiplex are the reduced number of transistors for the assigned function and the bi-directional aspect of the switches, i.e. demultiplexing function. This architecture reduces the number of bonding pads for n^2 elements down to 2n for the address lines plus two additional pads for signal output and bulk bias (i.e. 22 connections). It must be pointed out that the chosen approach does not enable the switching

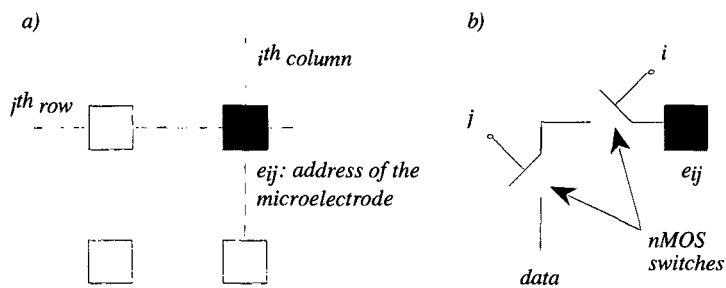

Figure 5.1: Schematic of the addressing principle.

of two or more electrodes simultaneously at different potentials and to collect individual signals. This limitation is inherent to the fact that the responses of the selected microdisk converge into an unique output line (data line) and that a single potentiostat is used for all microelectrodes.

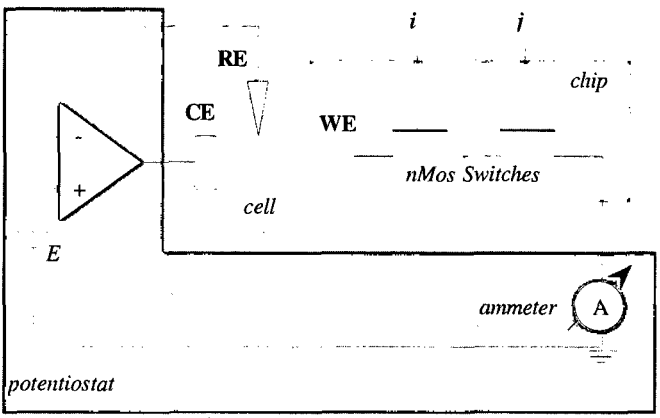

Figure 5.2: Schematic of the working principle; WE: microdisk, RE: reference electrode, CE: counter electrode, E: applied potential, i and j: address lines of the microdisk.

5.2.2 nMOS switch model

The simple description of the nMOS field effect transistor in the different operation regimes is used to model the output characteristics of a single switch. The case of a double switch configuration, i.e. two switches placed in series, is obtained by extension. A more detailed description of MOS devices and related second order effects can be found in the cited references and will not be addressed hereafter [15,17,18].

The nMOS switch is a four terminal device, namely the drain, the source, the gate and the bulk (fig. 5.3a). The drain and the source are respectively defined as the input (electrode side) and output terminals (potentiostat side) of the switch (fig. 5.3b). The "on/off" state of the switch is operated by the

voltage V_G applied to the gate terminal. The threshold potential V_T corresponds to the particular gate voltage at which the channel becomes inverted and starts being conductive. In the "on" state, the switch presents a small resistance R_{on} across the input/output terminals, whereas in the "off" state, the resistance is large but not infinite.

It is assumed that the source and the bulk are commonly grounded, and that all terminal voltages are quoted with respect to the source (fig. 5.3b). The current flowing across the switch is referred to as the drain current I_D. When the current flows from drain to source, i.e. the electrons flow goes from source to drain, I_D is given a positive sign. It is worth noting that this electronic convention is the opposite to that adopted in electrochemistry, as an electrons flow from source to drain corresponds to a reduction process.
When a MOS transistor is used as a switch, no voltage is applied to drive the drain terminal. The drain voltage V_D corresponds to the potential drop that develops across the channel resistance when I_D flows across the switch. V_D will be positive for a reduction and negative for an oxidation reaction. It is worth noting that, in the electrochemical context, the ground level of the electrode is shifted by the value of V_D, and that consequently the applied electrode potential E is affected by this additional ohmic drop.

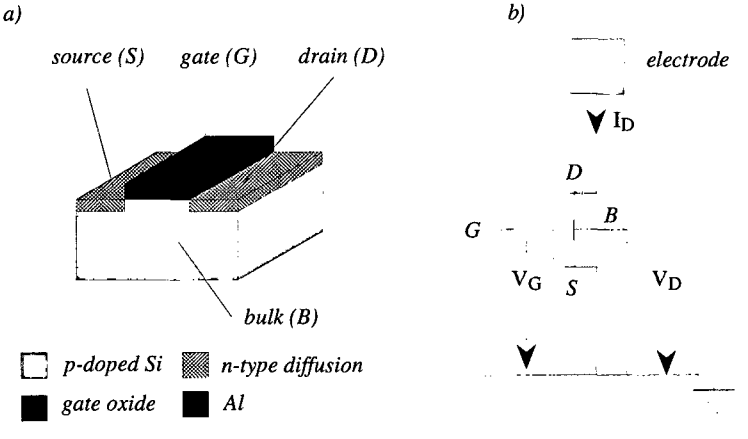

Figure 5.3: nMOS switch; a) cross section and definition of the device terminals; b) device symbol and definition of the terminal voltages.

The three distinct operation regimes of the switch are identical to those of the nMOS transistor:

i)	*subthreshold*	$V_G < V_T$
ii)	*linear*	$V_G > V_T \quad V_D < V_G - V_T$
iii)	*saturated*	$V_G > V_T \quad V_D > V_G - V_T$

subthreshold

When the switch is in the "off" state, i.e. $V_G << V_T$, the channel resistance of nMOS switches is in the order of 10^{12} Ω [15]. The switched-"off" microelectrodes are virtually disconnected from the potentiostat and left at open circuit. The subthreshold model describes how the switch turns on as V_G is increased towards V_T. In this operation regime, the semiconductor surface under the gate is only weakly inverted, and the source and the drain are separated by two back to back pn junctions. If $V_D >> kT/q$, the drain current I_D approximately follows an exponential form of the applied gate voltage:

$$I_D \approx \frac{W}{L} I'_{DO} exp\left(\frac{qV_G}{nkT}\right) \quad (5.1)$$

where W is the width and L the length of the gate, k the Boltzman constant ($1.381\ 10^{-23}$ J/°K), T the temperature in °K, q the charge of an electron ($1.602\ 10^{-19}$ C). The subthreshold slope factor n and I'_{DO} are two process-dependent parameters. The former can be used as figure of merit to assess the quality of the processed transistors. The value of n should be in the range of 1 to 2. The latter, I'_{DO}, is usually affected by leakage currents possibly flowing across the channel in the "off" mode and across the reverse biased drain/bulk pn junction. When V_G is sufficiently smaller than V_T, I_D departs from eq. 5.1 and takes a value I_{DO} defined as background current. I_{DO} must be kept below the nA since, in the worst case, the sum of leakage currents of all the "unswitched" microelectrodes adds to the measured electrochemical response of the "switched-on" electrode and thus may considerably affect the signal to noise ratio.

linear

When V_G reaches V_T, a surface inverted layer (channel) is created under the gate and the switch turns on. The source and the drain are connected by an n-type conductive surface channel through which current can now easily flow. The conductance of the channel, i.e. the channel resistance R_{on}, is modulated by varying V_G. If the drain voltage $V_D < V_G - V_T$, I_D is proportional to V_D and is given by:

$$I_D = \frac{\mu_n C_{ox} W}{L}\left[(V_G - V_T)V_D - \frac{V_D^2}{2}\right](1 + \lambda V_D) \quad (5.2)$$

where μ_n is the average surface mobility of electrons in the channel and C_{ox} is the gate capacitance per unit area. $C_{ox} = \varepsilon_{ox}/d_{ox}$, where ε_{ox}: 3.45 10^{-13} F/cm is the dielectric constant of SiO_2 and d_{ox} the thickness of the gate oxide. λ is an empirical correction factor taking into account the channel length modulation when V_D becomes comparable to $V_G - V_T$. The values of λ generally falls between 0.01 and 0.1 V^{-1}.

If $V_D << V_G - V_T$ and the channel is sufficiently long, λV_D and V_D^2 can be neglected in eq. 5.2. I_D becomes linearly dependent of V_D and the channel resistance can be expressed as:

$$R_{on,lin} = \frac{1}{\partial I_D / \partial V_D} \approx \frac{L}{\mu_n C_{ox} W (V_G - V_T)} \quad (5.3)$$

This expression shows that $R_{on,lin}$ is independent of I_D or V_D, and that the channel exhibits a constant resistance as long as the switch stays in a linear operation regime. Depending on the aspect ratio W/L, the channel resistance of nMOS switches typically ranges from a tenth to several KΩ. Assuming a surface mobility of ≈ 700 cm^2/Vs, a gate oxide thickness of d_{ox}: 800 Å, a gate voltage such as $V_G - V_T \approx$ 5 V and a ratio W/L: of ≈ 3, the channel resistance is about 2.1 KΩ. Hence, to reduce the potential drop V_D under the mV, the current magnitude of the microelectrode response must be kept below the μA. It is worth noting that, whereas it seems more favorable to use large W/L ratios to reduce the potential drop, large gate areas increase the parasitic capacitance and the reverse current of the source and drain pn junctions. The choice of the optimal gate dimensions are the result of a compromise between potential drop, switching speed and background current.

saturated

The switch enters the saturated mode when the current I_D flowing across the channel generates a potential drop V_D comparable to $V_G - V_T$. The saturation occurs when I_D approximately reaches:

$$I_{D,sat} = \frac{\mu_n C_{ox} W}{2L}(V_G - V_T)^2(1 + \lambda V_D) \quad (5.4)$$

$I_{D,sat}$ can be considered as the maximum current intensity that can possibly flow across the switch. This current driving capability of the switch, i.e. the value of the saturated current, is particularly critical upon "switching" the electrode, as large transient capacitive current resulting of the charging of the double layer will flow across the switch. In order to minimize the *RC* time constant, the switch must stay in a linear operation regime to allow fast double layer capacitance charging process. For an nMOS switch of gate dimension W/L: 3, a microelectrode of 625 μm^2, and a double layer capacitance of 20 $\mu F/cm^2$, the *RC* time constant is less than 0.5 µs provided that the switch stays in the linear operation mode. By neglecting in a first approximation the channel modulation effect, the switch remains in the linear regime as long as the current does not exceed I_D: 1 mA.
When I_D becomes comparable to $I_{D,sat}$, the channel resistance in the saturated regime can be approximated by:

$$R_{on,sat} = \frac{2L}{\lambda \mu_n C_{ox} W (V_G - V_T)^2} \quad (5.5)$$

which can be rewritten as:

$$R_{on,sat} = \frac{1 + \lambda V_D}{\lambda I_{D,sat}} \approx \frac{1}{\lambda I_{D,sat}} \quad (5.5bis)$$

emphasizing the relationship of the channel resistance with the drain current. By comparing eq. 5.5 with 5.3, it can be seen that, depending on the channel modulation factor λ, $R_{on,sat}$ is about one to two orders of magnitude larger than $R_{on,lin}$.

5.3 Fabrication of the Device

5.3.1 Design

The circuit is an array of 100 platinum microsquares of 25 μm side separated by 150 μm and arranged in a quadratic matrix of dimension 10 x 10. The overall sensing area is 2.25 mm^2 with a spatial resolution of 150 μm. The size of the microelectrodes is chosen so that the current of the electrochemical response remains sufficiently large to be easily measured (nA-μA) and yet does not generate a large potential drop V_D. As discussed chapter 3, the choice of the distance between the microelectrodes is set to avoid the occurrence of shielding. A modular approach has been followed to design the array. The repeating cell contains a square-shaped microelectrode and its two associated switches (fig. 5.4). The switches are nMOS transistors with a gate width of W: 30 μm and length of L: 10 μm. The array is produced by repeating the cell ten times across the horizontal and vertical directions.

To assess the electrical characteristics of the nMOS switch, test circuits have been designed and processed simultaneously on the same wafer. These circuits are single and double transistors in the same configuration as found in the array.

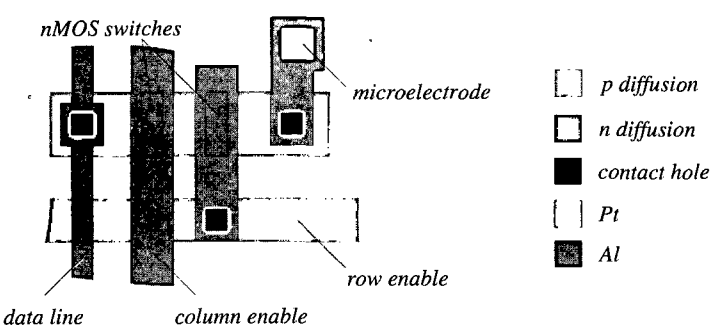

Figure 5.4: Layout of the microelectrode and its two associated switches.

5.3.2 Technological parameters

The addressable microelectrode arrays are fabricated using the technological processes described in chapter 2. The sequence of the fabrication steps is depicted in figure 5.5.
The devices are fabricated on a <100> 3 inches p-doped silicon wafer with a bulk resistivity of 5-7 Ωcm. The wafer is first cleaned by successive dips in fuming HNO_3 (10 min), BHF 1:7 (30 s) and HNO_3 70% at 115 °C (10 min). The substrate is thoroughly rinsed in DI water after each immersion.
The doping of the channel stop, the drain and the source of the transistors are respectively obtained by driving the impurities of p- and n-doped CVD oxides during the high temperature gate oxide formation. Undoped oxide is added as protective layer to prevent the out diffusion and the contamination of the oxidation furnace.

definition of the channel stop

A layer of 1000 Å thickness of p-doped CVD SiO_2 is deposited at 420°C, from a gas mixture of O_2, silane and diborane. Argon is used as neutral gas carrier. This doped layer forms the doping source for the channel stop. A protective layer of 3000 Å of undoped CVD SiO_2 is formed similarly without adding diborane to the gas mixture. The areas where the channel stop are to exist are protected by photolithography using the OMR 83 60cp. Exposed SiO_2 is etched in BHF 1:7 to delineate the active area of the transistors (sources, drains and gates) (fig 5.5a).

definition of the source and drain

The photoresist is removed and 1000 Å thick n-doped CVD SiO_2 layer is deposited at 350°C, from a gas mixture of O_2, silane and phosphine. Argon is again used as neutral gas carrier. This doped layer forms the doping source for the sources and drains of the transistors. The protective layer of undoped CVD SiO_2 is formed similarly without adding phosphine to the gas mixture. The area of the source and drain are protected by photolithography using the OMR 83 60cp. Exposed SiO_2 is etched in BHF 1:7 to delineate the gates of the transistors (fig 5.5b).

formation of the gate oxide and diffusion of the impurities

The photoresist is stripped and a gate oxide of 800 Å thickness is formed by thermally oxidizing the exposed Si at 1100°C under a controlled flow of O_2 (fig 5.5c). This thermal process allows the diffusion of the impurities into the bulk silicon and densifies the CVD oxides. The gate oxide is then submitted to a low temperature (450 °C) hydrogen annealing to minimize the density of trapped charges at the interface of the Si/SiO_2.

contact opening and metal lines deposition

Contact holes are delineated by photolithography (OMR 83 60cp) and the

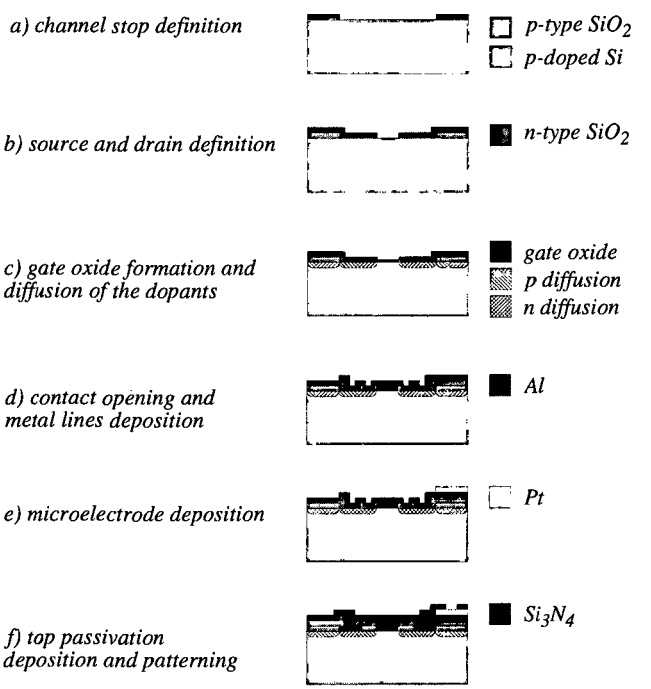

Figure 5.5: Sequence of the technological steps.

exposed SiO_2 is etched down to the surface of the silicon in BHF 1:7. The photoresist is stripped and a 6000 Å thick Al layer is evaporated on the wafer. The metal gates, the address lines and the connections to sources, drains and substrate are defined by photolithography (AZ 1518) so that all the unnecessary metal is subsequently etched in a solution of Alu-etch (fig. 5.5d). Al is annealed at 450°C in N_2 to insure a good ohmic contact.

microelectrode deposition

The microelectrodes are obtained by lift-off (AZ 1518). A Ti adhesion layer of 200 Å thickness is deposited by e-gun evaporation, followed by the deposition of Pt at a thickness of 2000 Å (fig 5.5e).

top passivation layer deposition

A 6000 Å thick PECVD Si3N4 layer is deposited as a top passivation layer. The bonding pads and the active area of the microelectrodes are defined by photolithography (AZ 1518). Exposed Si3N4 is etched in SF_6/O_2 plasma.
Each circuit is saw-diced and encapsulated on a 24 dual in line (DIL) package (fig. 5.6). An O-ring seal is made on top of the circuit with a Corning™ silicone rubber.

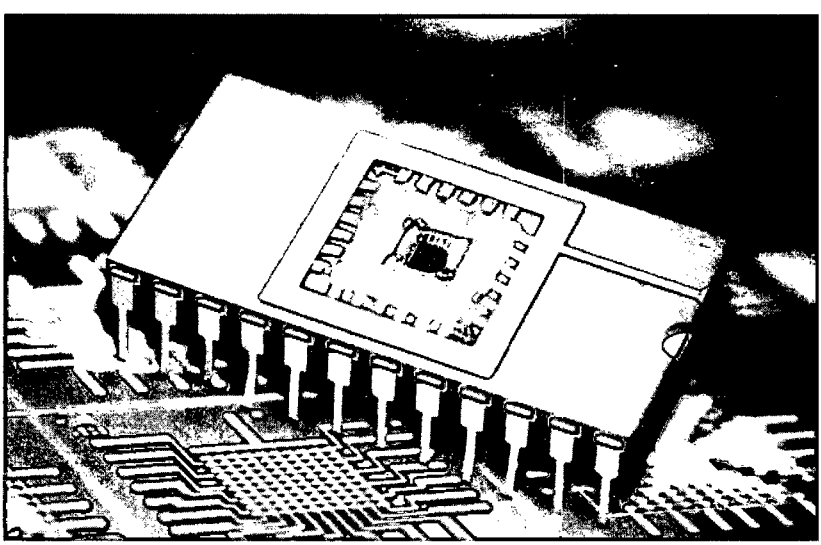

Figure 5.6: Photograph of the DIL mounted device; size of the dye: 4 x 4 mm².

5.4 Characterization of the Device

chemicals, instrumentation and procedure

Electronic tests are performed with a Hewlett Packard 4145B Semiconductor Parameter Analyzer and a Karl Süss prober. Electrochemical measurements are performed with an O-ring cell fixed on top of the circuit, in a Faraday cage. All potentials are quoted with respect to a saturated calomel reference electrode (SCE) and a Pt wire is used as counter electrode. Analytical grade sulfuric acid is diluted to 1 M concentration in deionized water. Ferricyanide ($K_3[Fe(CN)_6]$, Ferri-CN) is purchased from Merck, and solutions of 10 mM are freshly prepared in 1 M KCl. Nafion® 5% wt. in alcohol and pyrrole (PY) are obtained from Aldrich, and ascorbic acid (AA) from Fluka. The potential is controlled by an EC/225 IBM Voltammetric Analyzer. Current response is recorded on XY-t recorder (Kipp & Zonen). The switching signals for the transistors are obtained externally by an in-house built control unit (Appendix B). Different scans (single or continuous) and operation modes (individual electrode, columns or rows of electrodes) are accessible.

5.4.1 nMOS switch characteristics

Prior investigating the electrochemical properties of the array, the output characteristics of the integrated nMOS devices are evaluated for the single and double transistor configuration. Single switches are operated by controlling the gate V_G and the drain voltage V_D. The source and the bulk terminals are shorted to ground. Double switches are characterized by applying simultaneously the same V_G to the gates of both transistors and controlling the drain voltage of the first transistor. The source of the second transistor and the bulk common to both transistors are shorted to ground. The set of equations 5.1 to 5.5bis can be applied to model each transistor in the double switch configuration, provided that the terminal voltages are replaced as indicated in the figure 5.7. Note that, if both switches are operated simultaneously at the same V_G and if V_{DS2} is negligibly small, the double switch behaves as a single switch of gate length corresponding to twice the value of a single gate length.

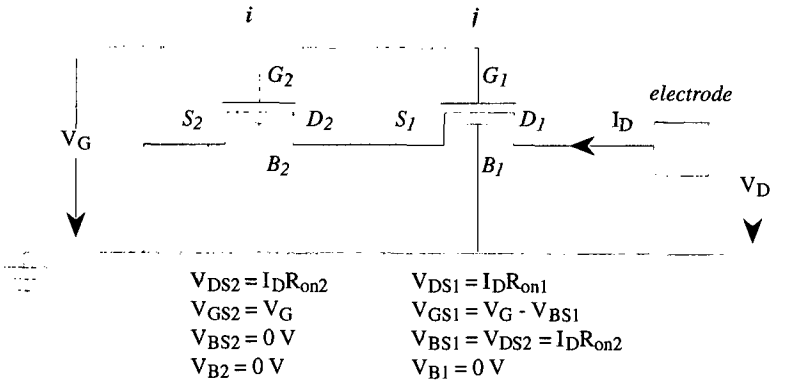

Figure 5.7: Schematic of the double switch configuration and terminal potentials.

general nMOS output characteristics

The output characteristics of single nMOS switch are identical to those of usual n-channel enhancement transistors. For a given V_G the drain current I_D first increases linearly with the drain voltage V_D, then gradually levels off and reaches a saturated value $I_{D,sat}(V_G)$. Owing to the fact that the transistors forming the double switch are placed in series, the device behaves as a large transistor with an equivalent gate length corresponding to twice the value of a single switch gate length, i.e. 20 µm. Output characteristics scaled down by a factor of two are observed (fig 5.8).

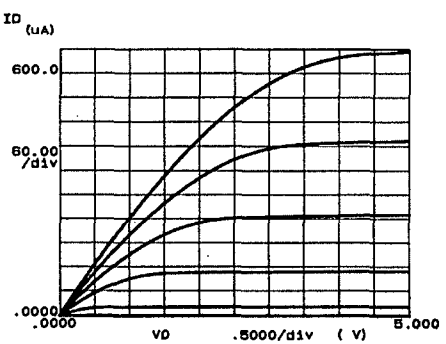

Figure 5.8: Output characteristics of the double nMOS switch; plot of I_D vs. V_D for different V_G; V_D: 0 to 5 V by steps of 0.05 V, V_G; 0 to 5 V by step of 1 V, $V_S = V_B = 0$ V.

subthreshold slope factor and background current

In the subthreshold regime, the semiconductor surface is only weakly inverted and I_D decreases exponentially according to eq. 5.1. By taking the log form of eq 5.1, we obtain a linear relationship of $I_D(V_G)$ of the form $y = mx + b$:

$$log(I_D) = log\left(\frac{W}{L} I'_{Do}\right) + mV_G \quad (5.6)$$

The subthreshold slope factor n can be approximated from the measured slope m , where:

$$m = \frac{q}{nkTln(10)} \quad (5.7)$$

The measured slope m: is respectively 12.4 A/V for the single and double switch configuration, and yields a subthreshold factor n of 1.40 (fig 5.9). This result is in good agreement with typical values usually attributed to MOS devices. The background current of the double switch I_{Do} when the gate voltage is smaller than -350 mV, i.e. in the "off" state, is smaller than 1 pA, and hence should not exceed 100 pA for the whole matrix. Given a signal intensity of several nA, a signal to noise ratio of at least 10 should be achieved.

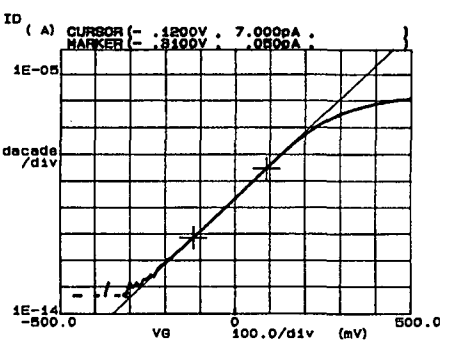

Figure 5.9: Subthreshold characteristic of the double nMOS switch; logarithmic plot of I_D vs. V_G; V_G: -0.5 to 0-5 V by steps of 0.01 V, V_D: 0.05 V, $V_S = V_B = 0$ V.; slope m: 12.4 and $I_{Do} < 0.1$ pA.

threshold voltage

The threshold voltage V_T in the linear operation mode can be determined graphically by plotting I_D/V_D versus V_G for $V_D < V_G - V_T$, so that the channel length modulation term $(1 - \lambda V_{DS}) \approx 1$. The equation of I_D in the linear operation mode can thus be expressed from eq. 5.2 as:

$$\frac{I_D}{V_D} = \frac{\mu_n C_{ox} W}{L}(V_G - V_T) \quad (5.8)$$

which has a linear form of the type $y = mx + b$. The x-intercept corresponds to V_T. Comparable values are obtained for the single and the double switch $V_T \approx 230$ - 270 mV. Consequently any gate voltage higher than these values turns the switches on.

The threshold voltage V_T in the saturated operation mode is determined similarly by plotting $\sqrt{I_D}$ versus V_G. V_D is set at a value comparable to $V_G - V_T$. Neglecting in a first approximation the channel length modulation term, eq. 5.4 can be rewritten as:

$$\sqrt{I_{Dsat}} = \sqrt{\frac{\mu_n C_{ox} W}{2L}}(V_G - V_T) \quad (5.9)$$

from which V_T can be extracted. Comparable values of threshold voltage are obtained for the single and double switch configuration $V_T \approx 210$ - 230 mV (fig 5.10).

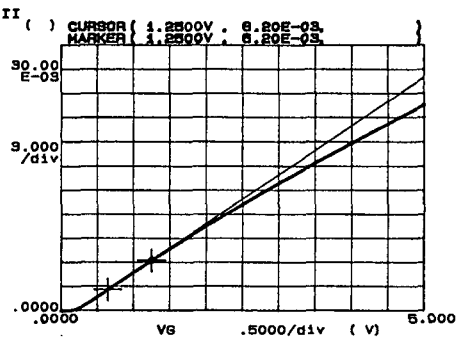

Figure 5.10: Threshold voltage evaluation for the double nMOS switch in a saturated regime; plot of $\sqrt{I_D}$ vs. V_G; V_G: 0 to 5 V by steps of 0.05 V, V_D: 5 V, $V_S = V_B = 0$ V.

channel modulation factor and $R_{on,sat}$

The channel modulation factor λ is determined from the slope in the saturated region of the output characteristic $I_D(V_D)$. The eq. 5.3 can be rewritten in a linear form as:

$$I_{D,sat} = I_D' \lambda V_D + I_D' \quad (5.10)$$

which has the form of $y = mx + b$. λ is found by dividing the measured slope m by the y-intercept b. The values of λ are in the order of 0.008 V^{-1} for the single switch and 0.005 V^{-1} for the double switch (fig. 5.11). These values are in good agreement with those generally obtained for nMOS transistors.

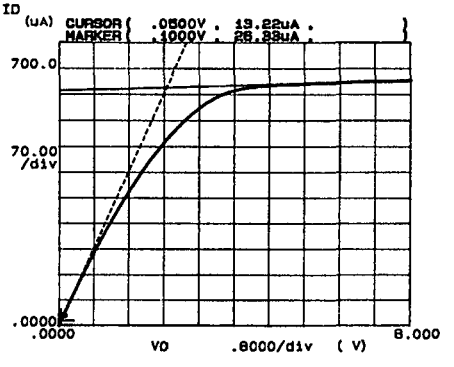

Figure 5.11: Evaluation of the channel modulation factor of the double nMOS switch; plot of I_D vs. V_D; V_D: 0 to 8 V by steps of 0.05 V, V_G: 5 V; $V_S = V_B = 0$ V; tangent in the saturated regime (solid line): slope m: 3.43 μA/V and y-intercept: 640 μA; tangent in the linear regime (dotted line): slope m: 275 μA/V.

switch resistance R_{on} *and* R_{off}

The channel resistance $R_{on,sat}$ in the saturated operation mode can be directly estimated from the reciprocal of the slope measured in figure 5.11 (solid line). $R_{on,sat}$ takes the values of 92 KΩ for the single switch and 291 KΩ for the double switch. Note that $R_{on,sat}$ for the double switch is more than twice the value of that of the single switch because of the differences in the modulation factor.

Similarly, the double switch resistance $R_{on,lin}$ in the linear operating mode ($V_D < V_G - V_T$) can be estimated from the slope of the tangent in the linear

regime (dotted line). The reciprocal of the measured slope yields a value of $R_{on,lin}$ about 3.6 KΩ. A close-up view of the current range of interest (± 100 nA), shows that $I_D(V_D)$ is ideally linear, and that the current offset at V_D: 0V is negligibly small (< pA). Moreover, as long as the signal intensity remains smaller than 0.2 µA, the ohmic drop V_D stays below the mV (fig. 5.12). These results indicate that the switch does not introduces ohmic distortion or significant potential drop, and, owing to a low offset current that the signal intensity can span from several pA to 100 nA. This lower limit however increases to about 100 pA if the entire addressing matrix is considered.
In the "off" state, R_{off} is in the order of 10^{12} Ω with a leakage current of less than 1 pA. These values are in good agreement with those generally obtained for nMOS switches [15].

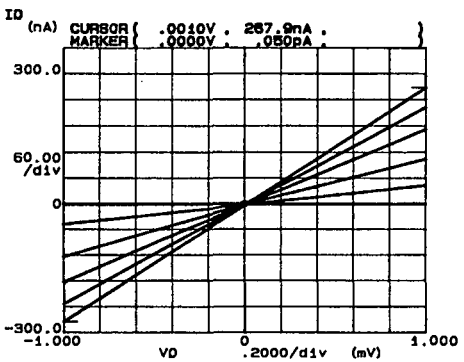

Figure 5.12: "on-off" current-voltage characteristics of the double nMOS switch; plot of I_D vs. V_D; V_D: -1 to 1 mV by steps of 1 mV, V_G; 0 to 5 by steps of 1 V; $V_S = V_B = 0$ V; $R_{on,lin}$: 3.7 KΩ, R_{off}: 3.5 10^{-12} Ω

Note that to be able to drive large negative currents through the switch without forward biasing the drain/bulk pn junction, a negative bias must be applied to the bulk. However, due to the currents magnitude involved, i.e. small V_D, no reverse biasing of drain/bulk junction is necessary and V_B can be shorted to ground.

5.4.2 Microelectrode array characteristics

Prior investigating the mapping ability of the array, the electrochemical behavior of the Pt microelectrodes is tested by cyclic voltammetry in a solution of 1 M H_2SO_4. The entire matrix is scanned and the response of each microelectrode is successively recorded. The features of the background voltammograms are comparable to those obtained for bulk Pt.
Note that due to the poor passivation properties of the PECVD top passivation layer, the stability of the device is reduced. The presence of Al hillocks and pinholes in the passivation layer leads to the corrosion of the Al metal lines within several hours depending on the solution composition. This problem can be circumvented by changing the design of the device and placing the electronics aside from the microelectrodes, e.g. on one side of the chip. The multiplex unit can in this case be encapsulated by an epoxy resin offering better resistance in liquids.

mapping properties

Reduction of 10 mM Fe^{3+} in 1 M KCl is successively performed on all

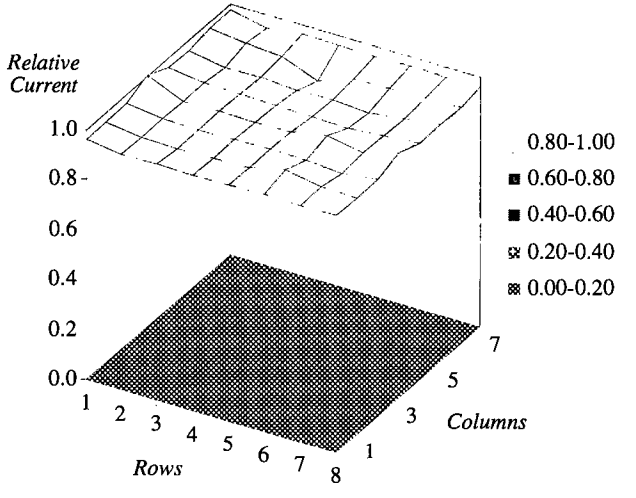

Figure 5.13: Electrochemical mapping achieved by addressing 64 microelectrodes of the array; reduction of 10 mM Fe^{3+} in a solution of 1 M KCl/N_2 at 0 V.

microelectrodes to assess the good functioning of each element. Figure 5.13 shows that the collected response is similar at each measuring site. The responses are normalized and expressed in percentage of the magnitude of the highest response.

To illustrate the mapping properties of the array, the device is then partially covered by a drop of Nafion® deposited on top of the surface with a micropipette. The current response at these modified microelectrodes is clearly affected by the charge exclusion properties of the polymer, as no reduction current of the negatively charged ferri-CN ions is recorded (fig. 5.14).

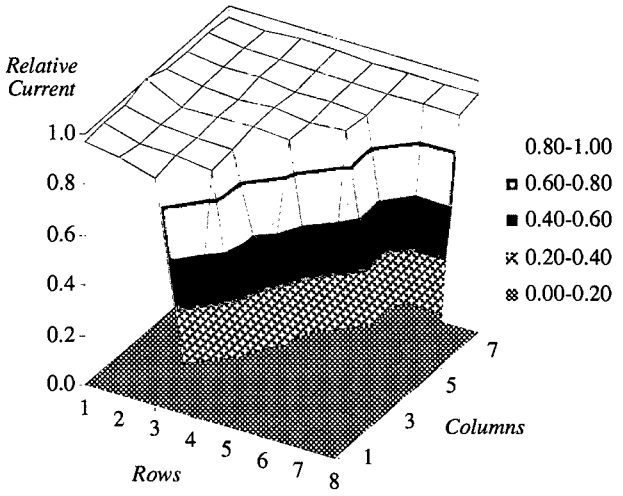

Figure 5.14: Reduction of 10 mM Fe^{3+} in a solution of 1 M KCl/N_2 at 0 V, with a Nafion® partially covered array.

A significant response is however recorded in the case of oxygen reduction (fig. 5.15) as gas molecules can diffuse across the polymer. The reduction current collected at the modified microelectrodes is about 40% of the current magnitude at bare Pt microelectrodes suggesting that the diffusion and the solubility oxygen in the polymer are lower than in aqueous electrolyte.

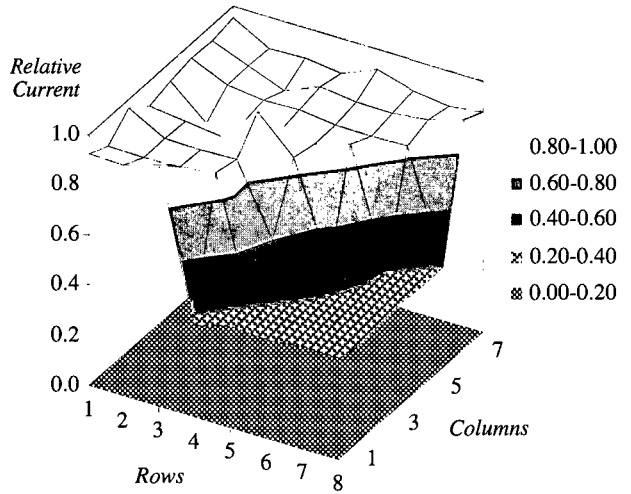

Figure 5.15: Oxygen reduction in PBS at 0 V with a Nafion® partially covered array.

electrochemical modification

Pyrrole is used as model system to illustrate the ability to selectively modify the array by electrodepositing a polymeric membrane onto the selected microelectrode surfaces. The deposition of the polymer is carried out by cyclic voltammetry as described in [19], from a solution of 0.1 M KCl containing 0.1 M PY. The potential is swept from 0.1 V to 0.825 V, at 25 mV/s. The columns of the array, formed by 10 vertically addressed microelectrodes, are distinctly modified by different membrane thicknesses. The first two columns are kept without deposition as a reference. The electrodeposition is performed onto the 8 remaining columns, by cycling the potential 4 times over the sweep range and disconnecting one column after each half cycle to achieve different thicknesses (fig. 5.16). The thickness of the membrane is estimated from the charge, assuming that 45 mC/cm^2 corresponds to a thickness of 0.1 μm [19]. It can be seen that, after the second sweep, i.e. column number 6, the thickness of the membrane varies linearly with the number of sweeps (r: 0.998).

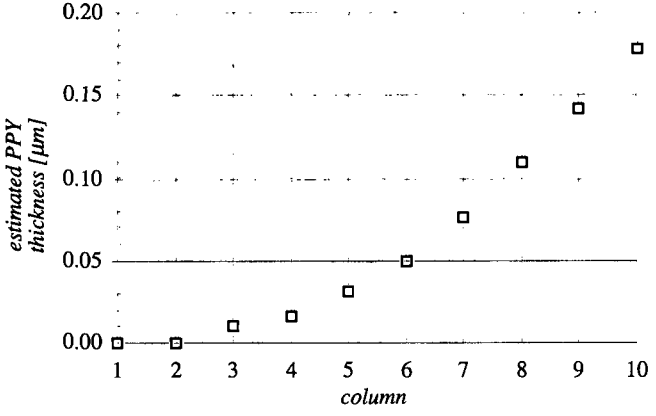

Figure 5.16: PPY thickness estimated from the charge transferred at each column during electrodeposition.

The background current of each column is successively observed by cyclic voltammetry in 1 M KCl at 25 mV/s, within the potential range of 0.1 to 0.4 V (fig. 5.17). The charging current is measured at 0.1 V and shows a linear dependence with the membrane thickness (r: 0.994).

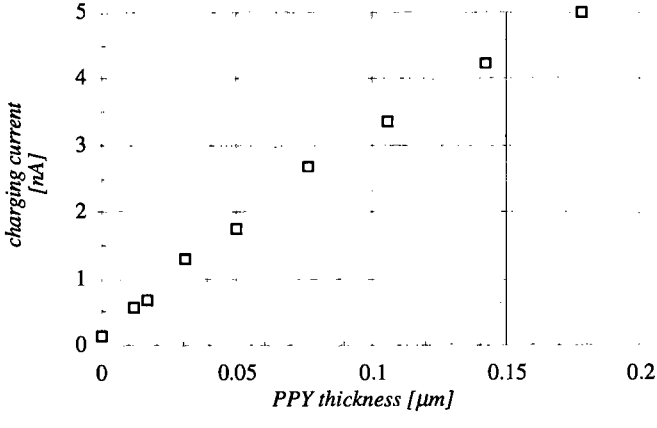

Figure 5.17: Dependence of the charging current with the PPY thickness; data obtained by cyclic voltammetry in 1 M KCl at 25 mV/s, with a potential range of 0.1 to 0.4 V; charging current measured at 0.1 V for each column of the array.

Polypyrrole is known to display anti-interference properties resulting from a size or charge exclusion effect [20]. In its "as electrodeposited" state, i.e. conductive state, the charge transfer occurs at the polymer surface. When 0.1 mM AA is added to the 1 M KCl solution, the oxidation current of AA recorded at 0.4 V for each column shows, as expected, a response independent of the membrane thickness (fig. 5.15). The anti-interference properties of the membrane are obtained when the polymer is in its over oxidized state, i.e. non conductive state. This over oxidation is achieved by sweeping the modified electrodes in 0.1 M KCl, from 0 to 1V. All columns are "switched-on" and swept simultaneously within the potential range until the voltammogram becomes stationary. In this case, when AA is added to the solution, the oxidation response is clearly affected by the thickness of the polymeric membrane. The current response decreases with the polymer thickness due to an increase of the diffusion barrier. The signal for AA is reduced to less than 30% of the initial value at bare Pt microelectrodes, i.e. unmodified columns, for membrane thicknesses > 0.18 μm.

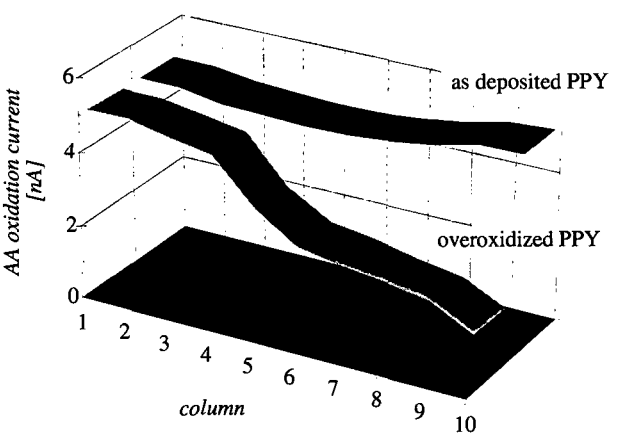

Figure 5.18: Change in permeability of PPY in its "as deposited" and over oxidized state, effect of the PPY thickness on the oxidation response of AA; background corrected currents; data obtained by cyclic voltammetry in 1 M KCl and 0.1 mM AA at 25 mV/s; with a potential range of 0.1 to 0.4 V; oxidation current measured at 0.4 V for each column of the array.

5.5 Conclusion

The concept of electrodes switching and multiplexing using nMOS switches integrated "on chip" has been proposed. The feasibility of the study has been demonstrated by the fabrication of an array of 100 individually addressable microelectrodes.

The electronic properties nMOS switches have been thoroughly investigated. The operation state of the switch can be controlled by classical 0-5 V logic levels. The background current per the switch is less than a picoamp and does not exceed 100 pA for the entire device. For a current range of 1 to 100 nA, a signal to noise ratio of at least 10 is achieved. The channel resistance of the switch in the "on" operation state is of about 3.7 KΩ. This value is in excellent agreement with those typically reported for nMOS switch of comparable geometric parameters. The ohmic drop generated by the switch resistance is therefore below 1 mV for the current range of interest. In the "off" operation state, a very high switch resistance in the scale of 10^{12} Ω is observed. "Unswitched" microelectrodes are thus virtually disconnected and left at "open circuit".

Two set of experiments qualitatively illustrate the mapping properties of the device, and the ability of collecting distinct information on selectively modified electrode surfaces. The actual design can be tailored to meet specific application requirements, such as linear positioning of the sensing elements in the vertical direction to monitor the concentration gradient of trace metals at air/water and water/sediments interfaces.

References

[1] Fiaccabrino G.C., Koudelka-Hep M., Jeanneret S., van den Berg A., de Rooij N.F., Sensors and Actuators B, 18-19 (1994) 675-67

[2] Fiaccabrino G.C., Strike D.J., Jeanneret S., de Rooij N., Koudelka-Hep M., 5th Intern. Meeting on Chem. Sensors, Rome, 1994, Technical Digest, vol 2, 1058-1061

[3] Tercier M.L., Buffle J., Electroanalysis, 5 (1993) 187-200

[4] Dees D.W., Tobias C.W., J. Electrochem. Soc.: Electrochem. Sci. and Tech., 134 (1987) 369-377

[5] Gross G.W., IEEE Trans. on Biomed. Engin., BME 26 (1979) 273-279

[6] Novack J.L., Wheeler B.C., IEEE Trans. on Biomed. Engin., BME 33 (1986) 196-202

[7] Carter S.J., Linker C.J., Turkle-Huslig T., Howard L.L., IEEE Trans. on Biomed. Engin., BME 39 (1992) 1123-1129

[8] Gisiger A., Clerc P.A., Jeanneret S., de Rooij N., Koudelka-Hep M., Muller D., Stoppini L., 5th Intern. Meeting on Chem. Sensors, Rome, 1994, Technical Digest, vol 1, 205-208

[9] Bard A.J., Denuault G., Lee C., Mandler D., Wipf D.O., Acc. Chem., Res., 23 (1990) 257

[10] Kakerow R, Manoli Y., Mokwa W., Rospert M., Cammann K., Krause J., Meyer H., Tech. Digest, Transducers '93, Yokohama, Japan, June 7-10, 1993, pp 1074-1077

[11] Kakerow R., Manoli Y., Mokwa W., Rospert M., Meyer H, Drewer H., Krause J., Camman K., Sens. Actuators A43 (1994) 296-301

[12] Meyer H, Drewer H., Krause J., Camman K., Kakerow R., Manoli Y., Mokwa W., Rospert M., Sens. Actuators B, 18 (1994) 229-234

[13] Meyer H, Drewer H., Gründig B., Camman K., Kakerow R., Manoli Y., Mokwa W., Rospert M., Anal. Chem., 67 (1995) 1164-1170

[14] Meyer H., "Entiwcklung und Characterisierung von bildgebenden Chemo- un d Biosensorarray, PhD dissertation, Westfälishen Wilhelms-Universität Münster, 1995

[15] Allen P.E,Holberg D.R., "CMOS Analog Circuit Design", Holt, Rinehart and Winston, New York, 1987

[16] Geiger R.L., Allen P.E., Strader N.R., "VLSI Design Techniques for Analog and Digital Circuits", McGraw-Hill, New York, 1990

[17] Sze S.M., "Semiconductor Devices: physics and technology", Wiley and Sons, New York, 1985

[18] Massobrio G., Antognetti P., "Semiconductor Device Modeling with SPICE", 2nd Ed., McGraw-Hill, New York, 1993

[19] Strike D.J., de Rooij N., Koudelka-Hep M., Sensors and Actuators B, 13-14 (1993) 61-64

[20] Hämmerle M., Schuhmann W., Schmidt H.L., Sensors and Actuators B, 6 (1992) 106-112

Conclusion

The major achievements of this work are to be exploited in two projects on **Electrochem**ical microsensors (ELCHEM), under the auspices of the Swiss Priority Program in **Mi**cro and **Na**no **S**ystem **T**echnology (MINAST). The first subject concerns the development of a gas analysis system (artificial olfactory systems, or "electronic nose") based on the combination of an array of chemoresistors made of distinct conducting polymers coupled with an artificial neural network. To this end, interdigitated microelectrode arrays can be utilized as transducers for the different chemoresistors. This system is aimed at specific applications in the consumer goods industry and should allow the finger-printing of various odors in order to assess the process quality. The various polymeric layers and the deposition techniques can eventually be optimized to achieve a high discrimination power with a limited number of sensors. This work is carried out in conjunction with the Fabriques de Tabac Réunies S.A. (CH) and Kraft Jacobs Suchard Management & Consulting (CH).

Interdigitated microelectrode arrays have also been used as transducer to monitor the variation of the membrane conductance of a new type of ion sensors. The operation of these **I**on **S**elective **C**onductimetric **M**icrosensors (ISCOMs) is based on the specific and reversible ion co-extraction from the aqueous solution into a sensitive membrane containing an ionophore. The detection of the primary ion is accomplished by measuring the bulk conductance of a thin plasticized polymeric membrane, cast on top of the interdigitated array. This project is part of the E.C. program ESPRIT IV and is entitled "Totally **in**tegrated microengineered **ion** sensors for large-scale applications (INION)". This project involves the collaboration of Institut für Chemo- und Biosensorik (ICB) of the University of Münster (D), Company Research Laboratory at the British Nuclear Fuels (UK), the National Institute for Coastal and Marine Management (RIKZ) (NL), Fluka Chemie AG (CH) and Ifremer (F).

The second aspect of the MINAST project concerns the development of voltammetric microsensors for routine *in situ* and *ex situ* analysis of trace elements in the environment. This research will partly be conducted on the basis of the results obtained with the Hg-plated iridium microdisk arrays and the sputtered carbon thin-films, in the collaboration with the CABE institute of the University of Geneva (CH), Metrohm AG (CH) and the CSEM (CH).

Similarly, in a joint research effort with Hydronaut Srl (I), CABE (CH) the AMK institute of the University of Gøteborg (S), voltammetric probes based on Hg-plated iridium microdisk arrays for trace metal detection are currently under development. This project is part of the E.C. Marine science and technology program (MAST III), and is entitled "voltammetric autonomous measuring probes for trace metals in the water column (500 m) and at water-sediment interfaces (6000 m) (VAMP)".

Appendix

Working Principle of the Bipotentiostat

In contrast to the classical bipotentiostat layout that is usually proposed (see ref. [59], chapter 4), the approach depicted in figure A.1 and A.2 has been followed. It can be seen that in our case, the bipotentiostat is composed of two identical channels (1 and 2), in which the working electrode potentials E_1 and E_2 are set independently one from another. Since the reference electrode (*RE*) is set to analog ground, the working electrodes are individually biased by shifting the potential of positive input of their respective operational amplifier by the amount of E_1 and E_2. Each channel has a current to voltage converter with 5 discrete gain factors from 10nA/V - 100 μA/V, and a low pass filter with 5 time constants from 1 ms to 10 s. The output stage consists of a differential amplifier with a fixed gain of 10 restoring to analog ground the potential level of the converted current.

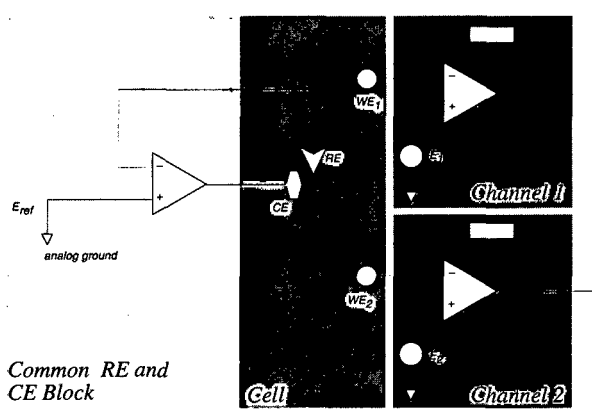

Figure A.1: Working principle of the bipotentiostat. The reference electrode RE is set to analog ground; the working electrode (WE_i) potential is shifted from ground by E_i

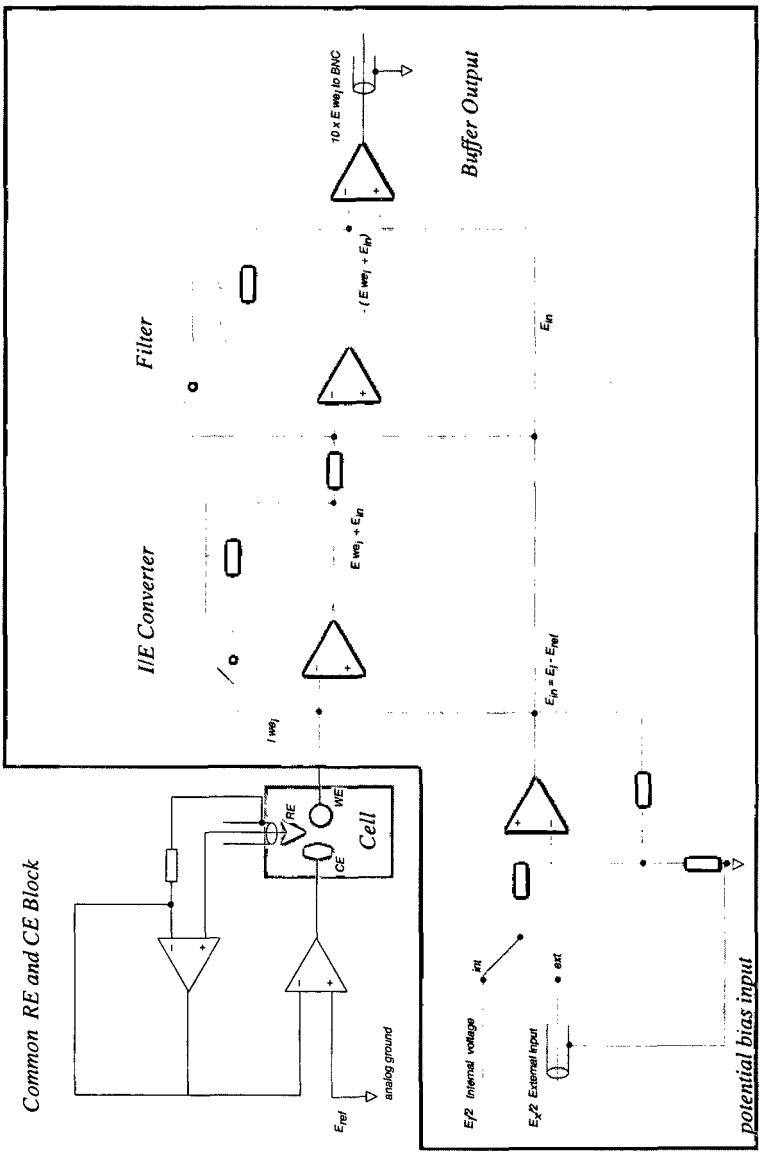

Figure A.2: Schematic of the bipotentiostat layout.

Appendix B

Working Principle of the Control Unit

The generation of the different clock waves driving the 20 addresses lines of the nMOS switches is obtained by cascading two decade counters with 10 decoded outputs (fig. B.1). A reference clock signal with 20 times the frequency of the "on state" of the switch is fed into clock input of the first decade counter. The decoded outputs of the first counter are interfaced to the row address lines of the matrix, whereas those of the second counter are connected to the column address lines. At each rising edge of the reference clock signal, the decoded outputs will successively turn one row address at a time to a high logic state. As the carry out of the first decade counter feeds the clock input of the second decade counter, the column address will be

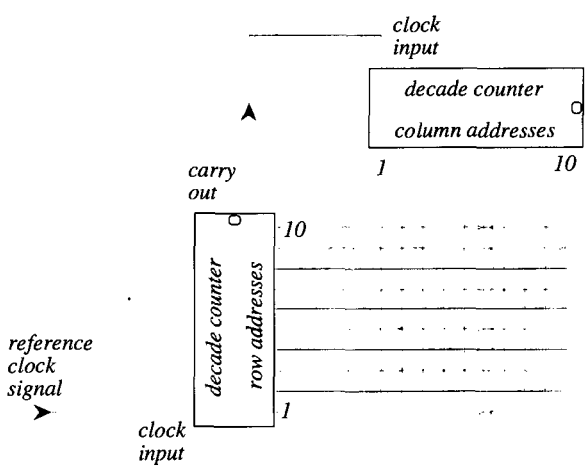

B.1: Schematic of the interfacing principle. Depending on its location in the matrix, each gate terminal of the nMOS switch is connected to the pertinent column or row address.

incremented after the first counter has completed its counting cycle. The corresponding generated signals are depicted in the following figure.

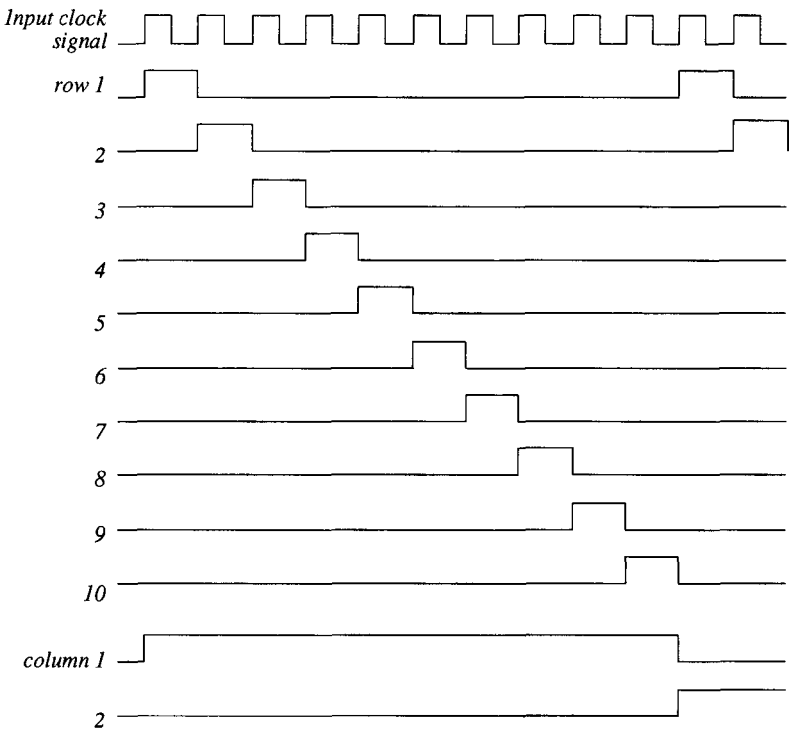

Figure B.2: Schematic of the generated clock waves.

Acknowledgments

I would like to thank Prof. Nico de Rooij for offering me the opportunity to work in such a motivating and enthusiastic team, for his guidance and support throughout this project. Thank you Nico, for the faith and the freedom of action you have granted me during this work.

I wish to give a special expression of my gratitude to Prof. Milena Koudelka-Hep. By her perceptive comments, helpful suggestions, sharp common sense and keen sense of humor, made her a remarkable help and an enjoyable person to work with. Incommensurable is the effort and care she has employed to shed some light on the multiple facets of electrochemistry, especially on Monday mornings before the coffee break. Thank you Milena, for looking puzzled whenever I was asking you foolish questions. Specials thanks to Dr. David J. Strike for his non negligible contribution in teaching me the fundaments of charge transfer and mass transport processes, and the refinement of the Shakespeare's mother tongue. Thank you David, for your knowledgeable discussions and your cheerful spirit during my ups and downs.

It was a great honor that PD Dr. Werner Morf, Prof. Scott Collins and Prof. Rosemary Smith generously accepted to give some of their time to the careful reading and correction of parts of this manuscript. I remain truly grateful to them. I gratefully acknowledge Prof. Hubert H. Girault from the Chemical Department of the Polytechnical School of Lausanne and Dr. Helwig Schäfer from Metrohm A.G. in Herisau, for kindly agreeing to be the co-examiners of my work.

I am indebted to the highly skilled technicians, Sylviane Pochon, Sabina Jenny, Pierre-André Clerc and Sylvain Jeanneret, for running the microfabrication lab against all the odds. The completion of this work would not been possible without their competence. Specials thanks to

Dr. Xiao-Ming Tang from the CSEM, for his outstanding contribution to the successful completion of the carbon project.

I wish to express my gratitude to Marie-Louise Tercier, Dr. Cecile Belmont and Prof. Jacques Buffle from CABE, University of Geneva, for sharing with me their expertise on trace metal analysis and for their significant contribution to this present work.

I also owe thanks to Arnaud Gisiger for his sound suggestions on the manuscript, to Dr. Sacha Choulga and Dr. Benedickt Ahlers for helpful discussions on interdigitated microelectrode arrays, to Dr. Philippe Arquint for his wise technical inputs and for not loosing his temper with the tedious book-keeping of the ethics orders, to Marc Boillat with my apologies for proof reading the only chapter of this work which will never be published and kindly letting me monopolize the computer for ages, to Marc-Alexis Gretillat for his excellent introduction on the cleanroom work, good tips and helpful discussions on MOS transistors, to Dr. Bart Van der Schoot for his hints in electronics and emulating discussions on potentiostats, to Pierre-François Indermühle for his meticulous and wonderful work on the AFM pictures, to Dr. Peter van der Wal, Marco Meijerink, Dr. Volker Gass, Pierre Thiébaud, Cynthia Beuret, Dr. Jürgen Brugger, Dr. Nicolas Blanc, Philippe Luginbuhl, Dr. Georges-André Racine, Florence Paoletti, Lionel Paratte, Cornel Marxer and many others without whom the group of Nico de Rooij would not be such a stimulating and friendly team to work with.

Finally I would like to gratefully acknowledge my relatives and friends for their support in this endeavor, and la Fondation Suisse pour la Recherche en Microtechnique FSRM for the financial support of the carbon project.

And last but not least, to my beloved wife,

Pour ton inépuisable soutient et ta compréhension, Delphine, reçoit le témoignage de ma profonde reconnaissance et de mon amour.